Momentum Transfer due to Hypervelocity Impacts into Spacecraft Solar Arrays

MSc Thesis

Conor Ryan

Delft University of Technology

TU Delft

Momentum Transfer due to Hypervelocity Impacts into Spacecraft Solar Arrays

by

Conor Ryan

Student number:	5126541	
Project duration:	March, 2021 - November, 2021	
Thesis supervisors:	Dr. Jian Guo	TU Delft (supervisor)
	Dr. Hanspeter Schaub	University of Colorado Boulder (co-supervisor)
Thesis committee:	Dr. Jian Guo	TU Delft
	Dr. Hanspeter Schaub	University of Colorado Boulder
	Dr. Angelo Cervone	TU Delft (Chair)
	Dr. Otto Bergsma	TU Delft (External examiner)
Institution:	Delft University of Technology	
Place:	Faculty of Aerospace Engineering, Delft	

Cover Image: A debris object colliding with a satellite. Credit: The Aerospace Corporation.

TU Delft

University of Colorado Boulder

Acknowledgements

Conor Ryan
Ballina County Tipperary, March 2022

I would like to start off by thanking my supervisors, Dr. Jian Guo and Dr. Hasnpeter Schaub, for their continued support and feedback throughout this project. Although this area of research was new to all of us, you showed great patience and flexibility in allowing me the freedom to explore this field.

I also had the great pleasure of working with Ms. Anne Aradyne Bennett, a graduate researcher at the Colorado Center for Astrodynamics Research. Anne's passion for what she does inspired me and without her, this project would have never gotten off the ground. I certainly could not have done it without you Anne.

I would also like to thank the Europe-Colorado mobility programme who granted me the opportunity of a lifetime in allowing me to work on my research at the University of Colorado Boulder. Special thanks to everyone at the AVS Lab and on the programme who I had the pleasure to get to know. Friday happy hours, weekend camping trips and the countless adventures made for an unforgettable experience. My time in Boulder made 6 months feel like a week, and for that, I am truly grateful.

I could not forget the life-long friends that I made during my Bachelors degree at the University College Dublin. Getting to experience college life with all of you has been a pleasure and I look forward to spending many more years together in the future.

Finally, I would like to thank my parents and my two brothers. Their unconditional love and support throughout this Masters thesis and indeed throughout my life has been incredible. I would not be accomplishing this goal without all of them.

Mar a deir an seanfhocal -

Giorraíonn beirt bóthar

.

Summary

During a hypervelocity impact, momentum enhancement can take place whereby the momentum imparted to a target can actually be greater than the initial projectile momentum. This is due to large amounts of target material or ejecta being expelled from the impact crater. The increase in momentum is quantified using a Momentum Enhancement Factor (MEF) which is a measure of how efficiently a projectile transfers its momentum to a target. Understanding how the MEF changes for a variety of hypervelocity impact conditions is vital when analysing the momentum transfer that occurs when two objects collide.

The majority of hypervelocity impacts that occur in Low Earth Orbit (LEO) are a result of untrackable space debris colliding with satellites. The 1-3 mm debris size range is of particular interest as it remains untrackable and can have devastating consequences if it collides with a target at orbital velocities of up to 15,000 m/s. These untrackable debris objects pose a significant threat to operational satellites and need to be explored to mitigate their damaging effects. Although the phenomenon of momentum transfer due to hypervelocity impacts has been understudied throughout literature thus far, broadening our knowledge of the momentum enhancement factor can help us use in situ data to tune models to better assess and address impact risks. With the rapid increase in small satellite launches, coupled with the planned expansion of mega-constellations in the near future, understanding the response of satellite structures to impact is critical.

After a thorough literature review, it was recognised that there was a significant absence of published information regarding the transfer of momentum from space debris to a satellite. Furthermore, very little information exists on hypervelocity impacts into typical spacecraft solar arrays. Due to the high costs and massive space required to house hypervelocity impact test equipment, experimental results are rare. However, a number of numerical tools have been developed to accurately model impacts at very high velocities. These tools implement a mesh-free method of discretisation known as Smoothed Particle Hydrodynamics (SPH), and have enabled the present study to explore the behaviour of simplified models of typical spacecraft solar panels under hypervelocity impact. ANSYS Autodyn was selected as the software of choice as it is one of the most widely used numerical tools to model hypervelocity impacts on the market. Validation was carried out by comparing results to previous hypervelocity impact experiments.

Two solar panel configurations were initially considered for this study. The first being the European Retrievable Carrier (EURECA) solar panels and the second being the Hubble Space

Telescope (HST) solar panels. Due to its less complex layup, the HST solar panel computational models ran a lot faster which allowed for more runs and better data and so was the solar panel chosen for this research

A range of simulations were performed in order to determine the MEF values resulting from various projectile and target conditions. Impact velocities from 2,000-14, 000 m/s were simulated for spherical aluminium, copper and glass projectiles of 1.0, 1.5, 2.0 & 3.0 mm diameter. In addition to the sphere, three other projectile shapes were analysed, namely a cone, cylinder & punch. A silicon layer was also implemented in the target, although no validation data was available and so, this remains to be a proposed model.

This thesis concludes by implementing the MEF values obtained into a model, which together with the change in semi-major axis of a satellite due to impact, can be correlated to debris sizes. These results have the potential to be applied to space debris environment validation and help fill the gap in data for 1-3 mm size projectiles.

Contents

Nomenclature

Abbreviations

Abbreviation	Definition
ADR	Active Debris Removal
Al	Aluminium
CCD	Charge-Coupled Device
CFD	Computational Fluid Dynamics
CFRP	Carbon Fiber-Reinforced Polymers
CSM	Computational Solid Mechanic
COTS	Commercial Off-The-Shelf
dSMA	Difference in Semi-Major Axis
EMR	Energy-To-Mass Ratio
EOS	Equation of State
ESA	European Space Agency
EURECA	European Retrievable Carrier
FDM	Finite Differences Method
FEM	Finite Elements Method
FE	Finite Element
FOS	Factor Of Safety
GEO	Geostationary Orbit
HAX	Haystack Auxiliary Radar
HC	Honeycomb
HST	Hubble Space Telescope
HVI	Hypervelocity Impact
ISS	International Space Station
LEO	Low Earth Orbit
MASTER	Meteoroid and Space Debris Terrestrial Environment Reference Model
MEF	Momentum Enhancement Factor
MPM	Material Point Method
NASA	National Aeronautics and Space Administration
ORDEM	Orbital Debris Engineering Model
RTV	Room Temperature Vulcanizing

Abbreviation	Definition
SPH	Smoothed Particle Hydrodynamics
SSBM	Standard Satellite Breakup Model
SSN	Space Surveillance Network
STS	Space Transportation System (the Space Shuttle)
UHMW-PE	Ultra-High Molecular Weight Polyethylene

List of Figures

List of Tables

1

Introduction

Space debris is increasingly acting as a major contributor to pollution levels in the space environment. This has major implications for spacecraft and drastically jeopardises the future of space operations. In January 2021, the statistical models used by The European Space Agency estimated that there are approximately 34,000 debris objects greater than 10 cm in orbit, 900,000 objects between 1 cm and 10 cm and 128 million objects from greater than 1 mm to 1 cm [1]. Fast forward 8 months to September 2021 and these numbers have gone up to 36,500 objects greater than 10 cm, 1,000,000 objects from greater than 1 cm to 10 cm and 330 million objects from greater than 1 mm to 1 cm. With the increasing number of small satellites being launched and the planned expansion for mega-constellations, the drastically rising levels of space debris is only going to get worse and pose major risks to operational satellites [2].

Depending on its size, space debris and meteoroids are catalogued using a variety of techniques. Trackable debris is measured using ground-based methods such as radar and optical assets, while untrackable debris is modelled statistically. These models are developed from retrieved surfaces and in situ impact detectors which are analysed to measure impact fluxes and debris populations. Currently, the models employed by NASA to track debris under 1 mm rely on data interpolation between impact counts from the Space Shuttle missions. Everything over 3 mm is tracked using radar data [3]. This leaves a small but significant gap in the 1-3 mm size debris range, which may appear insignificant, but when travelling at orbital velocities of anywhere up to 15,000 m/s in LEO can have devastating consequences.

When a hypervelocity impact like this occurs, a phenomenon called momentum enhancement can take place. This refers to when the momentum imparted to the target can be larger than the original momentum of the impactor due to ejecta being expelled backwards from the impact crater. Little research has been conducted to fully understand the effects that an undetectable small strike has on a spacecraft in terms of momentum transfer. Furthermore, there have not been any published studies attempting to understand the momentum transfer that occurs

between debris and spacecraft solar arrays. Solar arrays are one of the most critical parts of a spacecraft and their massive surface area exposure makes them extremely susceptible to debris strikes.

Due to the fact that small debris in the range of 1-3 mm is untrackable, spacecraft cannot carry out collision avoidance manoeuvres and have to rely on using models to assess the average risk of being struck by this debris. A collision between a non-catastrophic object and an operational spacecraft may happen unexpectedly and spacecraft operators need to be able to predict the motion of the spacecraft which ensues a strike [4]. The ability to identify and understand non-catastrophic small debris strikes allows space users to effectively make allowances for the ensuing dynamical effects on the spacecraft as well as helping to attribute potential future anomalies [5].

1.1. Space Debris

The space debris environment encompasses naturally occurring meteoroids and also man-made objects that have been placed into Earth's orbit. This littering of space is a consequence of human negligence and it is undeniable that the continuous pollution of the space environment will have some major implications for the future of space use. While the number of meteoroids remains close to constant, the number of space debris particles generated by human activity continues to increase with ongoing space mission activities. Due to the lack of active debris removal missions and global norms regarding end-of-life disposal, the majority of these objects remain in space and thus their numbers continue to increase. The list of items that pertains to space debris is numerous. This includes objects like payloads, upper stages, intact but non-operational satellites, as well as parts ejected during the missions like bolts, foil scraps, springs and protective covers of optical instruments. Explosions or collisions resulting from fragmentation can cause an increase in the amount of particles present. Additionally, both atomic oxygen corrosion and thermal cycling can result in the release of paint flakes from painted surfaces and thermal protective foils. Impacts from these microparticles can create even more ejection material [6]. These objects are spread across a vast spatial range, extending from Low Earth Orbit (200 - 2,000 km) to Geostationary Orbit (GEO) (33,000 - 39,000 km) and beyond. GEO is generally the limit of human interest around space debris due to the fact that most space activity occurs below this altitude. Figure 1.1 shows the trackable debris objects in LEO (not to scale) highlighted by a yellow ring. Relative impact velocities in this region tend to be between 10,000 and 11,000 m/s.

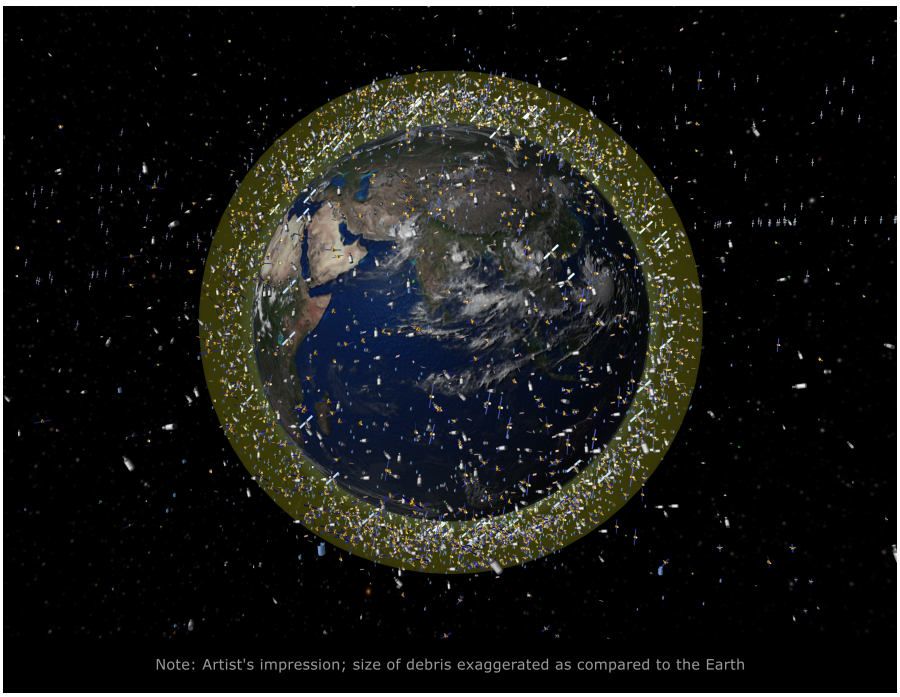

Figure 1.1: Debris objects in Low Earth Orbit [7].

1.1.1. Classification of Debris Sizes

As previously stated, there are an estimated 330 million particles between 1 *mm* and 1 *cm*, 900,000 objects between 1 *cm*, and 10 *cm*, and 36,500 trackable objects larger than 10 *cm* in Earth's orbit [1]. These can be classified as small, medium and large debris respectively:

- Small debris falls into the category of either mission-related objects such as aluminium oxide particles expelled from solid rocket motors, or fragmentation debris which is the product of either breakups or surface deterioration [8]. Other sources include paint flakes and meteoroids. These objects are generally in the range of 1 *mm* - 1 *cm* in size and cannot be directly monitored or their orbits predicted.
- The medium sized debris population is not as well-known as that of larger debris. This category of debris is between 1 *cm* - 10 *cm* in size and is not currently tracked. It is mainly composed of fragmentation debris and mission-related objects such as sodium potassium coolant droplets, solid rocket motor char, slag and dust [9]. The only real measurements of the medium-sized debris population come from sampling of lower-altitude, higher-inclination LEO orbital regions with ground-based sensors. Apart from this, there exists only estimations of the size and characteristics of the medium-sized debris population which are based on extrapolations [8].
- Larger debris of sizes >10 *cm* are far easier to track using ground-based methods. They comprise of mainly spent intact satellites, payloads and rocket bodies at end of life and objects released in the course of spacecraft deployment and operations. This is the domain

of Space Traffic Management (STM) which aims to ensure that the expanding orbital population operates safely by providing a robust framework for on-orbit coordination of activities. This of course encompasses active spacecraft and how they can avoid tracked objects by manoeuvring. It does not, however, include the hazardous untrackable debris population which cannot be avoided.

1.1.2. Space Debris Measurement

As previously mentioned in Chapter 1, debris can be classed as either trackable or untrackable. Trackable debris is measured using ground-based methods such as radar and optical assets, while untrackable debris is modelled statistically. Table 1.1 taken from Krisko [9] gives an overview of the size regimes of various debris sources present in LEO and how they are measured.

Space debris source	**Size range**	**Observation Method**	**Primary instrument (United States)**
Payloads and rocket bodies past end-of-life	>5 cm	Tracked and cataloged	SSN radars
Mission related	<1 m	Tracked and cataloged	SSN radars
Fragments of on-orbit explosions and collisions	<1 m	Tracked and cataloged, <10 cm Observed statistically	SSN radars, Haystack and HAX radars
Sodium potassium coolant droplets	∼1 mm to 5 cm	Observed statistically	Haystack and HAX radars
Solid rocket motor char, slag, and dust	∼100 μm to 5 cm	Observed statistically ground-based tests	Returned surfaces[a],
Ejecta and paint flakes (degradation products)	<1 mm	Observed statistically	Returned surfaces[a]
Meteoroids	<1 cm	Observed statistically	Returned surfaces[a], ground-based optical and radar measurements

[a]Space shuttle, ISS module, HST solar panels, EURECA, and LDEF surfaces

Table 1.1: Space debris sources and size ranges in Low Earth Orbit [9].

Although there are many ways in which larger debris can be tracked, we are currently relying on models to predict the populations of smaller, untrackable debris pieces. Models like ESA's Meteoroid and Space Debris Terrestrial Environment Reference Model (MASTER) and NASA's Orbital Debris Engineering Model (ORDEM) use large sets of observational data (both in situ and ground-based), covering objects which range in size from 10 μm to 10 m [10]. These large sets of observational data are provided predominantly by the Space Surveillance Network (SSN) which is the primary global database for tracking space debris. It is able to track debris down to around 10 cm in LEO and 70 cm in GEO [11], [12]. Below this trackable debris population, radars like HAX, Haystack and Goldstone provide measurements to feed data into statistical models for LEO while telescopes like MODEST do the same for GEO. Table 1.2 outlines the contributing databases for LEO and GEO.

Observational Data	**Role**	**Region/Approximate Size**
SSN catalogue (radars, telescopes)	Intact & large fragments	LEO $>$ 10 cm, GEO $>$ 70 cm
HAX (radar)	Statistical populations	LEO $>$ 3 cm
Haystack (radar)	Statistical populations	LEO $>$ 5.5 mm
Goldstone (radar)	Statistical populations	3 $mm <$ LEO $<$ 8 mm
STS windows & (returned surfaces)	Statistical populations	10 μm $<$ LEO $<$ 1 mm
MODEST (telescope)	GEO data set	GEO $>$ 30 cm

Table 1.2: Space debris observational data for Low Earth Orbit and Geostationary Orbit [13].

Below the limits of these radars is the 1-3 mm region where no measurements exist. The current models used by NASA rely on data interpolation between impact counts from the Space Shuttle missions (under 1 mm in size) and the lower limit of these radars (above 3 mm in size). Figure 9.4 highlights the critical gap in the 1-3 mm debris size range in LEO which NASA interpolate using their ORDEM models.

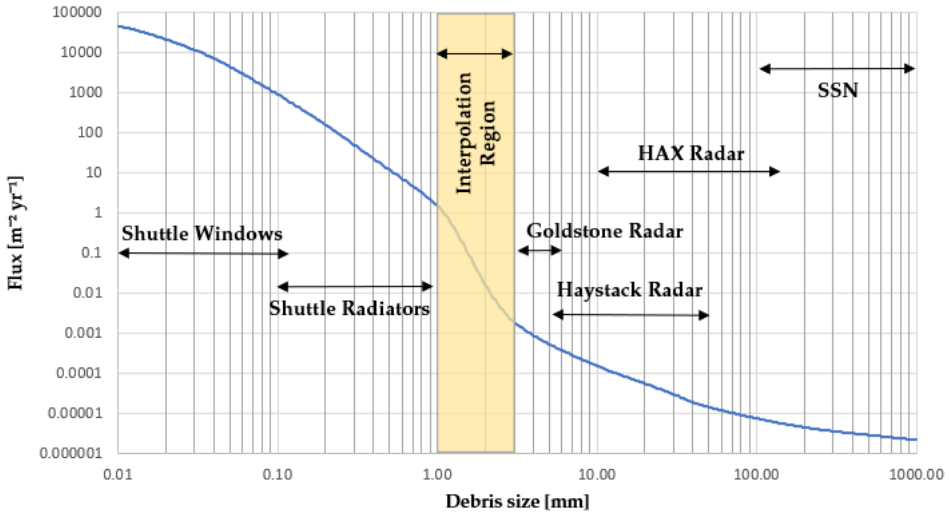

Figure 1.2: Estimated space debris size vs. flux for Low Earth Orbit (altitude = 800 km, inclination = 90°) in 2021 and how each size range is measured.

1.2. Research Objective

The overall research objective that this thesis aims to achieve is to:

Investigate the parameters which influence the momentum enhancement factor that results from a hypervelocity impact into a typical spacecraft solar array, by means of numerical simulations in ANSYS Autodyn. Having obtained this information, explore how these results can aid in validating debris modelling environments.

1.3. Research Questions

In order to realise the research objective, it is important to define the research questions, which will further be complimented by sub-questions. They have been chosen such that the main parameters which influence momentum transfer between a projectile and target can be explored, namely projectile size, shape, material, incidence angle & velocity and target composition. Throughout this study, the targets which will be simulated are typical solar panel layups. As a result of their complex multi-layered structures, solar arrays are very difficult to model within numerical analysis tools like Autodyn. The ability to implement a simplified model will save on computational time and thus enable more trends to be investigated. Understanding the fundamental behaviour of different materials and structural configurations under hypervelocity impact serves as a vital basis for analysing how debris propagates after a collision. Additionally, the effects of initial projectile conditions can have a profound influence on the magnitude of momentum transferred. With this motivation now defined, the following are the main research questions to be explored in this thesis:

1. To what extent can a typical spacecraft solar panel be modelled using hydrocode?
   (a) Is a simplified model a sufficient replacement for a more complex multi-material composition design?
2. How effectively can the momentum transfer from a hypervelocity impact to a solar panel be modelled?
   (a) What is the typical range of MEF values that result from a 1-3 mm size spherical projectile impacting a simplified solar panel target at hypervelocities?
   (b) How does the projectile size and material effect the MEF?
   (c) What influence does the target composition have on MEF?
   (d) What are the effects of using various projectile shapes on both ejecta mass and MEF?
   (e) How does a normal vs. oblique incidence impact effect the ejecta and therefore momentum transfer?
3. Can MEF results be applied to space debris environment validation?
   (a) What are the effects of non-catastrophic debris strikes on the orbital velocity and semi-major axis of a satellite?
   (b) Can satellite perturbation data along with simulated MEF values be used in order to characterise debris strikes?

1.4. Research Outline

The report is divided into the following sections:

Chapter 1. *Introduction,* explains the threat of untrackable space debris and defines the research objective as well as presenting the research questions and outline of this research.

Chapter 2. *Literature Review,* provides the necessary background information required to reach these objectives.

Chapter 3. *Numerical Model Components and Methodology,* describes the introduction to SPH formularisation and discretisations, and the modelling approach used in the numerical simulations throughout this work.

Chapter 4. *Single-Wall Validation,* presents simulation results which have replicated experimental studies and are used to validate the material models employed throughout this thesis.

Chapter 5. *Solar Array Model Formulation,* presents the simplified model of the Hubble Space Telescope solar array which is implemented in Autodyn and compares the impact morphologies of experimental versus numerical scenarios.

Chapter 6. *Projectile Size Study,* subsequently contains impact simulations with varying spherical projectile diameters. The simplified solar array model is used as the target as well as a proposed silicon model.

Chapter 7. *Projectile Material Study,* highlights the main differences between aluminium, glass and copper projectiles in terms of MEF and generated ejecta mass.

Chapter 8. *Projectile Shape Study,* presents comparisons of simulations and generated data for four different projectile geometries - sphere, cone, cylinder and punch shapes.

Chapter 9. *Application to Debris Environment Validation,* describes how this research and research like it can be used as a step in the right direction to validate the space debris environment.

Chapter 10. *Conclusions and Recommendations,* outlines the main conclusions and take away points as well as future recommendations.

Appendix A. *Material Models,* contains all material models used throughout this thesis work.

Appendix B. *User Subroutine,* presents the user subroutine which was written in Fortran and implemented in ANSYS Autodyn.

2

Literature Review

The following chapter presents an excerpt from the extensive literature review that has been preformed prior to conducting this thesis. It aims to provide the reader with a concise overview of the problem in its entirety. It first introduces the potential effects that a hypervelocity impact can have on a spacecraft followed by the ejection processes that occur. Section 2.5 subsequently covers the fundamentals of momentum transfer and enhancement. It finishes up by introducing how hypervelocity impacts are modelled and a review of the fundamental behaviour of materials under high speed impacts.

2.1. Catastrophic vs. Non-Catastrophic Collisions

A common model that is widely used for characterizing hypervelocity spacecraft breakups is the NASA Standard Satellite Breakup Model (SSBM) [14]. This model is employed by space agencies around the world in order to model the space debris environment [15]. According to the SSBM, when a debris strike impacts a spacecraft, the results can be classified as either catastrophic or non-catastrophic.

Catastrophic collisions can be defined as scenarios where both objects that collide become totally fragmented. A catastrophic collision produces not only a small fragment population, but also a larger fragment population which significantly contributes to collisional cascading. As a result, the catastrophic collision contributes to both the short-term and long-term environment [16]. Non-catastrophic collisions on the other hand can be characterized by the fragmentation of the smaller object and by cratering of the larger object. In this instance the majority of the spacecraft remains intact, however, the impact can generate debris that is about 100 times the mass of the impacting fragment. Although the majority of these fragments will be too small to catalogue, there will be some larger fragments that are big enough to track but do not represent a significant contribution to long-term collisional cascading. These can however

represent a significant short-term contribution to the hazard of operational spacecraft [16].

To distinguish between the two classifications, an Energy-to-Mass (EMR) ratio is used which defines catastrophic collisions occurring at an EMR of greater than 40 J/g [14]. In LEO, debris as small as 0.1% of a space object's mass can cause the object to break up into many fragments. A typical LEO catastrophic collision involving a spacecraft may eject hundreds or thousands of fragments large enough to cause a breakup if they collide with another spacecraft [15]. At higher altitudes, the collision velocities are slower and as a result a much larger impactor would be needed to cause a catastrophic breakup [8].

2.2. Effects of Hypervelocity Impacts on Spacecraft

Whether it be an impact from a naturally occurring meteoroid or man-made space debris, both objects have very similar effects when they impact a spacecraft. The following discussion applies equally to both types of particles [17].

When a hypervelocity impact occurs, the effect on the spacecraft depends on multiple parameters associated with both the impactor and the target, namely the size of the incident object and the impact velocity, the impact angle as well as shape and material density of the impactor. For the target, elements such as the location of the strike, thickness and material can all be important in determining the overall effect of the collision. Additionally, the sensitivity to certain failure criteria can play a crucial role in a spacecrafts ability to remain operational post-strike. If an impact occurs between a small debris object and a rather large spacecraft in comparison, this might result in a crater which may have no significant effect on the structural integrity of the impact site, but overtime may degrade a sensor or window and lead to sealing problems. Drolshagen [17] provides an overview of potential effects from hypervelocity impacts:

- Cratering and Ejecta
  - Surface erosion and degradation leading to a change in thermal, optical or electrical properties
  - Degradation of sensors and mirrors, including impacts on internal instruments by secondary ejecta
  - Degradation of windows (even relatively small craters require the exchange of Space Shuttle windows)
  - Sealing problems if e.g. exposed hatches have to be closed

- Structural damage
  - Penetration of spacecraft walls, leading to structural damage of inner subsystems
  - Penetration of pressurised vessels (tanks, manned modules, coolant loops)
  - Cutting of cables or tethers
  - Short circuits
  - Damage to exposed focal plane arrays like charge-coupled devices (CCDs)
  - Complete destruction of impacted spacecraft or spacecraft subsystem by larger object

- Plasma effects
  - Electrical interference
  - Current flow
  - Triggering of electrostatic discharges
  - Light flashes

- Momentum transfer
  - Change of attitude
  - Loss of target lock
  - Loss of formation flying

Although there are many potential effects that a hypervelocity impact may have on a spacecraft, such as cratering and ejecta, structural damage and plasma effects, the aspect which is probably least considered in literature is momentum transfer due to debris strikes [18], [19]. This includes change of attitude with potential temporary loss of target lock or crosslink. This is especially prominent in spacecraft which require high pointing accuracy and attitude stability and may suffer from a disruption in data acquisition as a result of even a small particle strike [17]. Furthermore, it is also necessary to consider spacecraft where gravitationally sensitive technological processes are implemented on-board and where an impact may induce a sudden change in the dynamics of the spacecrafts rotational and translational motion [20].

For instances where a larger, trackable space object is on course to impact a spacecraft, operators can conduct collision avoidance manoeuvres. However, for smaller objects which are untrackable, these collisions may occur unexpectedly. Without sufficient information, such a collision could be considered as an attack by a potential enemy. Additionally, studying the post-strike dynamics of non-catastrophic hypervelocity impacts can help to improve debris modelling, help to attribute anomaly and response, and debris risk assessments for future missions [5].

2.3. Ejecta

The risk of impact between meteoroids or space debris and a spacecraft has always been a threat to operations. A hypervelocity impact can induce significant damage to a spacecraft, its associated subsystems and components and can lead to mission failure. When a collision occurs, a phenomenon unfolds whereby there are large amounts of secondary debris particles produced upon impact. These secondary particles are more commonly known as ejecta and can be defined as the amount of matter produced during a primary hypervelocity impact of a meteoroid/space debris upon a given target or surface [21]. They can be ejected in the form of liquid, solid or gaseous states and are produced from both the target and impactor sample. While the primary collision occurs between the impactor and the target, secondary impacts can also occur when the particles are ejected outwards and in the neighbourhood of the parent body. Any ejecta that doesnt damage the rest of the spacecraft structure can stay within the satellites orbit and contribute to the primary debris flux and increase the collision risk. Due to their large surface area and brittle composition, appendages such as solar arrays are of specific concern when studying hypervelocity impacts and ejecta. According to Rival and Mandeville [22], there exists two different classifications of ejecta, namely, back-scattered ejecta and downrange scattered ejecta [21]:

- Back-scattered ejecta are particles which are expelled outwards into the half-space from which the impactor came. Where an oblique impact occurs, back-scattered ejecta can collide with the external spacecraft elements near the primary impact point.
- Downrange scattered ejecta are particles which travel into the target surface and are produced when the target is a thin plate that can cause spall formation on the rear face or complete perforation. When considering thinner targets, back-scattered ejecta is not as important as downrange fragments (which generally speaking accounts for the largest proportion of the total ejected mass).

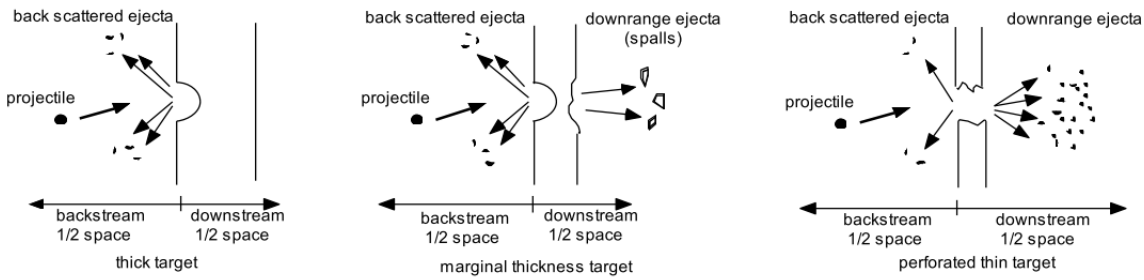

Figure 2.1: Secondary debris produced during HVI: downrange ejecta, back-scattered ejecta [21]

2.4. Review of Ejection Processes

Rival and Mandeville [22] have stated that there are three ejection processes which take place :

1. Jetting occurs when small, high velocity particles are ejected at grazing angles during the infancy of the impact.
2. Cone ejecta are small, high velocity particles which are ejected at constant elevation angle. This creates a cone shape around the impact crater, hence the name.
3. Spall fragments are large ejecta expelled at low velocities and normal to the impact surface.

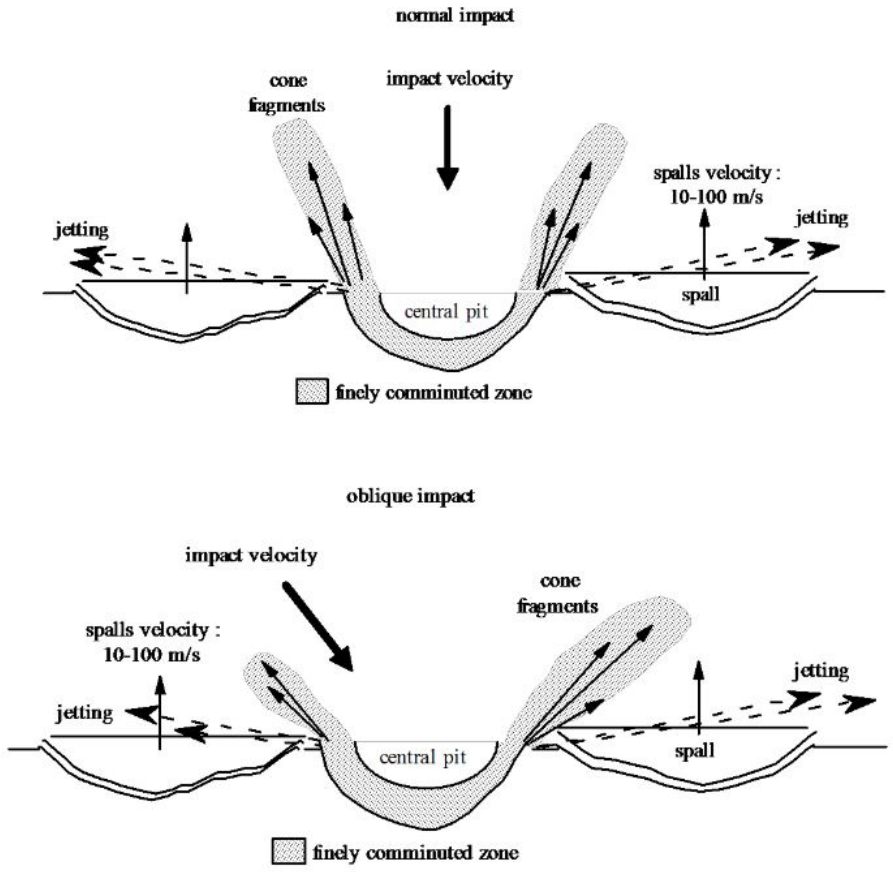

Figure 2.2: Ejection processes (jetting, cone, spall) after normal (top) and oblique (bottom) impact [21]

2.4.1. Jetting

Jetting is the ejection of material from the impactor/target interface while the impactor is penetrating into the target. In the case of the impact of a sphere onto a half-space, the curvature of the projectiles surfaces results in oblique convergence even when the impact velocity vector is perpendicular to the target surface. Thus, in terms of meteoroidal and space debris impacts

on spacecraft, jetting is a very early part of the impact process that occurs as the projectile encounters the target surface and does not require what is normally thought of as an oblique impact. Material is ejected at very high speeds because of the high pressures at the interface. Jetting ceases before the projectile has completely penetrated the target and is unrelated to the main phase of melt and vapor production during crater formation [23], [24].

2.4.2. Debris Cone

Cone ejecta are produced by tensile and compressive rupture of the target around the centre of the crater that has formed from impact. These cone fragments are ejected at about the same elevation angle as the crater itself. This gives rise to the conical shape of the debris cloud at the impact site [21].

2.4.3. Spallation

Spall fragments are large ejecta expelled at low velocities and normal to the impact surface. They are generated from tensile rupture of the target material near the primary impact site. This occurrence is particularly prominent for brittle materials like glass and hard metals. When considering solar arrays, their multilayer structure is favourable for large crack propagation and delamination at the interfaces. Due to these said occurrences, the ejected spall mass is rather larger than on a purely brittle homogeneous surface [21]. Rival et al. [25] performed an examination of HST solar cells which concluded that the spall mass could reach 90% of the total ejected mass for impact craters in the millimetre size range. The spall mass can be calculated from the difference between the total ejected mass and the cone fragments mass.

2.5. Momentum Transfer

Momentum, simply put, is the product of an object's mass and velocity. Momentum transfer in a HVI sense can occur when a kinetic projectile of mass m_p strikes a target of mass M at a velocity v_p. It is often defined as $M \times \Delta V$. Due to the ejecta expelled in the backwards direction, some of the momentum is carried away and therefore the momentum transferred can exceed the projectile momentum $m \times v_p$ [26]. Momentum transfer is often characterised by a momentum enhancement factor, MEF.

The most basic assumption that can be made is to consider that the impactor is absorbed by the target, or in other words, the space debris sticks to it. This results in a single composite body after the impact has been made and the spacecrafts momentum has been changed by the momentum of the impactor [27]. However, since most impacts tend to excavate material from the surface and even penetrate the target completely, a more complex method of determining momentum transfer is needed. This ejecta material that is expelled outwards as a result of an

impact causes a reaction on the entire body. Even though the total momentum of the system (including ejecta) will be conserved, a phenomenon known as momentum enhancement allows the momentum change of the spacecraft to be larger than the momentum of the impactor without defying the conservation of momentum i.e. the change in target momentum after the impact is greater than the original momentum of the impactor [27]. During a hypervelocity impact, the momentum of the impactor is conserved in [28]:

- The internal momentum transferred to the target during the impact-impulse,
- The ejecta from the impact zone surface of the solar panel,
- The material spalled from the non-impact surface of the solar panel,
- The forward momentum of all matter that leaves the non-impact surface when penetration of the target occurs.

Momentum transfer is quantified by a momentum enhancement factor, MEF, which is a dimensionless quantity and determines the efficiency of the momentum transfer. It is defined as the ratio of change in target momentum following the impact to the projectile momentum [29] and can be expressed in vector form according to Equation 2.1.

$$M_t \Delta \boldsymbol{v}_t = m_p \boldsymbol{v}_p - \sum m_e \boldsymbol{v}_e = \left(1 - \frac{\sum m_e v_e \cos\alpha}{m_p \boldsymbol{v}_p}\right) m_p \boldsymbol{v}_p = MEF m_p \boldsymbol{v}_p \tag{2.1}$$

Where:

- M_t = target mass (kg)
- Δv_t = change in target velocity (m/s)
- m_p = projectile mass (kg)
- v_p = projectile velocity (m/s)
- m_e = ejecta mass (kg)
- v_e = ejecta velocity (m/s)
- α = ejecta spread angle (deg)
- MEF = momentum enhancement factor

A simplified scalar form where only ejecta momentum normal to the target is considered can be defined by Equation 2.2.

$$MEF = \frac{\Delta p_t}{p_p} = \frac{p_p - p_e}{p_p} = 1 - \frac{p_e}{p_p} \tag{2.2}$$

Where:

- p_t = target momentum (kgm/s)
- p_p = projectile momentum (kgm/s)
- p_e = ejecta momentum (kgm/s)

Equation 2.2 shows that the ratio of ejecta to projectile momentum is the driving factor which governs the MEF. The higher the ratio, the lower the MEF. Equation 2.3 reveals how the total ejecta momentum is comprised of both back-scattered and downrange ejecta momentum.

$$p_e = p_{back} + p_{down} \tag{2.3}$$

The sign of the back-scattered ejecta momentum is negative relative to the downrange ejecta momentum which is positive. If complete perforation does not occur and/or there is no downrange ejecta generated, the p_{down} term will equal to 0 and p_e will be negative, resulting in an MEF greater than 1. Otherwise, if the p_e term is positive, the MEF will be less than 1. This means that the quantity of back-scattered ejecta momentum and downrange ejecta momentum play a vital role in MEF calculation. Assuming complete perforation Equation 2.4 shows that for a given projectile momentum, the higher the total ejecta momentum, the higher the ratio and hence the lower the MEF.

$$MEF = 1 - \frac{p_{back} + p_{down}}{p_p} \tag{2.4}$$

To date, studies have dealt with momentum transfer involving targets such as rock [30], [31], meteorites [26], [32], [33], aluminium [31], ice [31], pumice [34], dust shields on the Giotto Halley Mission [28], metal [35], spacecraft [18], [29] and spacecraft shielding [36]. Although these investigations set out to obtain values of the momentum enhancement factor for their respective tests, none of the investigations consider spacecraft solar arrays or modern state-of-the-art spacecraft structures like CFRP sandwich panels.

2.6. Modelling of Hypervelocity Impacts

Hydrocodes, also called wave-propagation codes, are time-explicit code packages that can be used for the numerical solution of mathematical models of high energy wave propagation phenomena [37]. By definition, "*hydrocodes explicitly simulate the temporal evolution of the incremental deformation process and update the changing geometry in each time step of the calculation by solving the fundamental conservation equations supplemented by constitutive equations describing the material behaviour*" [38]. Hydrocodes lend themselves extremely well when modelling hypervelocity impacts where a kinetic energy projectile uses the energy of its motion to penetrate a target. Zukas [39] in his book titled "*Introduction to Hydrocodes*" goes into great detail about the processes that occur during an impact. Zukas highlights that when a hypervelocity impact takes place, compressive stress waves are generated in both the impactor and the target. These compressive stress waves are immediately followed by shear waves which move at a slower pace. There is also the potential for relief waves to be generated during impacts with significantly higher velocities which are caused by lateral free surfaces. These manifest themselves as a 2D stress state behind the compressive front for normal impacts and a 3D stress sate for oblique impacts, since now asymmetric bending waves are involved. Both the compressive and shear waves will spread in the target until they interact with a material interface or a free surface. At this point, tensile waves can be generated in order to satisfy the boundary conditions and if the amplitude of the tensile stress pulse and its duration at a point in the material are sufficient, material failure by a variety of mechanisms can occur [39]. This allows hydrocodes to successfully model shock energy transmission and perform impact testing which compliments the use of accelerators such as light-gas-guns in a laboratory setting, see Figure 2.3.

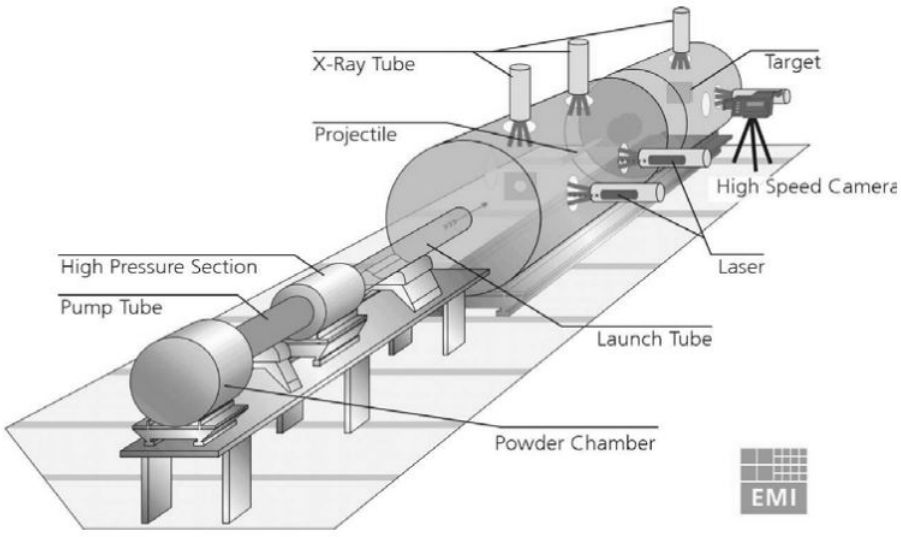

Figure 2.3: System components of the large 2-stage light-gas gun and its associated diagnostic equipment at the Ernst-Mach-Institute [40].

These accelerators can monitor and analyse the propagation of the generated debris cloud and the dynamics of the projectile penetration into the target. Although this method of interpreting a hypervelocity impact can aid in the design of spacecraft shielding or determining MEF, accelerator technology is not currently capable of recreating on-orbit collision velocities of up to 15,000 m/s in LEO [3]. LGG tests can be used to validate the accuracy of numerical models which can then subsequently be used as cheaper alternatives to LGG testing and attempt to fill in the effects at higher velocity regimes. Caution must be taken however as extrapolation is always questionable and this must be kept in mind when interpreting analytical results at higher velocities.

The basic working principal of a hydrocode numerical tool is to solve a set of conservation equations for mass, momentum, and energy, along with adjoining Equations of State (EOS), which include shock phenomena under consideration of material response with change of state [40]. This leaves partial differential equations which can be integrated in time, across a spatial body fixed (Lagrangian) grid or an inertially fixed (Eulerian) grid. There are benefits and limitations to both methods, as will be discussed. The Lagrange method comprises of a grid which distorts with the material. It is a computationally fast method with good traceability of body-related grid-point histories and defines the material interfaces/boundaries well. This is all at the expense of large grid distortions during an impact [40]. The Euler method on the other hand comprises of a fixed grid through which material flows. This is even more computationally expensive but allows for the mixing of materials and is better suited to modelling larger deformations.

For approximating the spatial derivatives in the underlying partial differential equations, several different methods exist, which can be classified into mesh-based methods and mesh-free methods. The individual methods are formulated in either Lagrangian or Eulerian kinematics and are specifically derived for certain structural components or loading conditions depending on the requirements [41]:

1. Mesh-based approaches include Finite Elements Method (FEM), Finite Volumes Method (FVM) and Finite Differences Method (FDM) [38]. These numerical methods have been used to solve complex engineering and science problems like those in the field of Computational Solid Mechanics (CSM) and Computational Fluid Dynamics (CFD). These approaches have proven themselves to be extremely helpful in solving both differential equations and partial differential equations associated with the phenomena being studied [42]. However, these mesh-based methods are not without their disadvantages with regards to certain applications. By using a grid/mesh, these approaches face some difficulties when handling situations that involve free surfaces, deformable boundaries, moving interfaces, and extremely large deformation and crack propagation [43]. During a hypervelocity impact, specific features are present such as large deformations, large inhomogeneities, moving material interfaces, deformable boundaries, and free surfaces. Shock waves also propagate through the colliding bodies and represent a fluid-like behaviour. All of these

aspects of a HVI ultimately result in an extremely difficult situation for grid based numerical methods to cope with [44].

2. Mesh-free methods include Material Point Method (MPM) and Smoothed Particle Hydrodynamics (SPH). These approaches have gathered momentum over the past few years as they continuously prove themselves to be a more effective way of managing certain complex engineering problems. Within the domain of modelling hypervelocity impacts, SPH is particularly useful and will be discussed further in section 2.6.1. Although meshless methods are better suited to hypervelocity impacts, they still have some shortfalls, particularly tensile instability and computational cost [45]. Nonetheless they are the preferred method when handling a HVI [46].

2.6.1. Smoothed Particle Hydrodynamics

SPH is a meshless technique which uses Lagrangian nodes that are not physically connected by a grid, but instead use mathematical interpolation functions to track their relative motion [40]. Originally developed by Lucy [47], Gingold and Monaghan [48]–[50], Monaghan [51]–[53] and Benz [54] to simulate the formation of stars, it avoids grid distortion and reaps the benefits of both Lagrangian and Eulerian methods. The main advantage of the SPH method is to bypass the need for a numerical grid to calculate spatial derivatives. This avoids the problems associated with mesh tangling and distortion which generally occur in Lagrangian analyses involving large explosive loading events. This makes the SPH method the most suitable technique when modelling a hypervelocity impact [45], [55]–[57].

Over the past few years there have been some improvements proposed for the purely SPH, meshless method [58]–[61]. However, it appears that a combination or hybrid particle-mesh method is better suited when modelling HVIs [62]–[64]. Johnson et al. [65]–[69] conducted many studies investigating different coupling methods and obtained very beneficial results. Another study by He et al. [70] applied a finite element-smoothed particle hydrodynamics adaptive method (FEM-SPH) to the simulation of a hypervelocity impact which produced a debris cloud. This coupling approach achieved good fragment identification which is a more difficult task for the traditional meshless method. Another example of this coupling approach is in a study by Schimmerohn et al. [38] wherethey developed a software tool PHILOS-SOPHIA that models hypervelocity collisions using hydrocode simulations. They compared two specific techniques. The first method couples a meshless smoothed particle hydrodynamics (SPH) method with a mesh-based finite element method (FEM). The FEM-SPH approach begins with an FE model in which distorted elements are adaptively converted into particles. The second approach, the eroded nodes method, replaces deleted elements with simple mass points. These simple mass points can also be referred to as eroded nodes, hence the name. Eroded nodes carry the mass and linear momentum of the eroded elements and interacts with other surface elements but not with each other. The study concluded that the FEM-SPH method, whose particles conserve the volume of the converted elements and can still absorb pressure and shear forces, better

reproduce specific features of the fragment cloud expansion. It also concluded that the eroded nodes simplification significantly reduces the computing time and can be a pragmatic approach for large scale models. Where geometrically large models are being simulated, this hybrid approach has proved to e promising. However, for much smaller and simplified models, the SPH method by itself is sufficient.

2.6.2. ANSYS Autodyn

Hydrocodes were developed in the 1950's in order to simulate the physical effects of nuclear weapons and since then, have become far more commercial with hydrocode being implemented in software packages like ABAQUS, ANSYS Autodyn, CTH, DYTRAN, EPIC, HEMP, HULL, LS-DYNA, OURANOS, PAM-SHOCK and RADIOS [41]. The ANSYS Autodyn software has proven to be a reliable choice and has been successfully used to model debris cloud interactions with multiple Whipple shields as a result of hypervelocity impacts [71].

ANSYS Autodyn is an explicit analysis tool for modeling and simulating nonlinear dynamics and the interaction amongst solids, fluids and gases. It provides a user friendly graphical interface which allows for a smooth and easy set up, running, and post processing of problems. Within the ANSYS Autodyn software package there are a range of solvers available [72] such as:

- Finite element (FE) solvers for computational structural dynamics.
- Finite volume solvers for fast transient Computational Fluid Dynamics (CFD).
- Mesh-free particle solvers for high velocities, large deformation, and fragmentation (SPH).
- Multi-solver coupling for multi-physics solutions including coupling between FE, CFD, and SPH.
- A wide suite of material models incorporating constitutive response and coupled thermodynamics.

ANSYS Autodyn has also been used by many studies in an attempt to characterise and model certain materials under partially and fully damaged states. These studies have lead to an improvement in both experimental and numerical analysis techniques when predicting the effects that a HVI has on materials, particularly composite structures. This includes aluminum honeycomb cored carbon fiber reinforced polymer composite based sandwich structures (CFRP/Al HC) [73], aramid weave epoxy composite panels [74] and classes of ultra-high molecular weight polyethylene (UHMW-PE) such as Dyneema® HB26 [75], [76]. The development and variety of the composite structure models within ANSYS Autodyn as well as the ability to implement multi-solver coupling between FE and SPH methods drove the software selection.

2.7. Behaviour of Materials under Impact

The main differences between low and high speed impacts are the physical phenomena involved and the ways of dealing with these phenomena. When a low speed impact occurs, the regime is essentially elastic for brittle materials and elastoplastic for ductile materials. In both cases, apart from the possibility of brittle fracture for materials such as ceramics or glass, the projectile and the target undergo little permanent deformation. When the impact velocity reaches several thousand meters per second, the situation is totally different because the impact phenomenon and the penetration of the projectile into the target are controlled by the dynamic properties of the materials. Locally, the stresses associated with the impact can exceed the resistance of the material by several orders of magnitude, and the behavior of the materials present can be partially assimilated to that of a fluid; this is then referred to as a hydrodynamic regime. In these cases, the phenomenology of the impact depends on the configuration of the system. Characteristics like projectile size, shape, speed and material and target material and relative thickness all become important factors in determining how the impact evolves. From a phenomenological point of view and in terms of damage, it is possible to separate the impact into three phases which underline the importance of the wave propagation phenomenon in the study of high speed impacts:

- **Hydrodynamic phase:** in the first moments of impact, the energy transmitted to the target and the energy retained by the projectile are distributed. Upon projectile/target contact, a shock wave is generated and propagates. It provides the mechanism for transferring kinetic energy from the projectile to the target. The behavior of materials is then hydrodynamic. This is the stage of formation of the hemispherical crater and the beginning of the ejection of material from the excavation of the crater.
- **Damage under impact:** during the propagation of the shock in the target, due to the fact that we are dealing with a divergent spherical wave, the stress decreases in 1/r (where r is the distance between the point of impact and a point inside the target) but may continue to damage the target (plasticisation for ductile materials or fragmentation for brittle materials). Generally, due to the attenuation of the intensity of the shock, the affected areas are very close to the crater.
- **Damage by reflection of elastic waves and stress relaxation:** even if the elastic limit of the materials is not reached, the propagation or reflection of the attenuated waves can lead to damage to the target. Thus, on ductile and brittle targets of medium thickness subjected to impacts at high speed, a zone of damage is often observed near the free surface: this is the damage by spalling due to the traction wave produced by wave reflection.

2.7.1. General Characteristics of Damage

The morphology of impact craters is very different depending on the nature of the material and target impacted. Figure 2.4 illustrates some classic examples of impacts on different materials and structures. On a ductile material such as a metal in Figure 2.4a, the crater is generally hemispherical and surrounded by a lip of molten material; if the target is not semi-infinite but of low thickness, a "blister" is sometimes observed due to the attached spall. The ratio of crater depth to particle diameter increases with the density of the projectile. As can be seen in Figure 2.4b, the damage morphology on a brittle target is far more complex. Shards from around the central crater and the molten area, along with the projectile material, is often ejected due to the shattering of the glass. On composite materials such as the substrate used on the solar cells of the Hubble Space Telescope (Figure 2.4c), there is a partial fusion of the resin and the fibers; the fibers are severed by the projectile. There is also significant delamination. Finally, structural effects are also sometimes observed in damage caused by high-speed impacts. They are usually due to the propagation and reflection of waves on the free edges and free surfaces of the target. For example, on a multilayer structure such as a solar cell, the consequences of an impact can be catastrophic on the cell structure due to the phenomenon of impedance mismatch due to stacking or geometry: the reflection of the shock wave on the interfaces induces loads which create long fractures and large fragments of the protective glass are ejected, see Figure 2.4d.

(a) Aluminum target [77]

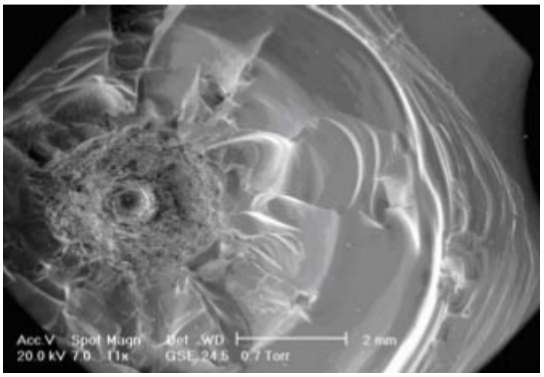

(b) Fused Silica [78]

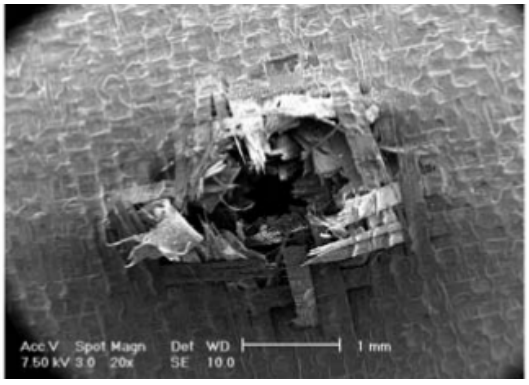

(c) HST Solar Array Substrate [79]

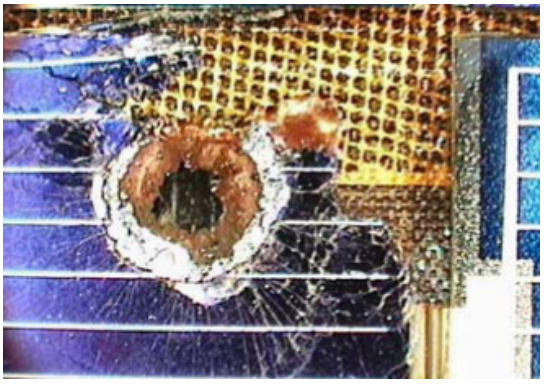

(d) HST Solar Array Laminate [80]

Figure 2.4: Hypervelocity impact damage on different types of targets.

It is evident that there are differences in damage morphologies between brittle and ductile materials during a hypervelocity impact. In general, brittle materials are observed to have lower fracture toughness and higher yield strength than their ductile counterparts, resulting in features such as cracking, shattering and spallation. Cracks tend to propagate radially from the primary impact crater resulting in very large volumes of ejecta being expelled, particularly for thin targets. These brittle ejecta particles are expelled at very high velocities and undoubtedly play a critical role in momentum transfer. Not only this, but due to their brittle composition and large surfaces exposed to the debris environment, solar arrays also represent a very real threat to themselves as well as the increase in space debris.

2.7.2. Multi-Layered Structures

Studies have shown that multi-layered structures such as HST solar panels which are composed of brittle and ductile materials actually result in an increase in spall phenomenon due to delaminations between cover-glass and silicon layers [25]. Central pit formation is controlled by hydrodynamic process and should not be that different in multi-layered HST structure compared to a single homogeneous target. On the other hand, spall behaviour does vary as it depends on wave propagation and is very sensitive to the structure of the material. New rarefaction waves are generated at the interfaces between the different target layers and cause further delamination. This results in an increase in probability of brittle rupture of the medium due to tension waves.

A distinct step structure is clearly visible among the glass and silicon layers in Figure 2.5. It is observed that the stacking of these brittle layers seems to amplify the spalling phenomenon and play an important role in the type of damage observed. This step structure is typical of a brittle materials damage morphology as shown later in Figure 4.3.

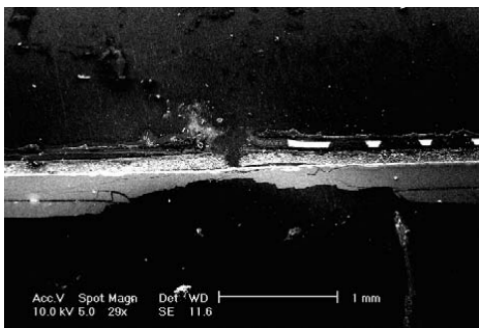

(a) No perforation but chipping of the protective glass and silicon layers

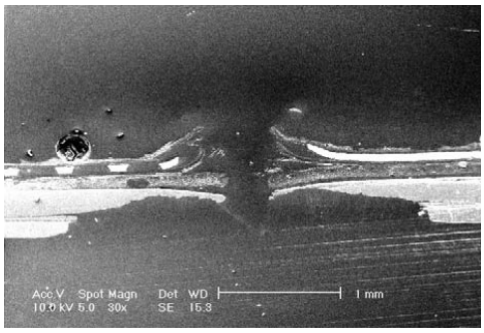

(b) Complete perforation with delamination of the composite substrate.

Figure 2.5: SEM (Scanning Electron Microscope) images of HST solar cells post hypervelocity impact [81].

2.8. Literature Review Conclusions

It has been show that there is a significant knowledge gap in the 1-3 *mm* size regime for space debris. As these objects are untrackable and only statistically observed, regular unannounced and unavoidable collisions occur which can have devastating consequences for spacecraft. Among the most susceptible spacecraft components to debris strikes are the solar arrays which boast very large exposed surface areas. Although strikes can occur on a daily basis without operators ever knowing, it has been shown that spacecraft can remain fully operational even when numerous hypervelocity impacts have occurred. Being able to detect and classify these impacts may help to attribute future anomalies and at the core of this is understanding the momentum transfer induced by different impact conditions.

There have been very few studies designated to understanding the momentum transfer that occurs between orbital debris and spacecraft. Moreover, to the best of the knowledge of the author, no studies have been conducted to determine momentum enhancement factors into satellite solar arrays. This forms an interesting topic due to the potential for space debris environment validation from studying how different impacts can be linked to satellite perturbations. The literature review has highlighted that through numerical analysis, it is possible to simulate speeds in the hypervelocity range which are unattainable with conventional modern-day equipment. These speeds are much more typical of orbital and collision velocities in LEO where there are large amounts of operational satellites, and much more planned for the near-future.

Understanding the fundamental behaviour of different materials and structural configurations under hypervelocity impact serves as a vital basis for analysing how debris propagates after a collision. Additionally, the effects of initial projectile conditions can have a profound influence on the magnitude of momentum transferred and this will be explored in greater detail throughout the remainder of this thesis study. By implementing a model of a typical solar array into ANSYS Autodyn and subjecting it to a range of different hypervelocity impacts, the momentum enhancement factor can be obtained. These values will allow the actual momentum transferred to a target to be determined and from this, help to associate a change in a spacecrafts motion to a particular debris strike classification. Obtaining these values is expected to help fill the knowledge gap surrounding the 1-3 *mm* debris size range and validate debris models.

3

Numerical Model Components and Methodology

This chapter introduces the numerical modelling tools implemented in the context of this thesis. It aims to provide an insight into the basic principles of smoothed particle hydrodynamics as well as an understanding of how models are set up in ANSYS Autodyn. This includes an explanation of the material models used, the 2D axial symmetry that was implemented, the boundary conditions that were set and finally the user subroutine which was created in order to extract custom data from Autodyn.

3.1. Material Modelling Components

This section presents the different components which constitute a material model. It also explains the reasoning behind the selection of these specific models, considering that there are multiple models available for any given material.

3.1.1. Equation of State

An Equation of State (EOS) characterises the hydrostatic behaviour of stress and strain. The relevant EOSs used in this study are characterised by the interaction between pressure and other state variables such as energy and material density within a medium [82]. Many EOSs exist for a variety of different applications among numerical simulations. The EOS formulations which are applied in the context of this thesis are the Mie-Grüneisen EOS for AL 2024-T4 and a simple polynomial one for glass which is a general form of the Mie-Grüneisen EOS and is energy independent. All material models in the in-built Autodyn material library use the Mie-Grüneisen EOS for aluminium and the simple polynomial EOS for glass, justifying the selection for their use. They are also widely used throughout literature.

3.1.2. Strength Model

Strength models are used in order to define the deviatoric relationship between shear stress and shear strain of the material. This in turn governs the yield criteria when the material undergoes loading from a HVI. The Steinberg-Guinan is one such model which was developed specifically for metallic materials [83]. It is particularly well suited to high strain rates of $\dot{\epsilon} \geq 10^5 s^{-1}$ which lies in the regime of typical hypervelocity impacts where strain rates are in and around $\dot{\epsilon} \geq 10^6 s^{-1}$ [84] and is used as the strength model for Al 2024-T4. Glass on the other hand uses a Johnson-Holmquist 2 (JH2) model which is used for brittle materials subjected to large strains and strain rates and high pressures and is commonly used throughout literature [85].

3.1.3. Failure Model

Following a HVI, failure of the material is determined by the implementation of a failure model. Al 2024-T4 uses a minimum hydrostatic tension failure model. This is a relatively straight forward failure model which states that if the tensile stress in the material, p, exceeds the minimum defined tensile pressure, p_{min}, failure initiation occurs and the material fails instantaneously [41]. The model limits the maximum tensile pressure in the material as:

$$p \leq p_{min} \tag{3.1}$$

Verheijen [84] establishes good reasoning for selecting this failure model, stating that it is less computationally expensive [72] and displays superior fragment mass distributions when compared to other models such as the Grady Spall model [86].

Glass uses a JH2 gradual failure type which results in damage being incrementally applied to the material strength as it accumulates. This failure model is specifically used with the polynomial EOS and JH2 strength model.

3.2. Smoothed Particle Hydrodynamics Discretisation

As previously discussed in Section 2.6.1, SPH is a meshless technique which uses Lagrangian nodes that are not physically connected by a grid, but instead use mathematical interpolation functions to track their relative motion [40]. The behaviour of a body is modelled by a set of mass particles that interact with each other via spheres of influence. As opposed to classical finite element methods, SPH has time varying nodal connectivity. This variation of influence between each particle and between each time step make it possible to model more easily and more realistically problems involving large deformations such as hypervelocity impacts.

Smoothed particle hydrodynamics works by discretising objects into single interpolation points. These particles are then used to determine material properties at these junctions based on the

contribution of all neighbouring particles n. This is outlined in Equation 3.2.

$$f(\boldsymbol{x}) = \sum_{i=1}^{n} (\boldsymbol{x}_i)\, W\left(\left|\boldsymbol{x} - \boldsymbol{x}_i\right|\right) \frac{m_i}{\rho_i} \tag{3.2}$$

Where:
$\boldsymbol{x}$ = node location vector (m),
m = mass (kg),
ρ = density (kg/m^3),
W = weighting function

Autodyn uses a kernel B-spline weighting function W as the smoothing function as illustrated in Figure 3.1. This determines the influence that neighboring particles have on the current interpolation point. In Equation 3.3, $R = r/h$ where r is the distance between the current point and the neighboring particle i and h is the smoothing length which defines the support area of the smoothing function W. Smoothing length is defined by the user in Autodyn as the "particle size" and Autodyn uses this value to place nodes at a distance of $1h$ from each other.

$$W(R,h) = \frac{3}{2\pi h^3} \begin{cases} \frac{2}{3} - R^2 + \frac{1}{2}R^3, & (0 \le R < 1) \\ \frac{1}{6}(2-R)^3, & (1 \le R < 2) \\ 0, & (R \ge 2) \end{cases} \tag{3.3}$$

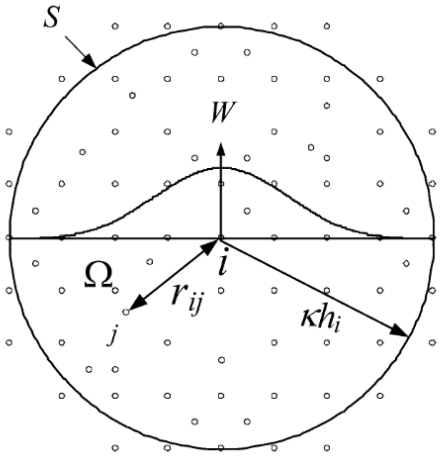

Figure 3.1: Illustration of SPH particle approximation for a 2D problem domain Ω with interpolation kernel W and surface S.

3.3. 2D Axial Symmetric Simulations

Autodyn has the capability of modelling in both 3D and 2D. The 3D configuration can be run with or without implementing symmetry but requires a massive amount of computational power, something which was not available during this thesis. The 2D setup offers an excellent alternative solution which does not sacrifice accuracy, although comes with some limitations of its own.

Autodyn 2D leverages symmetry in order to cut down on computing time. Both planar and axial symmetry options are available. In this particular instance, 2D axial symmetry is used throughout the rest of this work. 2D sketches generated in the x-y plane within Autodyn are rotated around the x-axis to create a 2D representation of a 3D model, as seen in Figure 3.2.

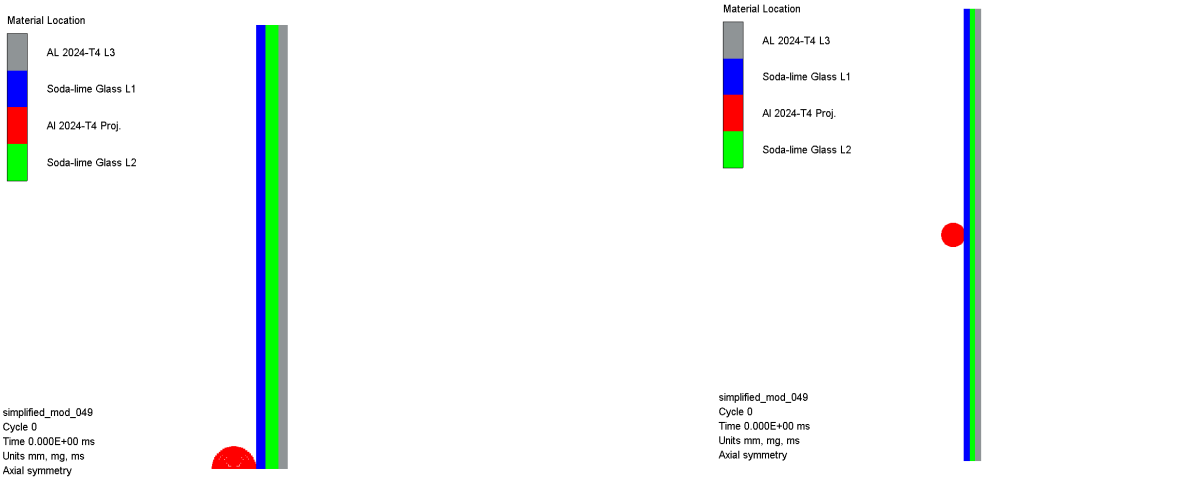

(a) 2D sketch generated in the x-y plane.

(b) 2D sketch generated in the x-y plane and rotated around the x-axis.

Figure 3.2: Autodyn 2D Axial Symmetry.

Using 2D axial symmetry in this way means that the targets will all be circular disks instead of square targets, as seen in Figure 3.3. A single 3D simulation was run in order to make sure that the results obtained using 2D axial symmetry were accurate. It is worth nothing that all the results in the 2D simulation had to be multiplied by Pi in order to match the 3D results. This was simply a case of multiplying the x-momentum values out to form a circle in 3D space. The results showed that the 2D and 3D MEF values obtained were identical, with the 2D simulations taking much less time to complete.

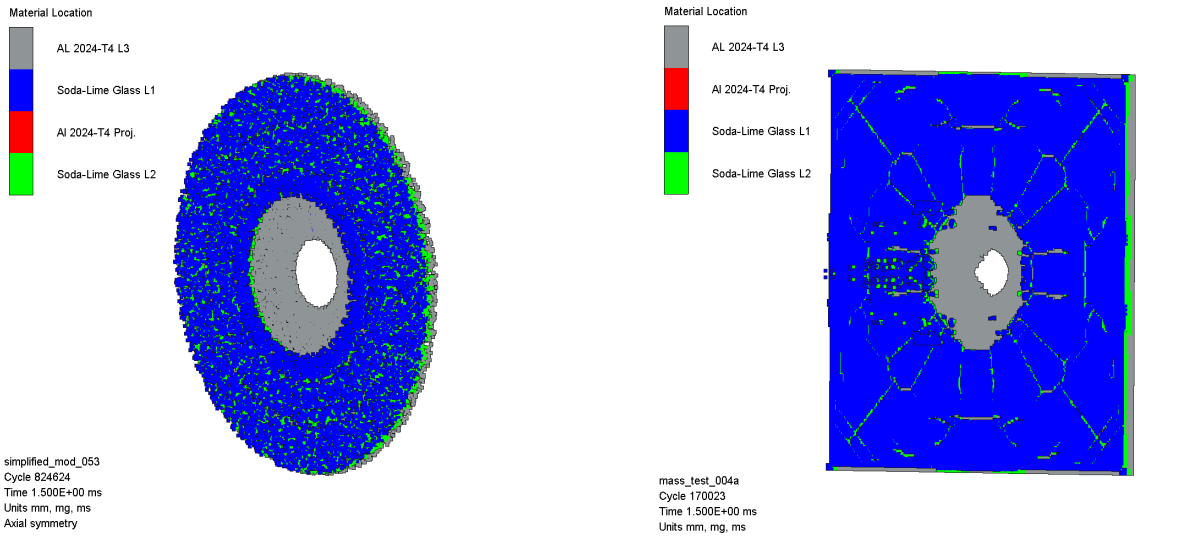

(a) 2D target with Axial Symmetry

(b) 3D target with symmetry in the Y and Z planes

Figure 3.3: Fragment plots of 2D (left) and 3D (right) targets. The plots only show elements that contain material that has not failed.

One of the other main differences between the 2D and 3D models, albeit insignificant when comparing MEF, is the absence of radial cartwheel fractures surrounding the circular spall zone. These can be seen in Figure 3.4b which compare very nicely to actual HST solar panel impact morphology as highlighted in Figures 3.3a and 3.3b. Nonetheless, both the 2D and 3D Autodyn models display very similar conchoidal fracturing to one another as well as to the real life impacts shown in Figure 3.4.

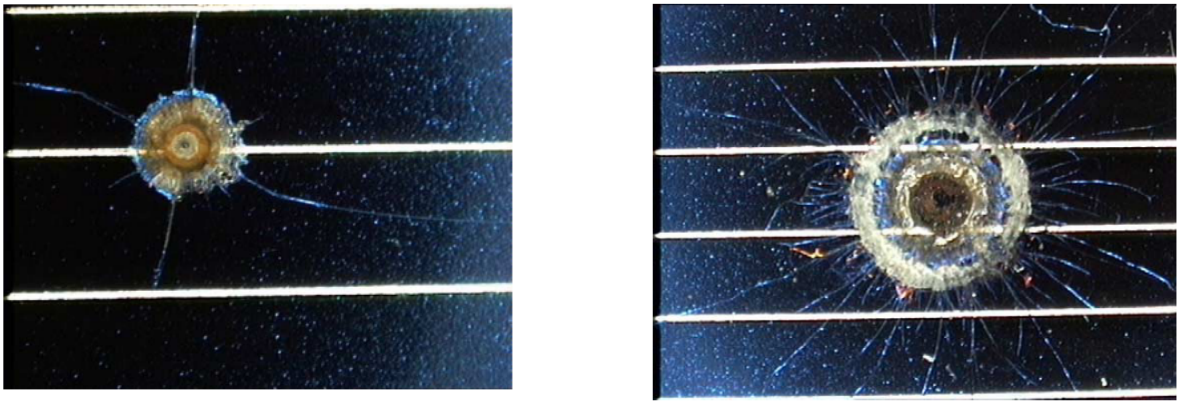

(a) Crater diameter 1 mm

(b) Crater diameter 2.4 mm

Figure 3.4: Hypervelocity impacts into HST solar cells [80].

As mentioned, there are however some limitations to consider. By using 2D axial symmetry, only impacts normal to the target can be simulated. Impact incidence angle cannot be changed and therefore means that research question 2e cannot be answered during this thesis. Since the propagation of debris particles is not important when calculating MEF values, 2D axial

symmetry is a very efficient way to set up the numerical analysis. This would be considered critical if the damage to secondary objects was being considered and the path of the debris post impact needed to be analysed.

3.4. Boundary Conditions

For all simulations conducted in this project, a boundary condition of 0 m/s is set on the top row of SPH particles for the x- and y-direction. This ensures that the target is constrained around its circumference and will not move when struck by the projectile.

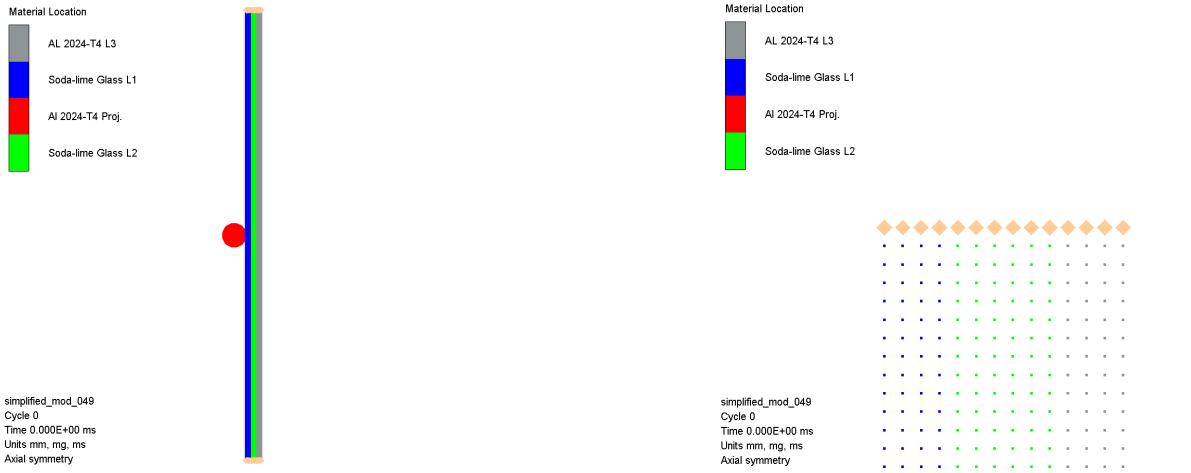

(a) Regions where the boundary is applied to the target.

(b) Enlarged view focussing on the top row of SPH particles.

Figure 3.5: Constraints applied to the boundary of the target.

3.5. ANSYS Autodyn User Subroutine

Within Autodyn, users have the option to select individual SPH particles and read out data pertaining to that particle such as position, velocity, mass and so on via the "Examine" feature. This is useful to some extent, but when dealing with a model with thousands of nodes, a more efficient method of extracting data is required. Users can opt to write their own custom subroutines which are written in Fortran code. Some example user subroutines are provided in the *Autodyn User's Subroutines Guide* [87] which serve as a nice starting point, but in order to create more complex custom models, a decent understanding of the Fortran programming language is required.

In order to write these subroutines, the following compilers are required:

- Microsoft Visual C++ 2017
- Intel Fortran 17.0.4

The approach which was decided upon was to implement a "numerical fence" as shown in Figure 3.6. When an SPH node passed through this fence its ID, position, velocity components, and mass were recorded in a .dat file. The approach makes use of the EXEDIT function in the usrsub2.f90 module which is designed for user customisation. See Appendix B for the full code.

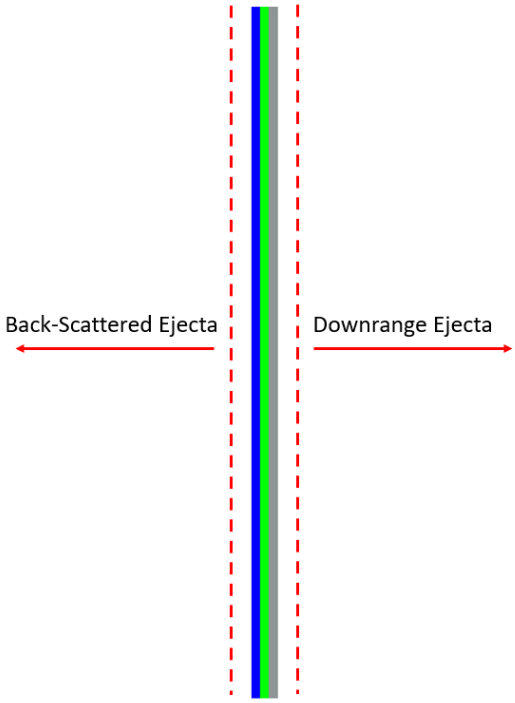

Figure 3.6: Numerical fence method implemented in Autodyns user-subroutine EXEDIT.

All targets modelled in this thesis had their origin at (0,0) and the fence was applied at the boundary of the target. Depending on the thickness of the target, these boundaries were set to different values. For example, the 0.7 mm targets had a back-scattered ejecta boundary limit of roughly $x = -0.5mm$ and a downrange ejecta boundary limit of $x = 1$. Anything contained between these limits was considered to be the target. The target only extended from x = 0 mm to x = 0.7 mm, so extra margins on either side were added to ensure that no intact target material was included. Once the data belonging to these ejecta particles had been stored, the x-momentum of each one could be calculated and the MEF obtained from Equation 2.2.

4

Single-Wall Validation

In this chapter, a validation study is conducted to ensure that the Autodyn models are yielding results comparable to real-life tests. Due to the high costs associated with hypervelocity impact testing, no specific experimental data could be obtained and so results were compared to the limited MEF data that was available. A set of MEF data was identified for aluminium, making the models relatively straight forward to validate. The same was not true for glass, and in the absence of MEF data, improvisations had to be made. This meant trying to replicate impact crater measurements from experimental data and then deduce what the expected MEF values would be. Glass models have been extensively studied in literature and Autodyn contains two well-validated material models. The only difference between them is the value for the hydrostatic tensile limit, and so a strength variation study is carried out in order to get as close as possible to experimental measurements.

4.1. Aluminium Models

Very little data exists when it comes to momentum transfer due to HVIs. This can be attributed to the fact that running HVI experiments is very costly and requires large facilities to house the equipment. Furthermore, any HVI data that does exist is not necessarily concerned with momentum enhancement, but rather the damage that an impact can cause on specific space materials and how the debris fragments propagate. Nonetheless, studies conducted during the U.S. space programme in the 1960's by Denardo and Nysmith [88] present MEF values which can be used to validate aluminium single-wall models.

In this study, spheres of Al 2017-T4 with diameters of 1.5875, 3.175, 6.35 and 12.7 mm were launched into semi-infinite Al 2024-T4 and Al 1100-0 targets at varying velocities. The plate dimensions were 254 x 254 x 50.8 mm. A light-gas gun was used to launch the projectiles and a ballistic pendulum was adopted to measure the target momentum that occurred upon impact.

The target plate was securely attached to the front of the pendulum and it was free to move on a five-wire system which was suspended downrange of the light-gas gun. An overview of the results obtained by Denardo and Nysmith are presented in Table 4.2.

In order to replicate the experiments from Denardo and Nysmith [88] as closely as possible, the projectiles and target plates were modelled as Al 2024-T4. Al 2017-T4 is not available in Autodyn and so it was decided to use the closest substitute possible which was AL 2024-T4 as both are of the Al 20XX series and both have a T4 temper.

Considering that the focus of this study is the $\sim 1\ mm$ projectile range, simulations were only run using the 1.5875 mm diameter projectiles. Target thickness was set to 50.8 mm to replicate the experiments. Some initial simulations were carried out in order to determine how the variation of target diameter affected the accuracy of the simulation. The motivation for this was due to the fact that an increased target size required more SPH particles to fill and hence increased computation time substantially. Even when 2D axial symmetry was used, the resulting target size was 127 x 25.4 mm and took over 7 days to compute with an SPH particle diameter of 0.05 mm. A faster method of replicating the experimental results was needed while also maintaining the parameters used. It was vitally important that the thickness of the target was not altered, as doing so might affect the region of the material which behaves plastically and may not allow HVI-induced shock waves to convert to elastic waves [82].

In order to overcome this, an empirically derived relationship used by Murr et al. [89] was implemented which defines the ratio of crater diameter to projectile diameter. Through Equation 4.1, the crater diameter was estimated for each impact scenario and along with a factor of safety (FOS) of 5 mm, a scaled down target diameter was used without fear of losing simulation accuracy.

$$\frac{D_c}{d_p} = 1.1 \left(\frac{\rho_p}{\rho_t} \right)^{1/3} \left(\frac{\rho_t}{\sigma_t} \right)^{1/3} \left(\frac{v_t}{v_t} \right)^{1/3} (\mu_0)^{2/3} \left(1 + \frac{\rho_p}{\rho_t} \right)^{2/3} \tag{4.1}$$

D_c is the crater diameter, d_p is the projectile diameter, ρ_p and ρ_t are the projectile and target densities, respectively. μ_0 is the projectile velocity at impact. v_t and v_p are the target and projectile bulk sound velocities, respectively. σ_t is the target static yield strength.

Comparing the results from this approach to the full scale replication models yielded identical values meaning that the simulation time could be drastically improved without influencing the MEF results. This target diameter scaling technique was adopted throughout the rest of this section. Table 4.1 presents the target dimensions that were used for each study.

Test Number	Target Material	D_c/d_p	D_c	FOS (mm)	Target Diameter (mm)	Target Thickness (mm)
1	Al 2024-T4	8.35	14	5	19	50.8
2	Al 2024-T4	10.07	16	5	21	50.8
3	Al 2024-T4	12.12	20	5	25	50.8
4	Al 2024-T4	13.09	21	5	26	50.8

Table 4.1: Overview of scaled target dimensions for replicating Denardo and Nysmith study.

In addition to this, a particle density refinement study was also conducted in order to find the optimum particle packing size which conformed well with the experimental results while also yielding feasible simulation times. During this parametric study it was found that a size of 0.08 mm accurately captured the propagation of the shock waves, resulting in a good replication of experimental data while also not taking longer than 24 hours per simulation. Boundary conditions of 0 m/s were set around the target perimeter in order to recreate the same conditions that Denardo and Nysmith implemented during their observations.

The strength of Al 2024-T4 was set to 0.427 GPa which was reported by Walker et al. [31] as the actual tensile fracture stress and a hydrostatic pressure failure model was implemented. Simulation results for the 3569.21, 4724.40, 6239.26 and 6998.21 m/s impact velocity cases are illustrated in Figure 4.1. Clearly no perforation occurs implying that the MEF values are expected to be above 1.

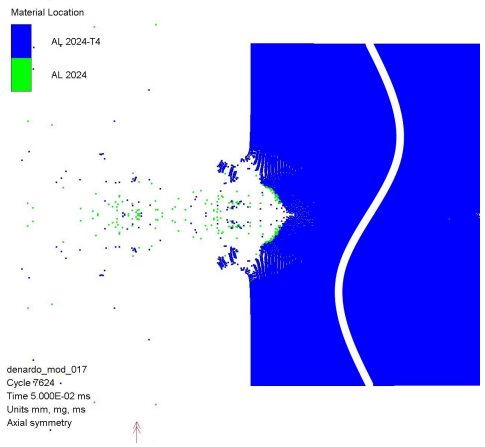

(a) Projectile velocity = 3569.31 m/s

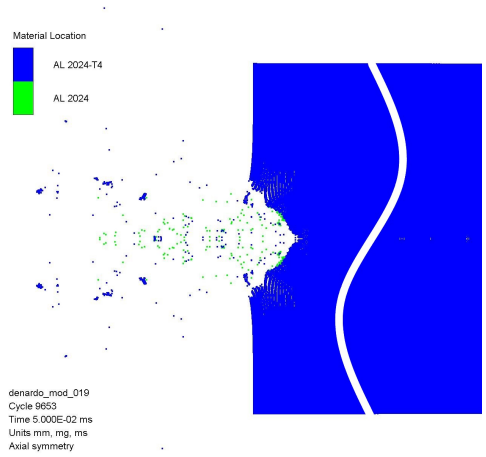

(b) Projectile velocity = 4724.40 m/s

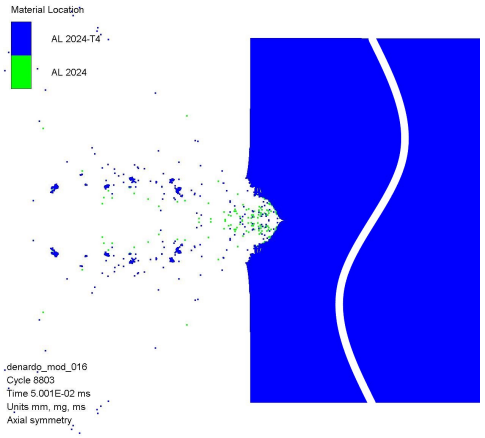

(c) Projectile velocity = 6239.256 m/s

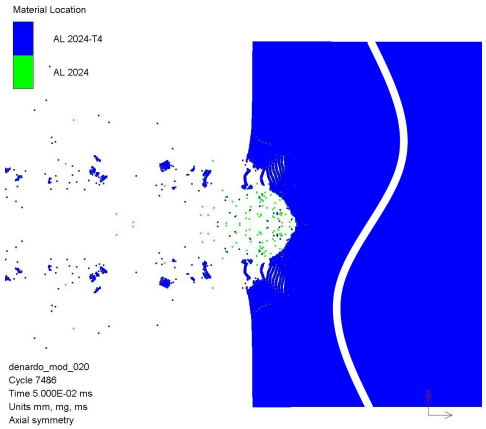

(d) Projectile velocity = 6998.21 m/s

Figure 4.1: Simulated impacts replicating Denardo and Nysmith study at approximately t = 0.05 m/s for various impact velocities.

The results obtained from these simulation are presented in Table 4.1 which compare extremely well with experimental values recorded by Denardo and Nysmith. Throughout the range of tests replicated, the percentage error in obtained MEF values is below 4%.

Test Number	Projectile Material	Projectile Diameter (mm)	Projectile Velocity (m/s)	Denardo MEF	Replication MEF	% Error
1	Al 2024-T4	1.5875	3569.21	1.09	1.13	3.67%
2	Al 2024-T4	1.5875	4724.40	1.21	1.22	0.83%
3	Al 2024-T4	1.5875	6239.26	1.31	1.33	0.76%
4	Al 2024-T4	1.5875	6998.21	1.36	1.34	1.47%

Table 4.2: Results of Denardo and Nysmith replication study.

Figure 4.2 shows a comparison of the MEF data obtained at different projectile velocities for both the experimental data and replicated simulations. There is good agreement overall and a clear increase in the MEF as projectile velocity increases. This can be attributed to the fact that at higher impact velocities, more ejecta fragments will be excavated and expelled at higher velocities.

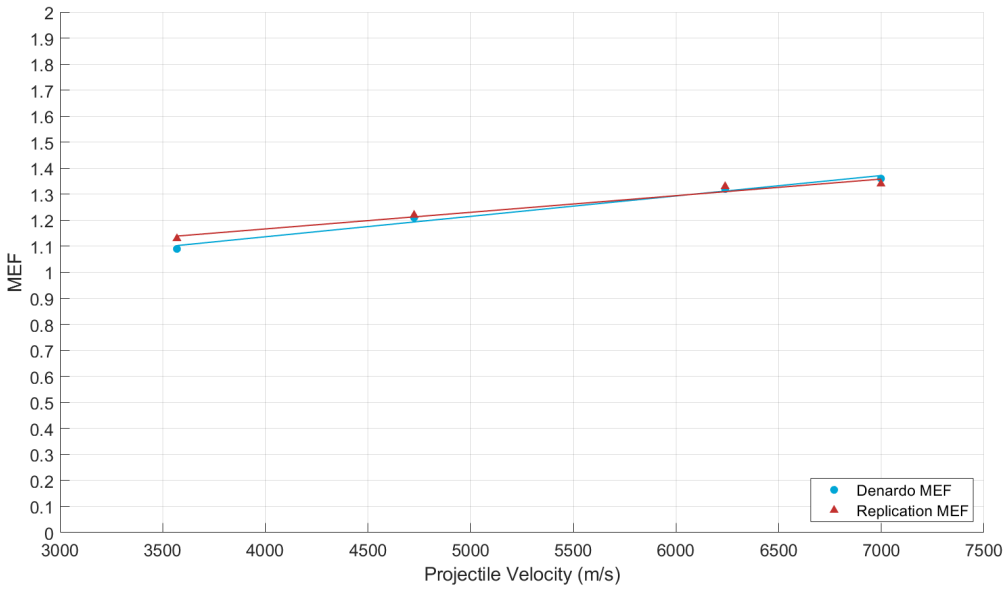

Figure 4.2: Results of Projectile Velocity vs. Momentum Enhancement Factor (MEF) comparing data obtained from studies by Denardo and Nysmith and through numerical simulation.

Overall, it has been shown that Autodyn can successfully model the momentum transfer that occurs during a hypervelocity impact. The Al 2024-T4 material model available in the Autodyn material library, modified with a hydrostatic pressure failure model, shows excellent agreement with experimental results from Denardo and Nysmith. Therefore a p_{min} value of 0.427 GPa will be used throughout the course of this thesis work when modelling Al 2024-T4.

4.2. Glass Models

Unfortunately no MEF data for glass could be found in literature. Since no experiments could be run, a different approach had to be used. It was decided that the closest alternative to measuring momentum transfer was to replicate the size of the craters formed following a HVI. The assumption being that if the size of the crater could be reproduced, then the MEF would be in a similar range due to the amount of ejecta mass that was expelled.

The experimental data used for glass model validation was taken from studies conducted by Taylor et al. [90]–[92] where the crater depth was measured as indicated in Figure 4.3. In these run of studies, spherical projectiles of varying materials including Al 2017, nylon, stainless steel and cellulose acetate with a range of diameters and velocities were launched into soda-lime glass targets of 50.8 *mm* diameter and 25.4 *mm* thickness. Experiments from Taylor et al. [92] using the Al 2017 projectile were simulated using diameters in the range of 0.8-2.0 *mm*. Due to the size of the 50.8 x 25.4 *mm* target, the amount of SPH particles required to fill this space caused the simulation to run for over 48 hours. A larger SPH packing size could be used, but this sacrificed the accuracy of the simulation. Some initial sizing studies were conducted in order to see how small the target could be set while still achieving the same MEF data. It was found that the diameter of the target could be reduced significantly while still producing the same MEF. The thickness of the target was kept the same in order to accurately capture any spallation that may occur. The results of this initial testing showed that a reduction of the target diameter from 50.8 *mm* to 15 *mm* conserved all MEF results and for this replication study, the final target dimensions were set to a diameter of 15 *mm* and a thickness of 25.4 *mm*. This substantially reduced simulation time from ∼48 hours to ∼12 hours.

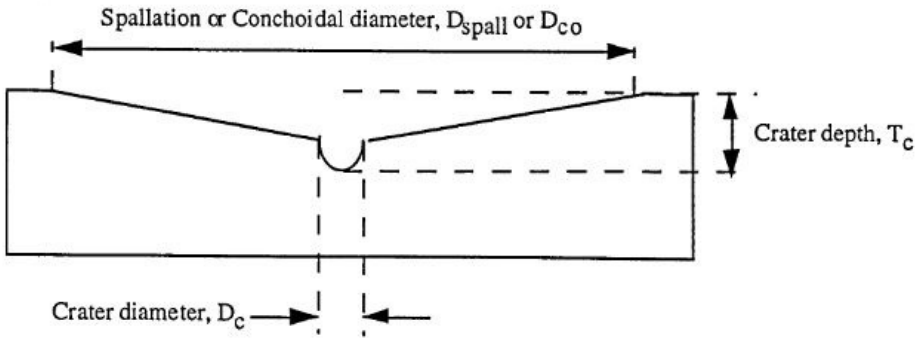

Figure 4.3: Soda-lime glass morphology following a HVI [90].

The data presented by Taylor et al. was not tabulated so Plot Digitizer was used in order to extract the data points on the graph shown in Figure 4.4. This plots projectile diameter vs. crater depth for a variety of materials both experimentally and using a Mohr-Coulomb strength model in Autodyn. Only the experimental results are of interest and so the latter can be ignored. Its observed that the crater depth increases linearly with increasing projectile

diameter, as expected.

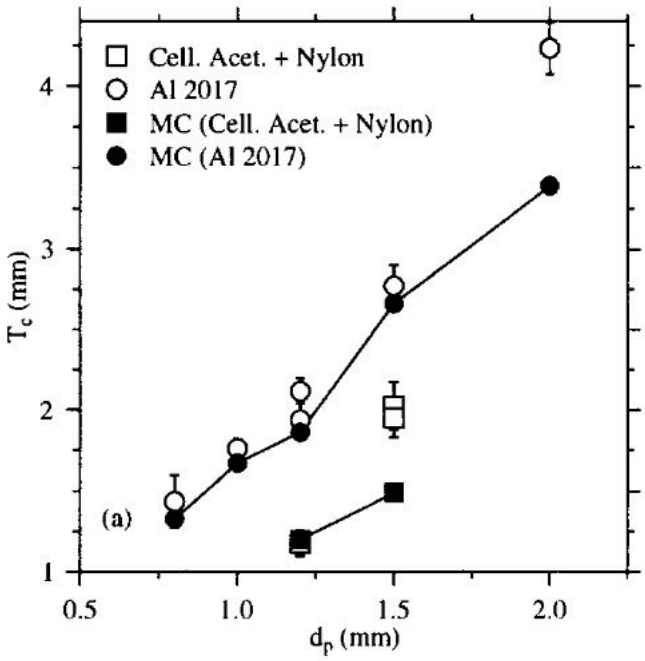

Figure 4.4: Crater depth T_c plotted against projectile diameter d_p for Nylon, cellulose acetate and Al 2017 [92].

4.2.1. Strength Variation Study

In order to accurately replicate the experimental results, its imperative that the material model used in the simulations enables the material to behave in the same way that it would in real life. At the forefront of this is determining specific parameters, most notably the strength of the material. When Taylor [90] ran Autodyn simulations to compare her experimentally derived results, she used a hydro tensile limit of 0.15 GPa. Taylor reports that the simulations typically over-predicted the crater diameter by up to 50 % and to a lesser extent the crater depth.

In a study conducted by Holmquist and Johnson [93] to develop a computational material model for glass, they reported a hydrostatic tensile pressure of 0.1 GPa. A different study by Wei et al. [94] report a value 0.35 GPa. Clearly there are some differences in values between authors and some discrepancies between experimental and numerical results obtained by Taylor. A parametric simulation study was conducted in order to determine whether which value for hydrostatic pressure could best replicate the experimental results presented by Taylor. All simulations used Al 2017 as the projectile material. The material model for Al 2017 was taken from [95] which had been previously validated.

The three values for the hydrostatic tensile limit that were tested were 0.1, 0.15 and 0.35 GPa, interestingly there are two glass models available in the Autodyn material library, only differing by these values. One has a value of 0.15 GPa and the other 0.35 GPa

Figure 4.5 depicts images from the 5050 m/s impact velocity simulation which used the a p_{min} value of 0.35 GPa. Figure 4.5a shows a full view of the target while Figure 4.5b shows a close up view and how the value of T_c was determined.

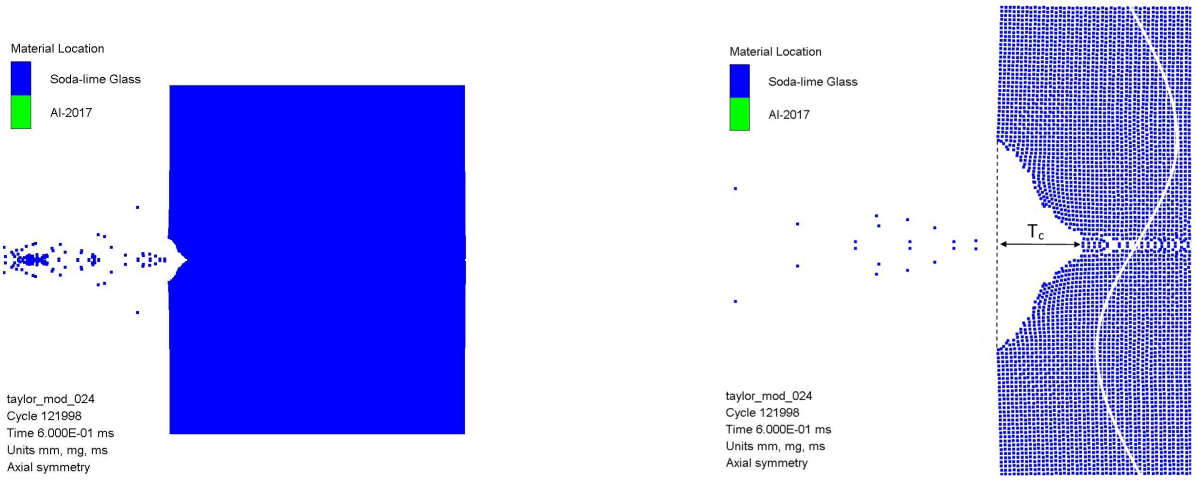

(a) Full view

(b) Enlarged view to show how T_c is calculated

Figure 4.5: Soda-lime glass target at t = 0.6 ms following impact with 1 mm Al 2017 sphere projectile at 5050 m/s with P_{min} = 0.35 GPa .

Within Autodyn, there is an examine feature which allows the user to select individual SPH particles and access the data pertaining to it such as coordinates, mass and velocity. This feature was used to obtain the x-coordinate of the particles at the very bottom of the crater. Since the dotted line represents the y-axis, the x-coordinate of these particles represents the distance and hence depth of crater, T_c. This was done for a range of simulations with strength values of 0.10, 0.15 and 0.35 GPa and the results are presented in Table 4.3.

Projectile Diameter (mm)	Projectile Velocity (m/s)	T_c (mm) 0.35 GPa	T_c (mm) 0.15 GPa	T_c (mm) 0.1 GPa	T_c (mm) Taylor
0.8	5000	1.24	2.12	1.29	1.43
1.0	5050	1.54	1.61	1.96	1.76
1.2	5070	2.4	1.93	2.07	2.11
1.5	5180	2.73	3.32	3.69	2.76
2.0	4440	4.82	5.10	5.15	4.24

Table 4.3: Crater depth (T_c) data achieved for various strengths compared with experimental results from Taylor [92].

Figure 4.6 plots projectile diameter versus crater depth and shows a comparison between the experimental and simulated data for various strengths. Using a line of best fit approach, the 0.35 GPa value seems to be the closest in terms of replicating experimental results.

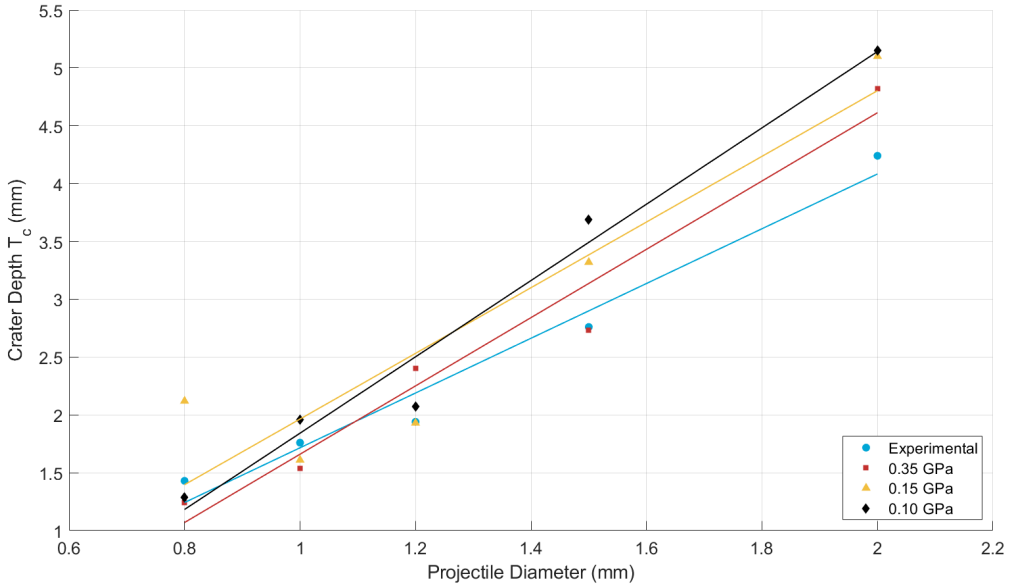

Figure 4.6: Projectile Diameter D_p vs. Crater Depth T_c for 0.90, 0.95, 1.00 GPa and experimental results from Taylor [92].

To analyse this further, a squared error method was used. The results are outlined in Table 4.4 which show the values for 0.35 GPa being the closest to the experimental values obtained by Taylor.

Strength (GPa)	Squared Error
0.10	1.77
0.15	1.55
0.35	0.63

Table 4.4: Squared Error for strengths 0.10, 0.15 and 0.35 GPa.

Due to the lowest squared error value, 0.35 GPa was set as the hydrostatic tensile limit for glass components considered throughout this project. Table 4.5 provides a comparison between the crater depth values obtained in Autodyn and those obtained by Taylor. The values from the simulations show good agreement and are within 14% of the experimental values. This is a random variation up and down and is not a consistent bias of ∼14%. The MEF values associated with the simulations are also recorded.

Projectile Diameter (mm)	Projectile Velocity (m/s)	T_c (mm) using 0.35 GPa	Taylor (mm)	% Error	MEF
0.8	5000	1.24	1.43	-13.29	1.18
1.0	5050	1.54	1.76	-12.50	1.18
1.2	5070	2.4	2.11	13.74	1.21
1.5	5180	2.73	2.76	-1.10	1.18
2.0	4440	4.82	4.24	13.68	1.23

Table 4.5: Comparison of crater depth (T_c) data achieved using 0.35 GPa hydrostatic tensile limit and experimental results from Taylor [92]

5

Solar Array Model Formulation

The aim of this chapter is to formulate a model for a typical satellite solar array that can be implemented into Autodyn. Two types of solar arrays are considered, namely the EURECA and HST solar arrays. Due to the complex, multi-layered structure of these respective arrays, a simplified model is proposed which drastically increases simulation efficiency.

5.1. Solar Array Model Formulation

This section outlines the differences between the two most commonly studied solar panel configurations. Both material and structural differences are considered and a simplified model of the HST solar array is presented.

5.1.1. EURECA vs. HST Solar Panels

Many varieties of solar panel configurations exist. Two of the most studied layups in terms of HVIs have been the European Retrievable Carrier (EURECA) and the Hubble Space Telescope (HST) solar panels. EURECA was retrieved by Space Shuttle Endeavour and returned from space in July 1993. Similarly, during a repair, one of the HST solar arrays was retrieved in December 1993 and then again in March 2002. This enabled a whole host of post-flight measurements of debris impact features to be recorded and analysed. The data obtained from these solar arrays provided a great deal of unprecedented documentation ,which among other things, allowed researchers to validate and update debris flux models as well as calibrate any HVI testing.

Of course, the composition of these solar arrays are not the same and considering that impact morphology is highly dependent on target properties, different behaviour was observed. The most obvious difference between the two is the CFRP Aluminium Honeycomb panels on the rear side of the EURECA solar arrays. Apart from this they essentially have the same composition - coverglass, a solar cell, RTV and adhesive as can be seen in Figure 5.1.

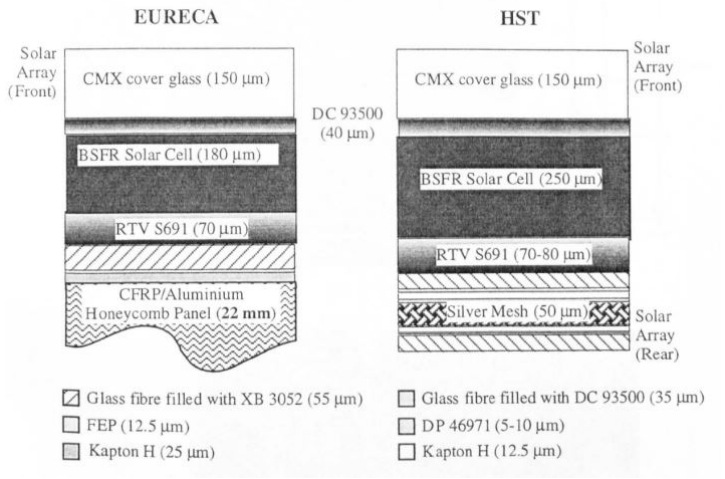

Figure 5.1: Solar panel cross-sectional schematic for EURECA and HST [90].

CFRP/Al HC panels have been widely adopted in aerospace structures due to their good strength to weight ratio and provide extremely good support for solar panels. The Fraunhofer Institute for High-Speed Dynamics in Germany have conducted a multitude of tests surrounding HVI testing into CFRP/Al HC panels. The work done by Ryan et al. [96], Wicklein et al. [73] and Schäfer et al. [97] involved investigating the damage induced by a range of different projectile conditions into commercial off-the-shelf (COTS) CFRP/Al HC panels presented in Figure 5.2.

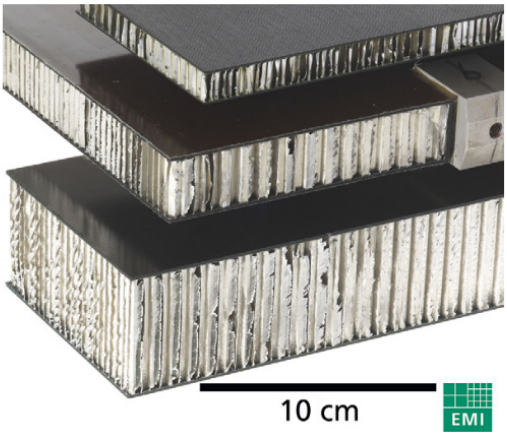

Figure 5.2: Three different Radarsat-2 CFRP AL HC panels used by Ryan et al. [96].

Ryan et al. measured various parameters such as front and rear clear hole diameter, diameter of surface spall area and also whether perforation occurred or not. It was originally planned that the data obtained from this work would be used for validation in the same way that the work from Taylor et al. [92] was used. The various measured diameters could be compared to the ones obtained in Autodyn and the MEF values could be estimated. As part of their investigation, Wicklein et al. even developed an orthotropic material model for CFRP allowing for a nice implementation into Autodyn. In his PhD thesis, Ryan [98] also presents material models for Al 5056 which is a common aluminium type used for the honeycomb. Unfortunately however, some issues arose particularly around computation time and it was decided to not go any further with the CFRP/Al HC panels and focus on the HST solar arrays for the remainder of this study. This is discussed further in Section 10.2.

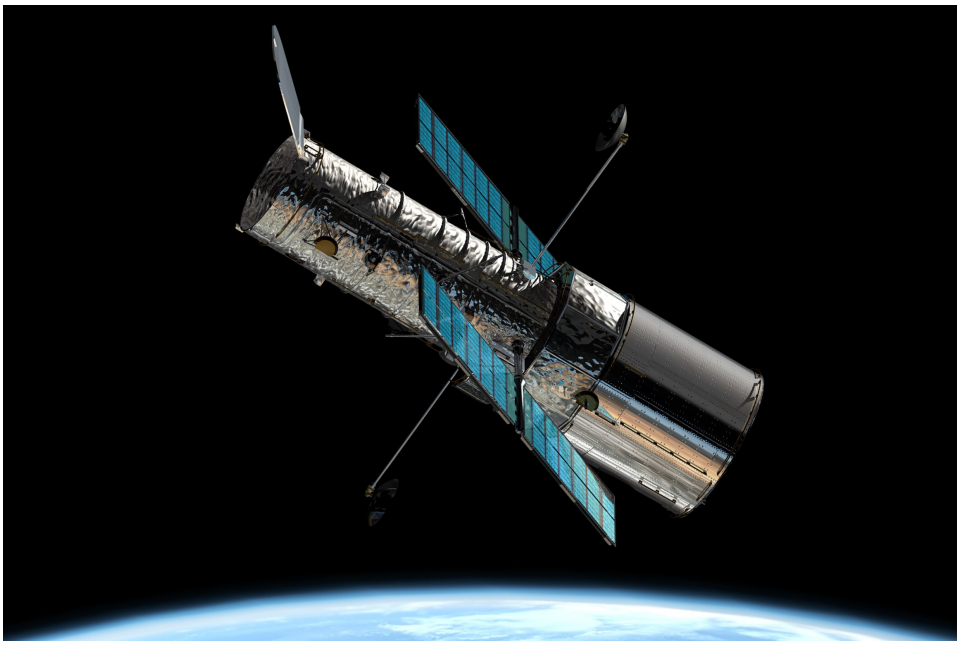

Figure 5.3: Hubble Space Telescope [99].

5.1.2. Structure of HST Solar Panels

The solar cells that were analysed for this study were recovered by the 3B servicing mission aboard the Space Shuttle Columbia in March 2002. Each HST cell measures 40.2 x 20.8 x 0.7mm. The visible faces in Figure 5.4 show the composite substrate of the solar generator and the CMX protective glass. As shown in Figure 5.5, a HST solar cell has a complex multilayer structure. It consists of a borosilicate protective glass (CMX cover glass) bonded to a semiconductor made of silicon by a layer of adhesive. This assembly which constitutes the solar cell is glued to the composite substrate of the panel with an RTV glue. Old Hubble substrates are made up of different layers including fiberglass, Kapton film, silver grid, and layers of glue. This flexible substrate was replaced by a rigid substrate in March 2002 [81]. A quick analysis of the overall panel underlines that the structure is made of some very fragile materials like the glass and silicon solar cell. However, it should be noted that the composite substrate and the adhesive layers guarantee the strength of the structure and give it satisfactory resistance to hypervelocity impacts.

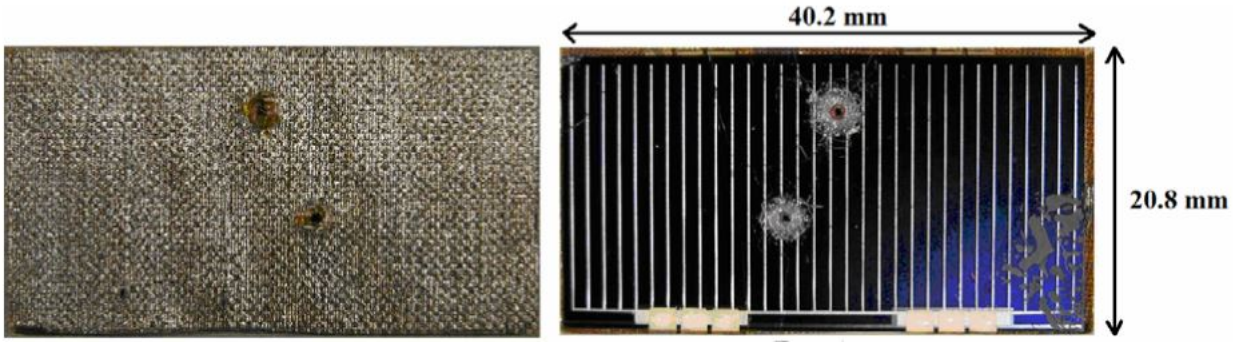

Figure 5.4: Photos of the rear (left) and front (right) faces of a retrieved Hubble solar cell. On the left, two points of entry can be seen into the composite substrate and, on the right, the damage caused by the phenomenon of chipping and spallation on layers of silicon and glass [81].

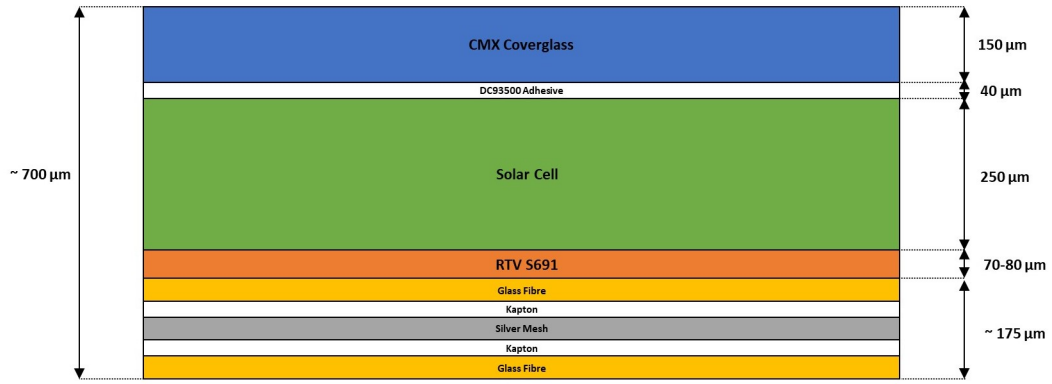

Figure 5.5: Internal structure of a HST solar panel.

5.1.3. Simplified HST Solar Panel Model

Due to the variety of materials used in the HST solar panels, it is extremely difficult to consider a complete numerical model. The substrate alone is composed of fiberglass, Kapton film, a silver mesh, and layers of adhesive as can be seen in Figure 5.5. Due to this complexity, a similar approach is taken to Michel [81] who assimilated the substrates behaviour to a ductile material.

Additionally, the solar cell also poses some issues in terms of choosing an appropriate material model. The solar cell is composed of silicon and unfortunately there is no model available in Autodyn which means alternative options must be explored. Michel also came across the same issues, and to overcome them, assumed that silicon behaves similarly to fused silica. Fused silica is more widely studied and he combines its experimentally derived parameters with the main characteristic data for silicon like density, shear modulus and Hugoniot Elastic Limit. This material model is presented in Table A.3.

An earlier study by Taylor [90] compared the behaviour and impact morphologies of a HST solar cell to soda-lime glass. During her work, Taylor confirmed that the soda-lime targets show a very similar hypervelocity impact response to solar cells in terms of pit profile (D_{co}/D_{pit}) and is highlighted in Figure 5.6.

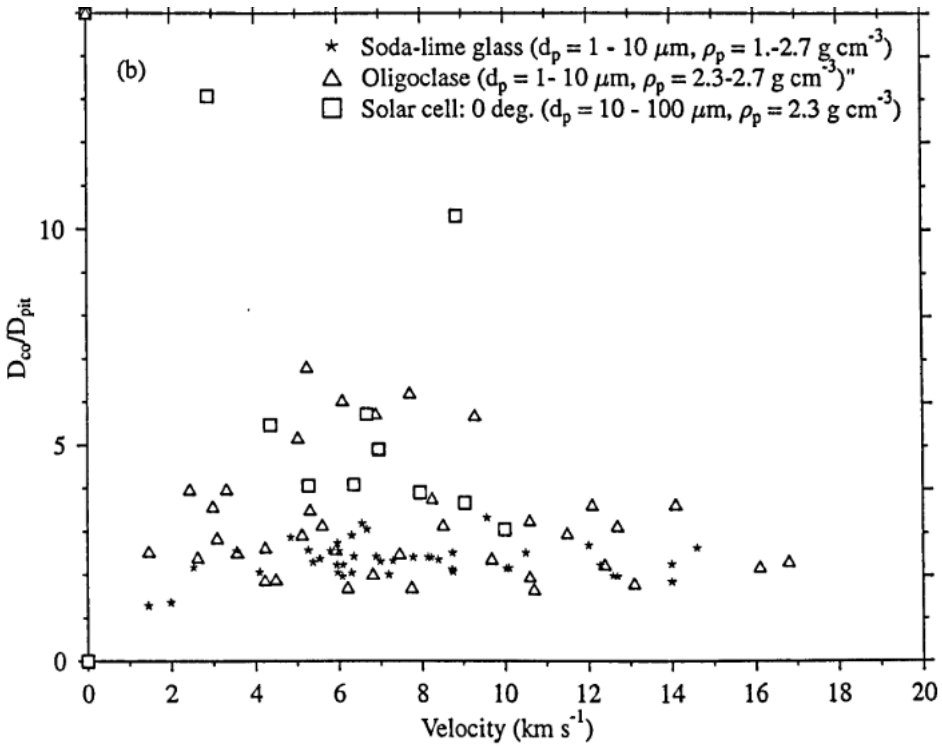

Figure 5.6: Projectile Velocity vs. Chonchoidal Diameter/Pit Diameter for solar cell, soda-lime glass and oligoclase targets [90].

Seeing as soda-lime glass has already been validated in this study, and its behaviour can be assimilated to that of a silicon solar cell, it will be used to model the silicon layer. The proposed silicon model presented by Michel cannot be validated due to the absence of published experimental data. However, it will still be modelled and used as a comparison. Simplifying the solar panel in this way allows for the optimisation of Autodyn in terms of simulation time while also providing a simplified understanding of the damage mechanisms linked to the propagation of a shock wave in a fragile multilayered structure. The solar panel is therefore broken down into 3 main constitutive parts where the thickness of each layer is approximated in the same manner as Michel:

1. **Coverglass:** The thickness of the protective glass layer was set to 0.2 mm. The material model for Float glass was used to replicate the behaviour of the solar panel coverglass.
2. **Solar Cell:** The thickness of the silicon layer was set to 0.3 mm. Two sets of tests were run in order to compare the behaviour of the proposed Silicon model.
   (a) The first set of simulations considers this layer to be another layer of glass. This has already been validated in Section 4.2.1 and behaves similarly to silicon as confirmed by Taylor [90]. This is termed the glass-glass-aluminium target configuration.
   (b) The second considers that the material model for Silicon is similar to that of Fused Silica and the data is taken from Michel [81]. This is called the glass-silicon-aluminium target configuration.
3. **Substrate:** The thickness of the substrate was set to 0.2 mm. Its behaviour is considered to be ductile in order to reproduce the good resistance of the structure under high impact speeds. The material model for Al2024-T4 which has been previously validated was implemented.

An overview of the simplified structure is illustrated in Figure 5.7.

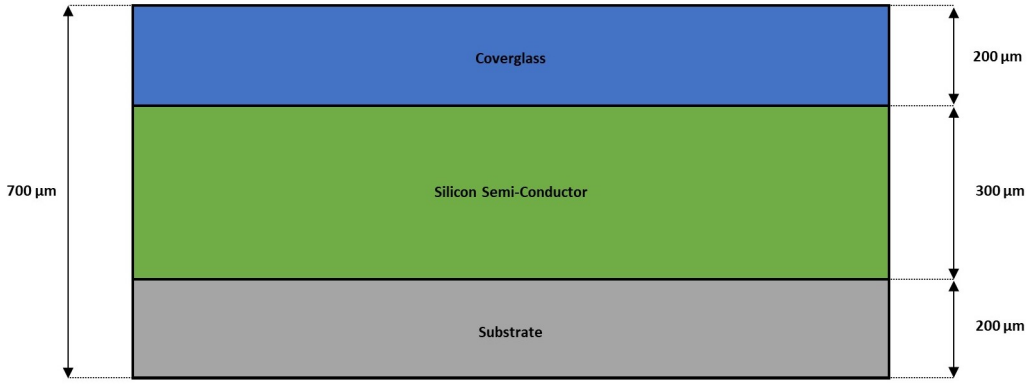

Figure 5.7: Simplified HST solar panel internal structure used in Autodyn.

It was important that the impact morphology of the simplified model showed similarities to real-life HST solar arrays which were exposed to hypervelocity impacts. Although the size and velocity of the projectile which impacted the HST array in Figure 5.9 are unknown, it is useful in determining the typical damage profile. Comparing this to simulation results illustrated in Figure 5.8a (2D) and Figure 5.8b (3D), its clear that the step structure of the glass and silicon layers is present and look quite similar. There are however some slight differences in the substrate layer. The multiple layers that make up the substrate are quite distinct in Figure 5.9 and show the delamination quite well. In comparison, due to the single layer used to model the entire structure, Figures 5.8a and 5.8b fail to replicate this delamination behaviour, which was of course expected. On a positive note, the profile of penetration on the rear face of the models bear a close resemblance to the image of the real-life tests. The lipped shape is quite prominent and is a feature of ductile failure and is a good indication that the simplified model performs well in replicating experimental behaviour. Comparing the impact morphology in this way highlights the limitation of the simplified model in its ability to show this delamination behaviour. Nevertheless the scope of this study is not to analyse every detail of damage in the structure but rather the essence of MEF which is more to do with ejecta mass and velocity.

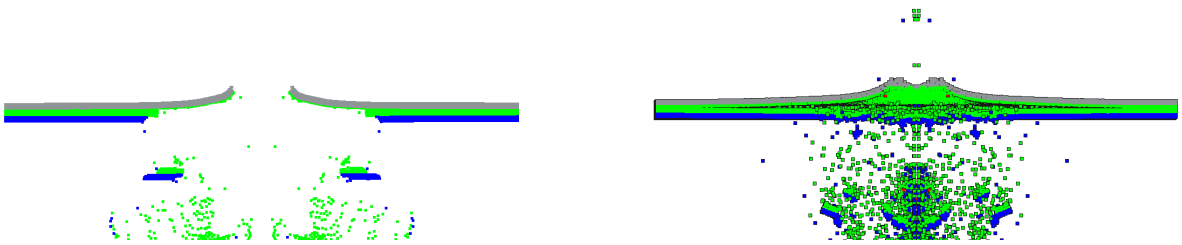

(a) 2D model **(b)** 3D model

Figure 5.8: 2D and 3D models of a simplified HST solar cell following a HVI.

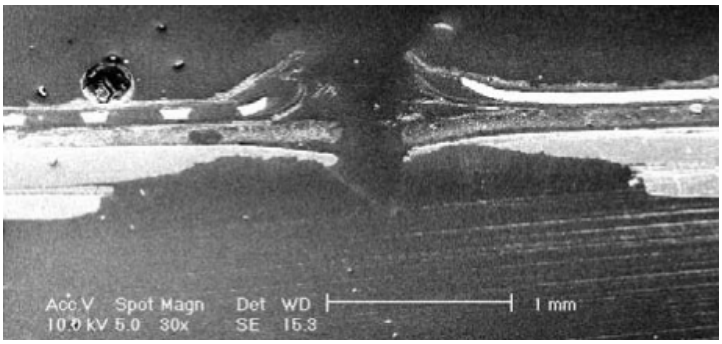

Figure 5.9: SEM (Scanning Electron Microscope) images of a HST solar cell following a HVI showing significant delamination [81].

6

Projectile Size Study

The objective of this chapter is to obtain MEF values for a range of different projectile sizes using two different target configurations. The first is the glass-glass-aluminium target where all materials have been validated. The second is the glass-silicon-aluminium target which remains a proposed model as no data could be found to validate the behaviour of silicon under hypervelocity impact. Although this second configuration is only a proposed model, the results of both approaches are presented and compared in this chapter.

6.1. Glass-Glass-Aluminium Configuration

Before getting into any of the simulations, its important to consider how the next few chapters are related to each other. This is illustrated by Figure 6.1.

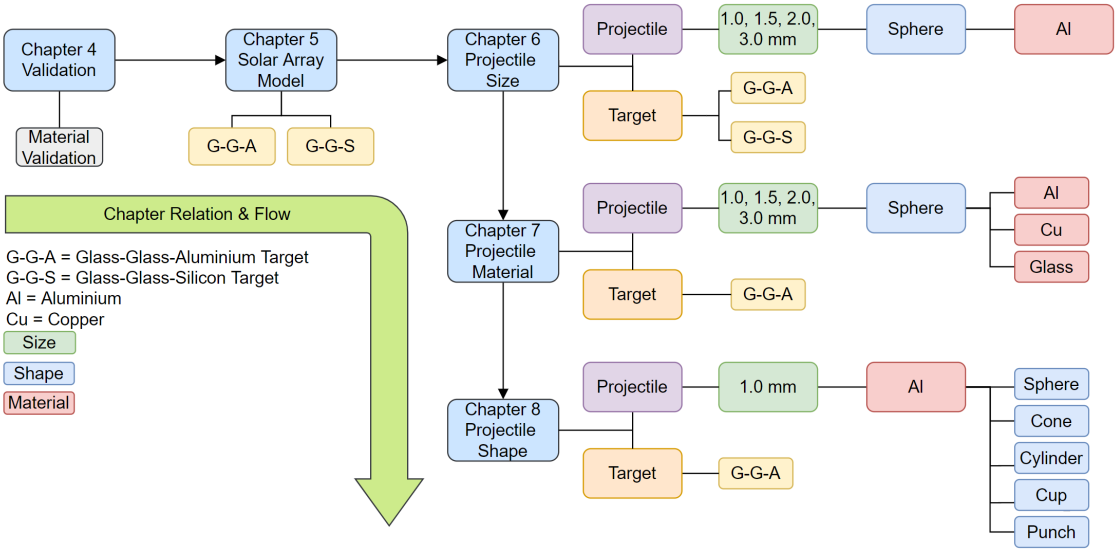

Figure 6.1: Flowchart of methodology from Chapters 4-8.

Here we see the logical flow starting from initial validation and solar array model formulation, right the way through to Chapters 6, 7 & 8 which explore the effects of projectile size, material and shape respectively. This highlights the various parameters which are being investigated in each chapter and how they relate to each other at a high level.

6.1.1. Model Setup

Now that the simulation methodology has been defined, we can move on to the first study involving the projectile size. During this study, both the coverglass and silicon layers were modelled as soda-lime glass and the substrate layer was modelled as Al 2024-T4. All of these materials have been previously validated in Chapter 4. Four different projectile diameters were selected, namely 1.0, 1.5, 2.0 and 3.0 mm. Each projectile size was simulated at 1000, 2000, 3000, 7000, 10000 and 14000 m/s. An initial SPH particle density refinement study was conducted in order to find the smallest particle packing size which yielded feasible simulation times while also producing accurate results. During this parametric study, three particle sizes were tested, namely 0.1, 0.05 and 0.02 mm. It was found that 0.1 mm resulted in too little SPH particles in order for the simulation to stabilise. The 0.05 mm and 0.02 mm packing sizes yielded identical MEF results, with the 0.05 mm simulation having a run time of 48 hours compared to 56 with the 0.02 mm. Due to the lower simulation time and accurate results, 0.05 mm was set as the SPH packing size for the HST simplified solar panel models considered throughout this project. In order to constrain the movement of the target and clamp it in place, a boundary condition was imposed on the top row of SPH particles which prevented movement in the x- and y-direction as outlined in Section 3.4.

6.1.2. Ballistic Limit

Before assessing the various impact scenarios, it is important to understand the fundamental mechanics of the ballistic limit. The ballistic limit is the critical size of projectile that causes perforation or spallation of the target structure. It is often defined by a ballistic limit equation (BLE) which is used to characterise the performance of a shield under hypervelocity impact and is a function of projectile parameters (density, shape, velocity), impact angle and wall thicknesses. They are graphically represented by a ballistic limit curve (BLC) which highlight the threshold for penetration by plotting impact velocity against projectile size. Figure 6.2 shows the BLC for single-wall and double-wall target configurations and highlights some of the important phenomenology that occurs in various impact velocity regimes. The regions below the lines represent where no perforation occurs. These are extremely useful graphs whereby for a double-wall system it can be seen that a for a given projectile size, perforation may occur in the ballistic range, but not at higher velocity regimes. This is due to the fact that at lower velocities, projectiles tend not to fragment to the extent that they do at higher velocities. For a double-wall target, this means that fragmentation of the projectile leads to less impulse density on the rear wall and reduces the risk of penetration.

On the other hand, the single-wall BLC is more straight forward and displays inverse proportionality. In the ballistic region, the projectile is deformed following its impact but remains more or less intact. For aluminium projectiles striking aluminum targets, this is typically below impact velocities of 3000 m/s [100]. When the ballistic range transitions into the shatter range, the projectile becomes increasingly fragmented and as it does, disperses ejecta material across a larger area. This trend carries through to the melt/vaporisation region. The transition velocity between the shatter range and the melt/vaporisation range is approximately 7000 m/s for normal aluminum-on-aluminum impacts. This is where the projectile is substantially melted.

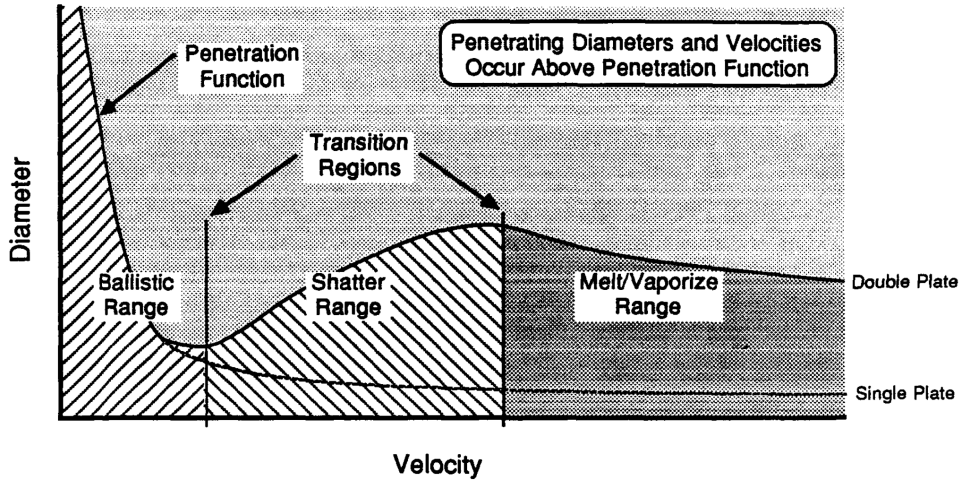

Figure 6.2: Generic Single-Wall and Double-Wall Ballistic Limit Curves [101].

6.1.3. Qualitative Comparison

In order to get a better sense of the behaviour and impact morphologies of these materials under hypervelocity impact, visualisations of the debris cloud and impact sites are presented below for each impact case. Presenting the simulations in this way will enable inferences to be drawn regarding the influence of increased velocity on the simplified solar panel target. The differing orbital mechanics of various regimes is the reason for testing all of these impact velocities. LEO impacts will mostly be in the range of 10000-14000 m/s, but the lower impact velocities are reasonable for say an inclined GEO orbit and are therefore worth including to understand how MEF changes.

Case 1: $V_p = 1000\ m/s$

Figure 6.3 presents the simulation results obtained for the $V_p = 1000\ m/s$ impact case. Closer inspection of the debris cloud in Figure 6.3a shows that both the downrange and back-scattered ejecta in the respective debris clouds have little dispersion in the y-direction, creating very narrow debris clouds. The bulk of the fragments are more spread out amongst the x-direction with less fragmentation of the impactor itself. The in-line characteristics of the debris cloud are consistent with a ballistic impact as opposed to hypervelocity one as highlighted in Figure 6.2. Figure 6.3b displays an enlarged view of the impact site where a degree of spallation can be seen. The first and second layers comprise of glass and their brittle behaviour is evident through the complete obliteration around the impact site. The third layer, made from aluminum, is observed to have undergone far more ductile deformation and absorbed more energy before it fractured completely, creating the burst profile that can be seen.

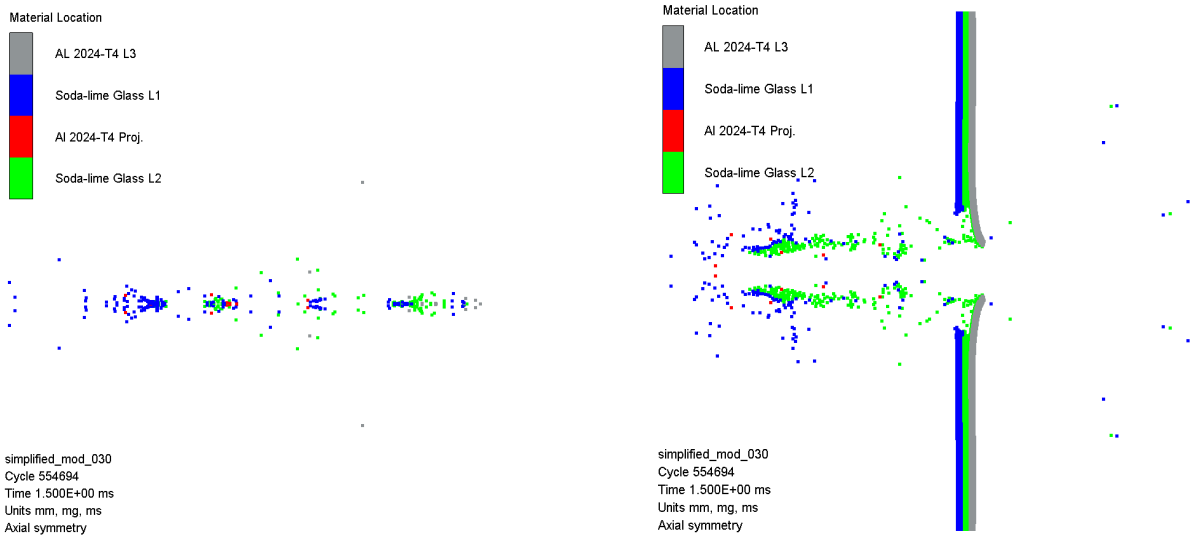

(a) Debris cloud produced by impact.

(b) Enlarged view focussing on impact site.

Figure 6.3: Simulated debris cloud and damage induced by using aluminium spheres of 1 mm diameter for $V_0 = 1000\ m/s$ at $t = 1.5\ ms$ after impact into a 0.7 mm glass-glass-aluminium thick target.

Case 2: $V_p = 2000\ m/s$

The overall profile of the debris cloud in the $V_p = 2000\ m/s$ impact case has transitioned from following a very narrow path either side of the target, to having a slightly larger angle of ejection as highlighted in Figure 6.4a. The impact looks like it is still within the ballistic range, although the projectile is becoming more and more fragmented which indicates that it is probably around the vicinity of the shatter region. Moving over to Figure 6.4b, it is observed that significantly more damage has occurred in the first and second glass layers. Two sizeable chips of glass have broken away from the front face and have resulted in a larger crater width as opposed to the $V_p = 1000\ m/s$ case. On a general note, the brittle nature of glass means that it has a lower tensile strength than aluminium and this is evident in the spalling behaviour we see here.

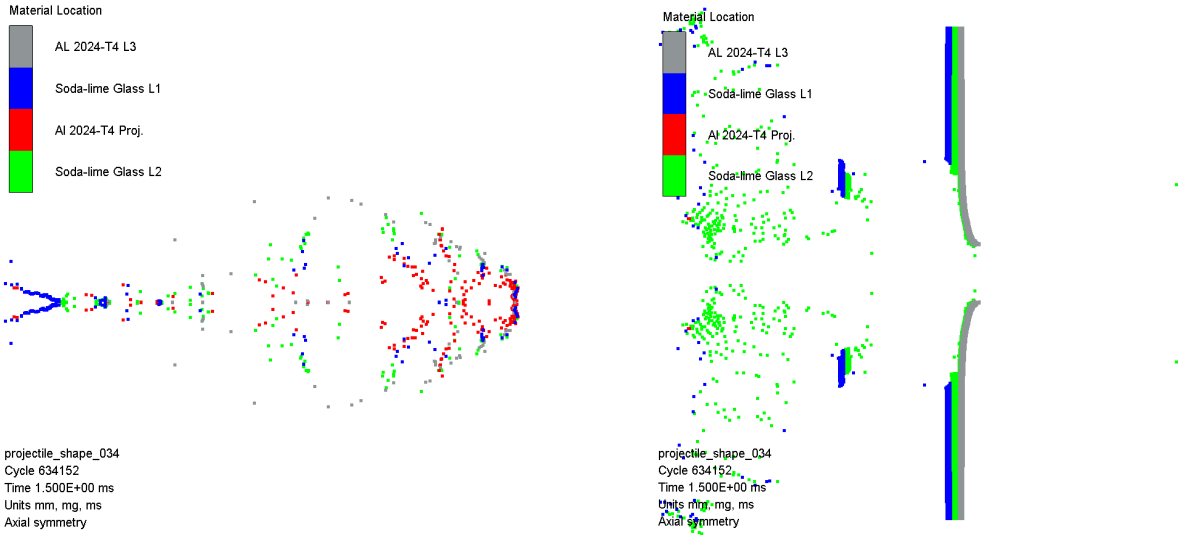

(a) Debris cloud produced by impact.

(b) Enlarged view focussing on impact site.

Figure 6.4: Simulated debris cloud and damage induced by using aluminium spheres of 1 mm diameter for $V_0 = 2000\ m/s$ at $t = 1.5\ ms$ after impact into a 0.7 mm glass-glass-aluminium thick target.

Case 3: $V_p = 3000\ m/s$

In comparison to the previous two impact velocities, Figure 6.5a illustrates how a much more distinct debris cloud is produced with a lot of the impactor material on the leading edge of the downrange cloud and indistinguishable from the other materials. It is very likely that the impact is now transitioning to the shatter regime and explains why the debris cloud is larger due to the projectile becoming much more fragmented. On closer inspection of the trailing edge of the debris cloud, it proves to be divided into more distinct particle layers and can be distinguished in the order that the layers were impacted. The outermost layer of particles is grey (aluminum layer 3), followed by green (glass layer 2), blue (glass layer 1) and finally red (aluminium projectile) as we work inwards. Interestingly, Figure 6.5b does not show as much chipping on the front face as opposed to the $V_p = 2000\ m/s$ impact case, but does however show a slightly larger puncture hole through the aluminum layer.

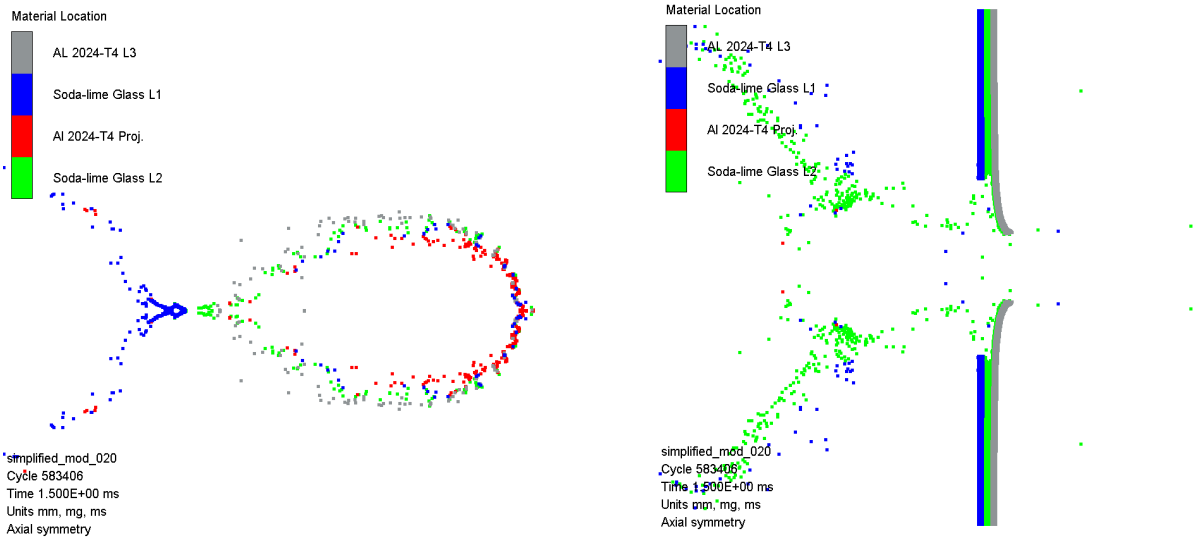

(a) Debris cloud produced by impact.

(b) Enlarged view focussing on impact site.

Figure 6.5: Simulated debris cloud and damage induced by using aluminium spheres of 1 mm diameter for $V_0 = 3000\ m/s$ at $t = 1.5\ ms$ after impact into a 0.7 mm glass-glass-aluminium thick target.

Case 4: $V_p = 7000\ m/s$

Looking at the trailing edge of the downrange debris cloud in Figure 6.6a it can be seen to follow the same trailing edge behaviour as Figure 6.5a, but with slightly more grouped together particles. It seems reasonable to assume that upon impact, the outer layers of the debris cloud or halo should consist of the target material that has been expelled outwards and that the inner cone should consist of the impactor debris. This is evident by looking at Figure 6.6a where there is a clear separation between the impactor debris and all other debris in the leading edge. Its also evident from Figure 6.6a that the quantity of glass left on the front face is smaller than the $V_p = 3000\ m/s$ impact case and that the diameter of the hole of penetration though the aluminium is larger again.

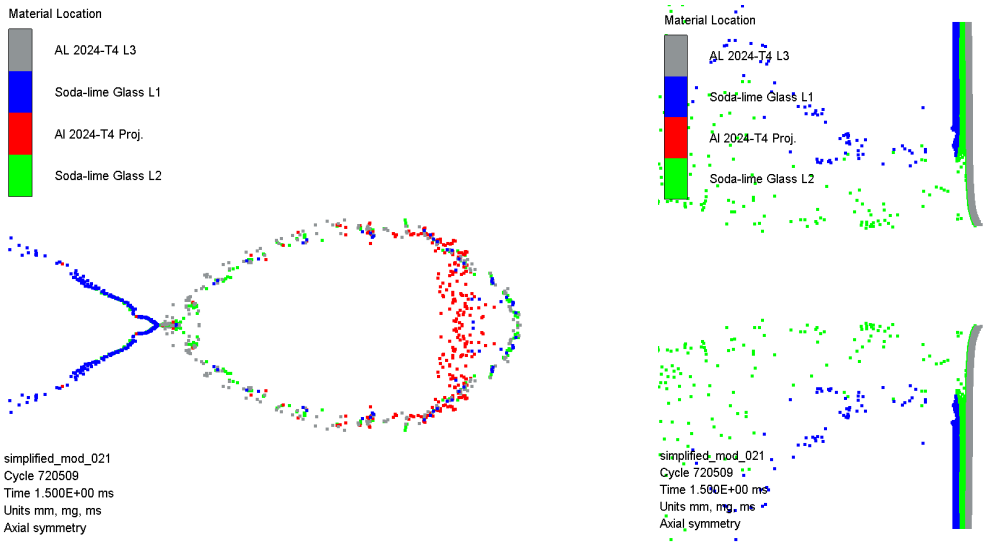

(a) Debris cloud produced by impact.

(b) Enlarged view focussing on impact site.

Figure 6.6: Simulated debris cloud and damage induced by using aluminium spheres of 1 mm diameter for $V_0 = 7000\ m/s$ at $t = 1.5\ ms$ after impact into a 0.7 mm glass-glass-aluminium thick target.

Case 5: $V_p = 10000\ m/s$

It is quite clear that up until now, the general trend is that as impact velocity increases, the angle of ejecta gets larger which in turn results in a larger debris cloud. Comparing Figure 6.7a to Figure 6.6a, it is clear to see that the impactor debris is also less grouped and has lagged even further behind the trailing edge of the downrange debris cloud.

It is also true that for an increase in velocity the quantity of glass material remaining in tact on the front face decreases as well as the larger diameter of penetration of the aluminium layer. The growth of the spallation zone is due to an increase in fracturing and subsequent ejection of glass material in the vicinity of where the projectile impacted the target. The greater the impact velocity, the higher the kinetic energy and the more stress is induced to the surrounding material by the expansion of the central pit. Figure 6.7b highlights this behaviour quite well when compared to previous lower projectile velocities.

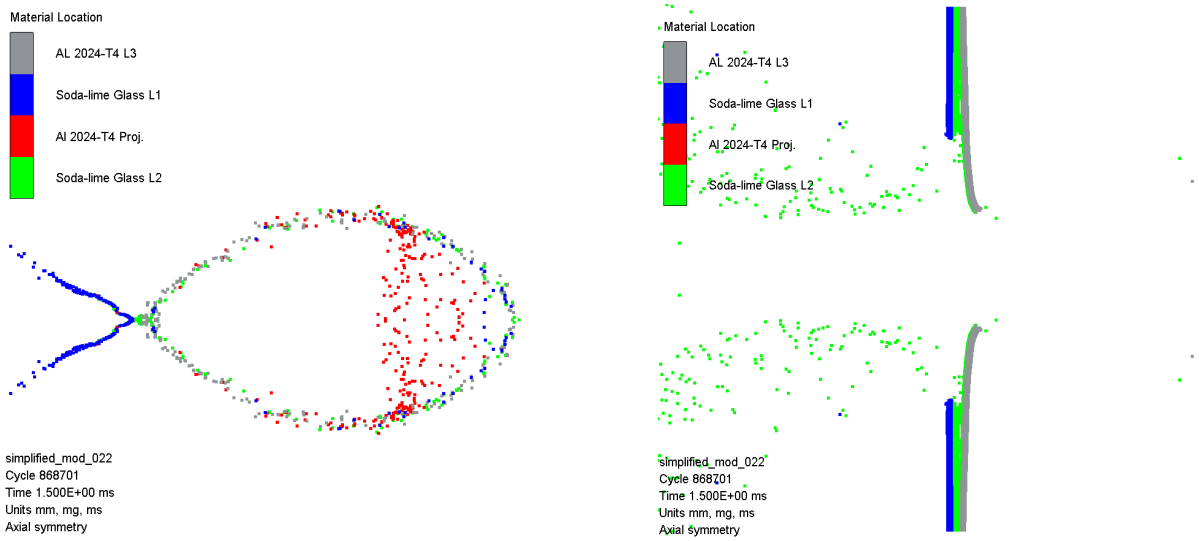

(a) Debris cloud produced by impact.

(b) Enlarged view focussing on impact site.

Figure 6.7: Simulated debris cloud and damage induced by using aluminium spheres of 1 mm diameter for $V_0 = 10000\ m/s$ at $t = 1.5\ ms$ after impact into a 0.7 mm glass-glass-aluminium thick target.

Case 6: $V_p = 14000\ m/s$

The final impact case of $V_p = 14000\ m/s$ confirms what is stated above. Figure 6.8a shows the projectile material in the debris cloud lagging farther and farther behind the leading edge, while Figure 6.8b shows very little glass material left on the front face. It stands to reason that for this single-wall system, the increase in velocity for constant mass results in a increase in momentum and kinetic energy, which in turn is proportional to the amount of damage that is caused.

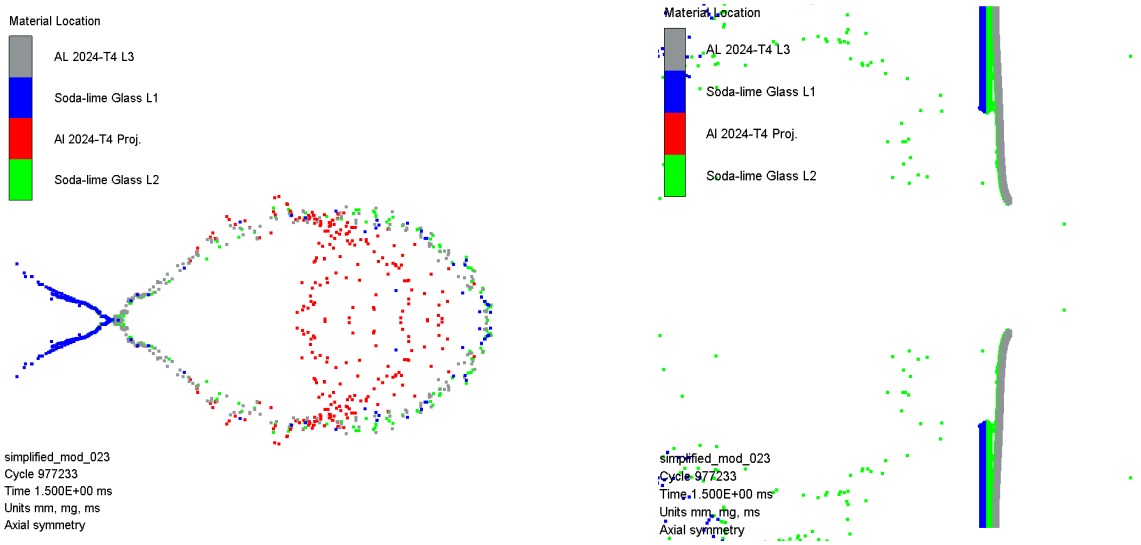

(a) Debris cloud produced by impact.

(b) Enlarged view focussing on impact site.

Figure 6.8: Simulated debris cloud and damage induced by using aluminium spheres of 1 mm diameter for $V_0 = 14000\ m/s$ at $t = 1.5\ ms$ after impact into a 0.7 mm glass-glass-aluminium thick target.

6.1.4. Results and Discussion

Table 6.1 contains all results for the glass-glass-aluminium configuration analysed in Section 6.1.

D_p (mm)	v_p (m/s)	m_p (mg)	p_p (mgm/s)	Ejecta Mass/ Projectile Mass	E_k $(Joules)$	MEF
1.0	1000	1.38	1380.66	15.09	0.69	0.0228
1.0	2000	1.38	2761.32	49.89	2.76	0.2958
1.0	3000	1.38	4141.98	33.24	6.21	0.2041
1.0	7000	1.38	9664.62	67.71	33.81	0.0938
1.0	10000	1.38	13806.60	72.64	69.00	0.0817
1.0	14000	1.38	19329.20	135.24	101.31	0.0691
1.5	1000	4.77	4765.79	6.92	2.38	0.0662
1.5	2000	4.77	9531.58	17.64	9.53	0.1229
1.5	3000	4.77	14297.40	23.55	21.45	0.1104
1.5	7000	4.77	33360.50	30.65	116.76	0.0433
1.5	10000	4.77	47657.90	24.85	238.29	0.0246
1.5	14000	4.77	66721.10	24.52	467.05	0.0238
2.0	1000	11.39	11391.20	6.89	5.70	0.0310
2.0	2000	11.39	22782.4	11.16	22.78	0.0716
2.0	3000	11.39	34173.60	13.83	51.26	0.0438
2.0	7000	11.39	79783.00	12.01	279.08	0.0171
2.0	10000	11.39	113912.00	11.82	569.55	0.0089
2.0	14000	11.39	159477.00	10.40	1116.32	0.0050
3.0	2000	38.77	77540.00	5.78	77.54	0.0334
3.0	3000	38.77	116310.00	7.43	174.47	0.0281
3.0	7000	38.77	271390.00	5.82	949.87	0.0122
3.0	10000	38.77	387700.00	5.34	1938.50	0.0060
3.0	14000	38.77	542780.00	5.19	3799.46	0.0048

Table 6.1: Overview of results for aluminium spheres of 1.0, 1.5 & 2.0 mm diameter striking 0.7 mm thick glass-glass-aluminium targets.

It was noticed during the 1000 m/s impact case that some strange phenomenon was occurring. During certain simulations, after the projectile had penetrated the target and was well downrange, it began to change direction and travel backwards in the negative x-direction. This made a significant contribution to the back-scattered ejecta momentum and resulted in wildly inaccurate simulations. Although this was not occurring in every case, it was a cause for concern. Upon analysing the plot shown in Figure 6.9, it is clear to see that there is an unexplainable drop in MEF for the 1000 m/s impact case.

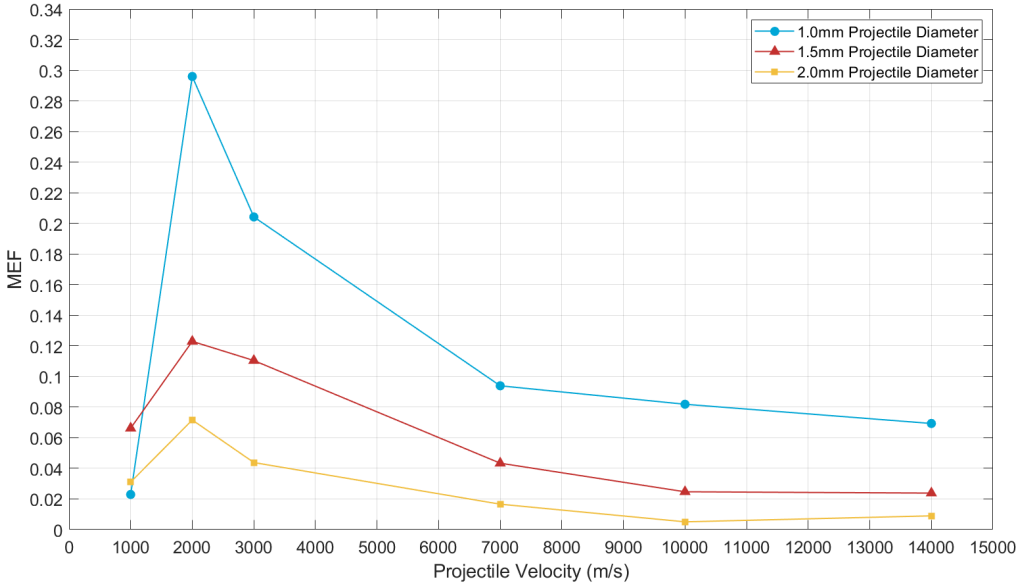

Figure 6.9: Simulated results of Projectile Velocity vs. Momentum Enhancement Factor (MEF) for aluminium spheres of 1.0, 1.5 & 2.0 mm diameter striking 0.7 mm thick glass-glass-aluminium targets - including 1000 m/s impact case.

It was only on further inspection that it was revealed there is an inherent issue with the Autodyn software at simulating low impact velocities. Although 1000 m/s may not seem low, in the context of hypervelocity impacts it certainly falls below this classification. Depending on the projectile and target material, a hypervelocity impact is classified as an impact occurring at approximately over 2500-3000 m/s. It is not certain whether this is the root cause of the problem as no reliable information could be found in the Autodyn manual. To visualise this issue, Figures 6.10a and 6.10b show a side-by-side comparison of the in-built Autodyn generated history plots for the 1000 m/s and 2000 m/s impact velocities respectively. Figure 6.10a shows a continued increase in x-momentum across all materials. This in turn results in a higher ejecta momentum/projectile momentum ratio and disproportionately decreases the MEF. In comparison, Figure 6.10b displays much more logical behaviour with the x-momentum plateauing after around 1 ms. These plots represent a projectile diameter of 1.0 mm but this behaviour was also present in the 1.5, 2.0 & 3.0 mm projectile diameter cases.

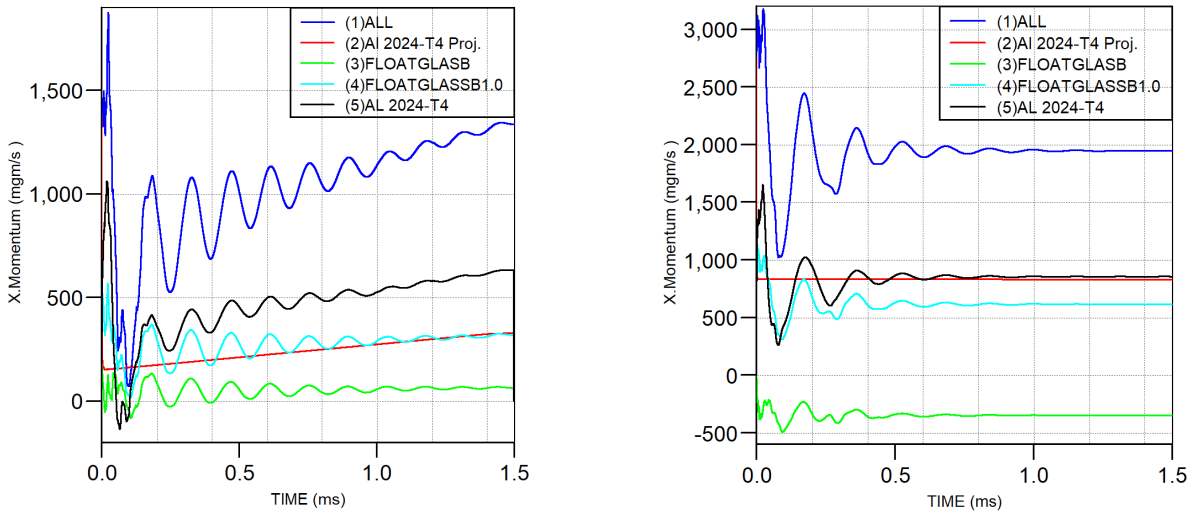

(a) 1000 m/s impact velocity.

(b) 2000 m/s impact velocity.

Figure 6.10: In-built Autodyn generated results of Time vs. X-Momentum for aluminium spheres of 1.0 mm diameter striking 0.7 mm thick glass-glass-aluminium targets.

Considering that Autodyn displays erratic results at velocities around and below 1000 m/s, the remainder of this thesis work will only consider impact velocities of above 2000 m/s where the simulation remains stable. In LEO regimes there won't be too many impacts less than 2000 m/s. In GEO however, the impact velocities will be much less in the range of a few hundred to approximately 4000 m/s [102]. Its worth noting that for GEO-specific analysis a more well-behaved model is required to capture these lower velocities where hypervelocity impact mechanics aren't present.

Figure 6.11 plots projectile velocity versus MEF starting at 2000 m/s and displays some interesting behavior, most notably the fact that the 2000 m/s impact velocity is the most efficient velocity for higher momentum enhancement factors across all projectile diameters. It stands to reason that the slower a projectile is travelling, the harder it will be for it to break through the target and hence the more momentum will be transferred. It is therefore safe to assume that for thin targets where complete perforation occurs, the lower the projectile velocity and hence momentum, the higher the MEF. In addition to this, it is expected that if Autodyn could have accurately modeled the 1000 m/s impact case, it would have yielded MEF results higher than the 2000 m/s case. This implies that velocity is inversely proportional to MEF for this given set up where complete perforation occurs.

Figure 6.12 shows the value trends for MEF as a function of projectile diameter in the glass-glass-aluminium target. As projectile diameter increases, MEF tends to decrease. This can be attributed to a few reasons, most notably the fact that for a given velocity, a smaller projectile will have less momentum than a larger one. This allows larger projectiles to more easily penetrate the target and results in a higher transfer of momentum to the ejecta rather than to the target itself. Indeed, at lower velocities of 2000-3000 m/s the effects of smaller

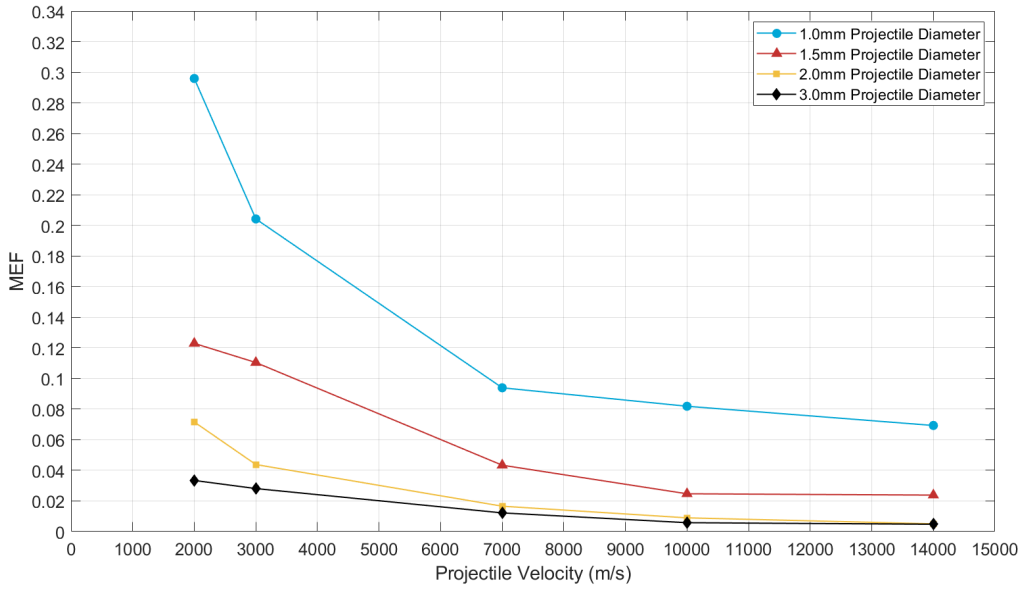

Figure 6.11: Simulated results of Projectile Velocity vs. Momentum Enhancement Factor (MEF) for aluminium spheres of 1.0, 1.5, 2.0 & 3.0 mm diameter striking 0.7 mm thick glass-glass-aluminium targets.

projectiles are much more prominent. Moving to higher velocities of 7000-14000 m/s, it can be seen that the MEF values are much lower and there is less of a negative correlation between them. This highlights that the faster and larger a projectile is, the less of an impact it will have on the momentum transfer.

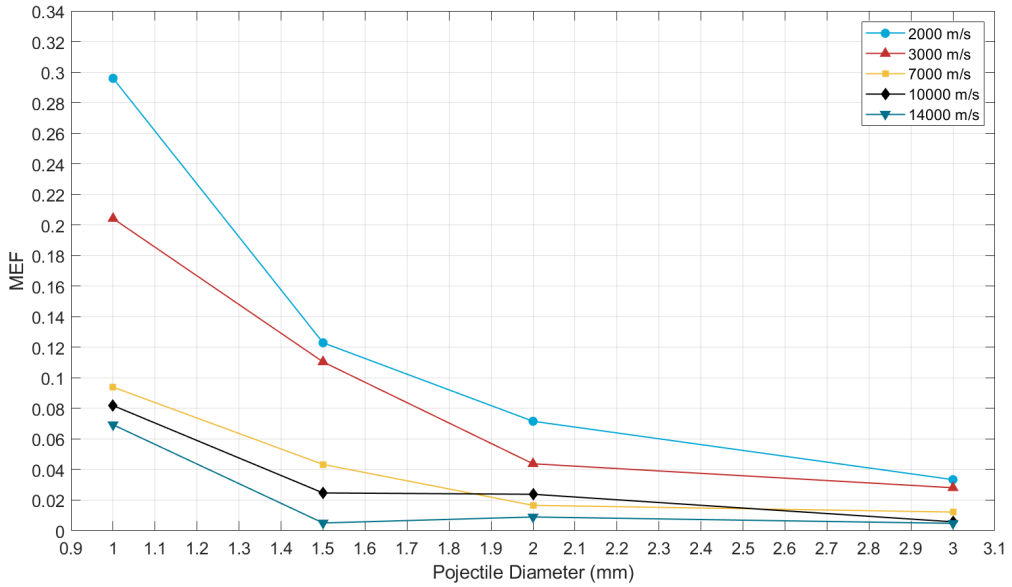

Figure 6.12: Simulated results of Projectile Diameter vs. Momentum Enhancement Factor (MEF) for aluminium spheres of 1.0, 1.5, 2.0 & 3.0 mm diameter striking 0.7 mm thick glass-glass-aluminium targets.

6.1.5. Constant Momentum Study

Now that its been illustrated how the MEF tends for given velocities, projectile momentum needs to be held constant in order to fully compare projectile size. As previously discussed in Section 6.1.4, Autodyn encounters difficulties when simulating impact velocities of around 1000 m/s and below. This means that it is not possible to achieve lower momentum values with larger projectiles as this would mean decreasing the velocity to very low and unstable values. In order to compare projectile momentum across all three diameters, the minimum projectile momentum that could be simulated was 20000 mgm/s. This resulted in impact velocities as high as 40000 m/s for the 1 mm projectile, and although this may be unrealistic in terms of space debris hypervelocity impacts, it serve to create a comparison. It is not however unrealistic for micrometeoroids with collision velocities being be much higher and reaching around 60000 m/s [103]. It is important to caveat though that the further away we get from test data in terms of impact velocity, the less confidence we should have in the results. The same way the impact physics change from the ballistic low-velocity collisions where the projectile remains more or less intact to a hypervelocity collision where everything fragments and becomes vaporised, the physics might also change again once you get to these much larger hypervelocity collisions and may have an effect on the accuracy of the models.

D_p (mm)	m_p (mg)	V_p (m/s)	p_p (mgm/s)	E_k $(Joules)$	MEF
1.0	1.38	14485.41	20000	144.85	0.0799
1.0	1.38	21728.11	30000	325.92	0.0543
1.0	1.38	28970.81	40000	579.42	0.0290
1.0	1.38	39834.87	55000	1095.46	0.0367
1.5	4.77	4192.87	20000	41.93	0.0688
1.5	4.77	6289.31	30000	94.34	0.0328
1.5	4.77	8385.74	40000	167.71	0.0496
1.5	4.77	11530.40	55000	317.09	0.0264
2.0	11.39	1755.93	20000	17.56	0.1023
2.0	11.39	2633.89	30000	39.51	0.0523
2.0	11.39	3511.85	40000	70.24	0.0418
2.0	11.39	4828.80	55000	132.79	0.0313

Table 6.2: Overview of results for aluminium spheres of 1.0, 1.5 & 2.0 mm diameter striking 0.7 mm thick glass-glass-aluminium targets with constant momentum.

Figure 6.13 presents the data observed in Table 6.2. The results demonstrate that for this projectile momentum range, the slopes of the lines representing the change in MEF as diameter increases are more or less flat. This indicates that for a given projectile momentum above 20000 mgm/s, even though the points jump around a bit, the MEF tends to remain fairly steady. Although this is an important observation, it is not necessarily that relevant so far as real

life LEO impacts are concerned. It is very unlikely that a man-made debris particle will be travelling at velocities above 40000 m/s. However, it is possible that micrometeoroids could impact at such velocities and therefore still bears significance. Of course, it can seen that as momentum increases, MEF decreases across all projectile diameters. This highlights that the higher the projectile momentum, the lower the percentage of momentum is transferred to the target.

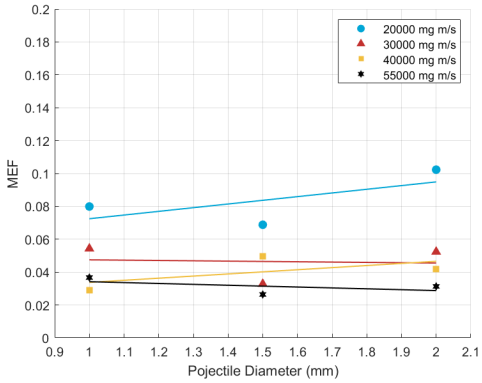

(a) Projectile Diameter vs. Momentum Enhancement Factor (MEF)

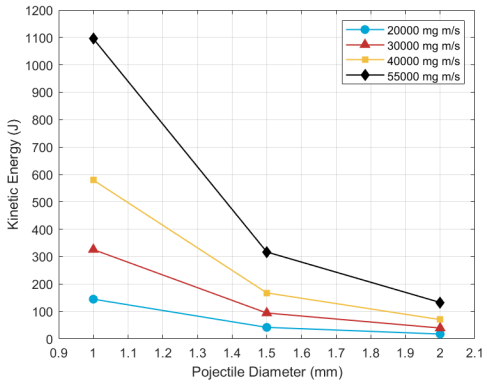

(b) Projectile Diameter vs. Kinetic Energy

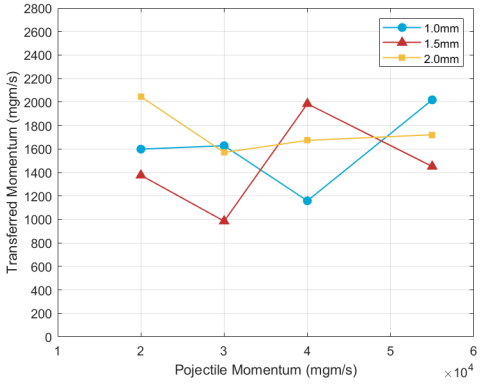

(c) Projectile Momentum vs. Transferred Momentum

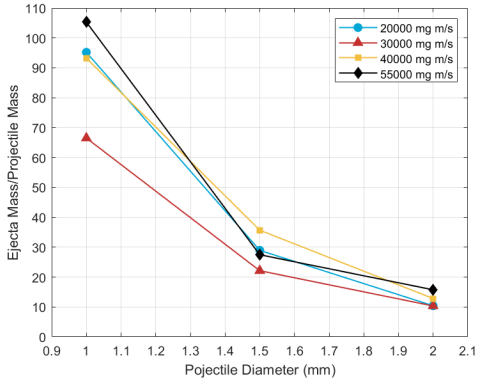

(d) Projectile Diameter vs. Normalised Ejecta Mass

Figure 6.13: Simulated results for aluminium spheres of 1.0, 1.5 & 2.0 mm diameter striking 0.7 mm thick glass-glass-aluminium targets with constant momentum.

As shown in Figure 6.13a when projectile momentum is held constant within this range, size doesn't have a major effect on the MEF. Intuitively, one would expect that at constant momentum, smaller projectiles would inflict more damage due to the higher kinetic energy of the object. When momentum is held constant, kinetic energy is inversely proportional to mass, meaning that smaller objects will have a higher kinetic energy as highlighted in Figure 6.13b. This is driven by the square of the velocity term in the kinetic energy equation. Considering that the kinetic energy of a projectile is directly proportional to how much damage it will inflict when it hits the target, at a constant momentum, smaller projectiles should induce more damage.

To quantify and compare the overall effect of projectile size at constant momentum, projectile momentum is plotted against transferred momentum in Figure 6.13c. It is observed that there is no discernible trend in the relationship. That is, a smaller particle can impart similar amounts of momentum as a larger one at equivalent initial momentum, but this relationship very much varies as the initial momentum increases.

When ejecta mass is normalised by projectile mass as illustrated in Figure 6.13d, it is observed that there is s a significant difference in the amount of ejecta generated when projectile size increases. It is clear that the smaller a projectile is, the more efficient it becomes at producing ejecta and this can be attributed to the higher kinetic energy of the object. A smaller projectile being more efficient just means that roughly the same amount of momentum will be delivered by a variety of projectiles and speeds. However, this will not remain true for every smaller projectile, as eventually the critical size of the projectile will be surpassed where perforation does not occur and the MEF will increase dramatically.

It can therefore be concluded that for the conditions used in these simulations, projectile size has little effect on MEF when projectile momentum is held constant. The kinetic energy of the particle ensures that smaller projectiles yield the same amount of of ejecta mass as larger projectiles while momentum is held constant.

6.2. Glass-Silicon-Aluminium Configuration

The second target that was simulated was the glass-silicon-aluminium configuration. This section outlines the results obtained using the same input parameters as Section 6.1.

6.2.1. Model Setup

Similarly to Section 6.1, the coverglass was modelled as soda-lime glass and the substrate layer was modelled as Al 2024-T4. The silicon layer however was modelled using the proposed material model presented by Michel [81]. Unfortunately there is no experimental data available for silicon validation meaning that this run of simulations is only a proposed model. The same projectile conditions, SPH particle packing size and boundary conditions were imposed as in Section 6.1 in order to present a direct comparison between the two target configurations.

The lack of published data on the behaviour of silicon under hypervelocity impact makes it incredibly difficult to understand how it will behave. The limited number of previous studies have concluded that silicon displays a brittle material damage morphology [104]. Therefore its behaviour is comparable to brittle materials like glass.

6.2.2. Results and Discussion

Table 6.3 contains all results for the glass-silicon-aluminium configuration.

D_p (mm)	v_p (mg)	m_p (m/s)	p_p (mgm/s)	Ejecta Mass/ Projectile Mass	E_k $(Joules)$	MEF
1.0	2000	1.38	2761.32	22.83	2.76	0.2449
1.0	3000	1.38	4141.98	39.42	6.21	0.2181
1.0	7000	1.38	9664.62	58.45	33.81	0.0476
1.0	10000	1.38	13806.60	53.62	69.00	0.0732
1.0	14000	1.38	19329.20	54.42	135.24	0.0325
1.5	2000	4.77	9531.58	11.92	9.53	0.0968
1.5	3000	4.77	14297.40	16.21	21.45	0.0815
1.5	7000	4.77	33360.50	21.04	116.76	0.0406
1.5	10000	4.77	47657.90	20.82	238.29	0.0250
1.5	14000	4.77	66721.10	22.47	467.05	0.0204
2.0	2000	11.39	22782.40	8.22	22.78	0.0660
2.0	3000	11.39	34173.60	10.12	51.26	0.0577
2.0	7000	11.39	79783.00	10.32	279.08	0.0201
2.0	10000	11.39	113912.00	11.70	569.55	0.0145
2.0	14000	11.39	159477.00	12.38	1116.32	0.0105

Table 6.3: Overview of results for aluminium spheres of 1.0, 1.5 & 2.0 mm diameter striking 0.7 mm thick glass-silicon-aluminium targets.

Figure 6.14 plots projectile velocity versus MEF starting at 2000 m/s and displays more or less the same behavior as the glass-glass-aluminium configuration presented in Figure 6.11. Apart from the spike in MEF at 10000 m/s for the 1 mm projectile, the lines tend to follow an inversely proportional relationship.

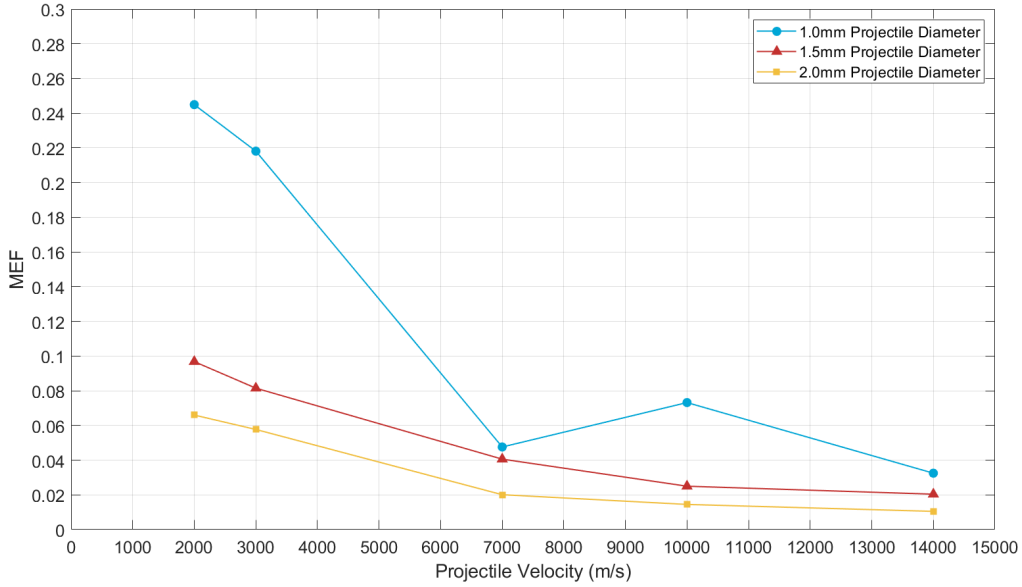

Figure 6.14: Simulated results of Projectile Velocity vs. Momentum Enhancement Factor (MEF) for aluminium spheres of 1.0, 1.5 & 2.0 *mm* diameter striking 0.7 *mm* thick glass-silicon-aluminium targets.

The ejecta mass and MEF values obtained for the glass-glass-aluminium and the glass-silicon-aluminium targets are compared in Figure 6.15. It is apparent from Figure 6.15a that for each projectile diameter simulated, the glass-silicon-aluminum target produces less ejecta mass than the previously simulated glass-glass-aluminium target. This implies that the silicon material used has a higher resistance under hypervelocity impact than the glass, meaning that it is tougher and shatters less easily.

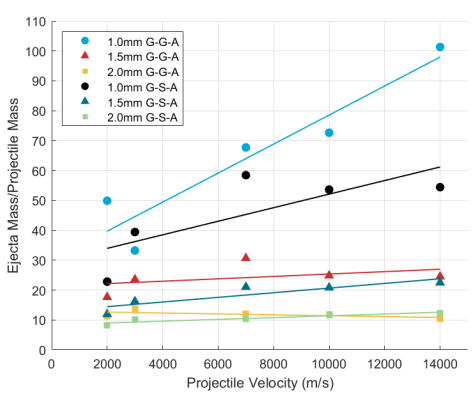

(a) Projectile Velocity vs. Normalised Ejecta Mass

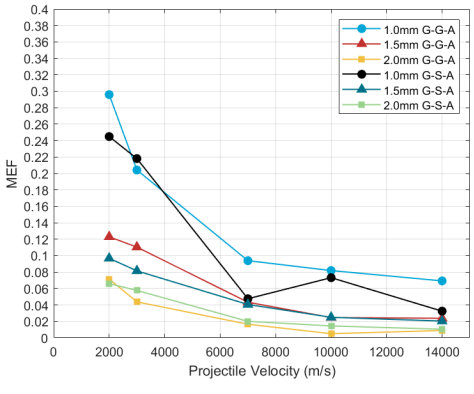

(b) Projectile Velocity vs. Momentum Enhancement Factor (MEF)

Figure 6.15: Simulated results for aluminium spheres of 1.0, 1.5 & 2.0 *mm* diameter striking 0.7 *mm* thick glass-glass-aluminium targets vs. glass-silicon-aluminium targets

Looking at Figure 6.16, it is quite evident that the silicon is less susceptible to brittle fracture than the glass as more of it is intact. Interestingly, the lower quantity of ejecta mass doesn't correspond to an increase in MEF. On account of the fact that MEF tends to decrease as ejecta mass generation increases, it was expected that Figure 6.15b would show higher MEF values for the glass-silicon-aluminium target. This is not the case however. The general tendency of MEF values for the glass-silicon-aluminium target are below those of the glass-glass-aluminium target. This underlines that although more ejecta mass may be produced, it does not necessarily mean that less momentum will be transferred to the target. Due to the fact that more of the silicon is intact, less material was ejected and hence a higher proportion of the projectile momentum had to be transferred to less material.

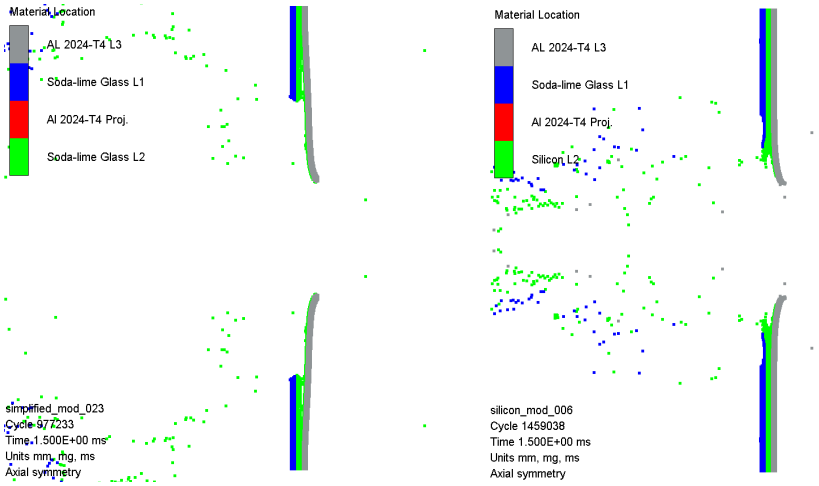

(a) Glass-glass-aluminium target **(b)** Glass-silicon-aluminium target

Figure 6.16: Glass-glass-aluminium target vs. Glass-silicon-aluminium target for 1mm aluminum spheres at 14000 m/s.

The approach utilised suffers from the limitation that the silicon material model could not be validated due to lack of experimental data. It is worth stressing again that this is a proposed estimate of the behaviour of silicon and cannot be confirmed.

6.3. Summary

The aim of this chapter was to define the MEF values for various projectile sizes in the 1-3 mm range. For the impact velocity regime of 2000-14000 m/s, these values have been found to lie in the region of 0.0048 to 0.2958 for the glass-glass-aluminium target and 0.0105 to 0.2449 for the glass-silicon-aluminium target. Once the projectiles breach around the 7000 m/s point, they enter into the melt/vaporisation range and this is where the projectiles become substantially melted and where we see the MEF tending the plateau. This is an important observation, particularly when considering LEO impacts as most are in the range of 10000-14000 m/s. The 1 mm projectile recorded an MEF of 0.0817 at 10000 m/s, meaning that this is likely to

be on average the highest value of MEF experienced in LEO for this particular solar array configuration among the debris size range studied.

When equivalent momentum was used in the range of 20000-55000 mgm/s for the 1-2 mm projectiles, it was observed that size did not display any obvious trends in influencing the MEF and is more or less the same across all diameters. There is, however, some uncertainty in these results. For example the $1mm$ had to be simulated at speeds of approximately 40000 m/s in order to reach an equivalent momentum of 55000 mgm/s. There are no experimental results that can reach even close to these speeds so the behaviour of the materials in these kinds of regimes is unknown.

7

Projectile Material Study

After successfully implementing the solar array model in Autodyn and obtaining results for the projectile size study, this chapter deals with analysing the effects of two other projectile materials, namely copper and glass. The results are compared to those recorded for the Al 2024-T4 projectile and some inferences are made.

7.1. Model Setup

In order to study the effects that various projectile materials have on MEF values, it was proposed to simulate some common space materials which fell into the categories of low, medium and high density objects. The most common projectile material used in HVI testing to date has been Aluminium [88]. A range of grades have been tested, including Al 2017, Al 2017-T4 and Al 2024-T4. Due to the fact that Al 2024-T4 has already been validated in Section 4.2.1 and is ready available in Autodyn, it was selected as the Aluminium projectile for this study. This will hopefully facilitate any future studies regarding momentum transfer.

Initially three other projectile materials were chosen, namely glass, copper and CFRP. Fragmentation of solar arrays, spacecraft shielding and other components has lead to large populations of these materials and so studying their influence on momentum transfer is very beneficial. Some initial studies were conducted which revealed that the CFRP material model majorly increased computation time. This resulted in only copper and glass being used as numerous simulations could be carried out more efficiently. The copper model uses a shock EOS and a Steinberg-Guinan strength model taken from Price et al. [105] and implements a hydrostatic failure model as Murr et al. [89] have done with a hydrostatic tensile pressure value of of 0.2 GPa. The material models for aluminium, copper and glass can be found in Appendix A. In order to compare the materials, spherical projectiles of diameters 1, 1.5 and 2.0 mm were simulated at velocities of 2000, 3000, 7000, 10000 and 14000 m/s. Similarly to Section 6.1, the

glass-glass-aluminium target configuration was used with an SPH packing size of 0.05 mm

7.2. Results and Discussion

Table 7.1 contains all results for the glass projectile study.

Material	D_p (mm)	V_p (m/s)	m_p (mg)	p_p (mgm/s)	Ejecta Mass/ Projectile Mass	E_k $(Joules)$	MEF
Copper	1.0	2000	4.43	8854.00	9.32	8.85	0.0671
Copper	1.0	3000	4.43	13281.00	18.56	19.92	0.0560
Copper	1.0	7000	4.43	30989.00	35.62	108.46	0.0383
Copper	1.0	10000	4.43	44270.00	22.74	221.35	0.0274
Copper	1.0	14000	4.43	61978.00	25.80	433.85	0.0169
Glass	1.0	2000	1.25	2508.40	27.91	2.51	0.3458
Glass	1.0	3000	1.25	3762.60	57.80	5.64	0.2309
Glass	1.0	7000	1.25	8779.40	79.31	30.73	0.1191
Glass	1.0	10000	1.25	12542.00	101.07	62.71	0.0920
Glass	1.0	14000	1.25	17558.80	105.77	122.91	0.0735
Glass	1.5	2000	4.33	8658.80	14.37	8.66	0.1610
Glass	1.5	3000	4.33	12988.20	27.06	19.48	0.1149
Glass	1.5	7000	4.33	30305.80	29.98	106.07	0.0563
Glass	1.5	10000	4.33	43294.00	28.01	216.47	0.0430
Glass	1.5	14000	4.33	60611.60	29.04	424.28	0.0353
Glass	2.0	2000	10.35	20696.00	13.13	20.70	0.0766
Glass	2.0	3000	10.35	31044.00	10.52	46.57	0.0483
Glass	2.0	7000	10.35	72436.00	13.86	253.53	0.0211
Glass	2.0	10000	10.35	103480.00	13.07	517.40	0.0144
Glass	2.0	14000	10.35	144872.00	12.76	1014.10	0.0159

Table 7.1: Overview of results for glass spheres of 1.0, 1.5 & 2.0 mm diameter striking 0.7 mm thick glass-glass-aluminium targets.

Figure 7.1 plots projectile velocity versus MEF for the aluminium copper and glass projectiles. Generally speaking, the glass projectiles result in larger MEF values across all projectile diameters bar the 3000 m/s impact case where the aluminium projectile has a larger MEF value. The density of glass is 2.53 mg/mm^3 compared to 2.785 mg/mm^3 for Al 2024-T4. This obviously has a direct influence on the mass and hence momentum of the projectile. As previously concluded in Section 6.1.4, the larger the initial projectile momentum, the smaller the value for MEF. Considering that the glass projectiles have less momentum, it is no surprise that they induce more efficient momentum transfer. The influence of density can also be seen amongst the 1 mm copper projectiles which have much lower MEF values than their aluminium

and glass 1 mm counterparts. The 1 mm copper results are actually more akin to the 2.0 mm aluminum and glass projectiles. The density of copper is 8.93 mg/mm^3, making it 3.2 times higher than aluminium, and 3.5 times larger than glass. This relates to an MEF increase of between 3.11-5.15 from copper to glass and 2.45-4.41 for copper to aluminium. It is important to caveat that these values are not representative of every HVI case that use these materials, but rather the specific thin-layered structure that was modelled in these simulations.

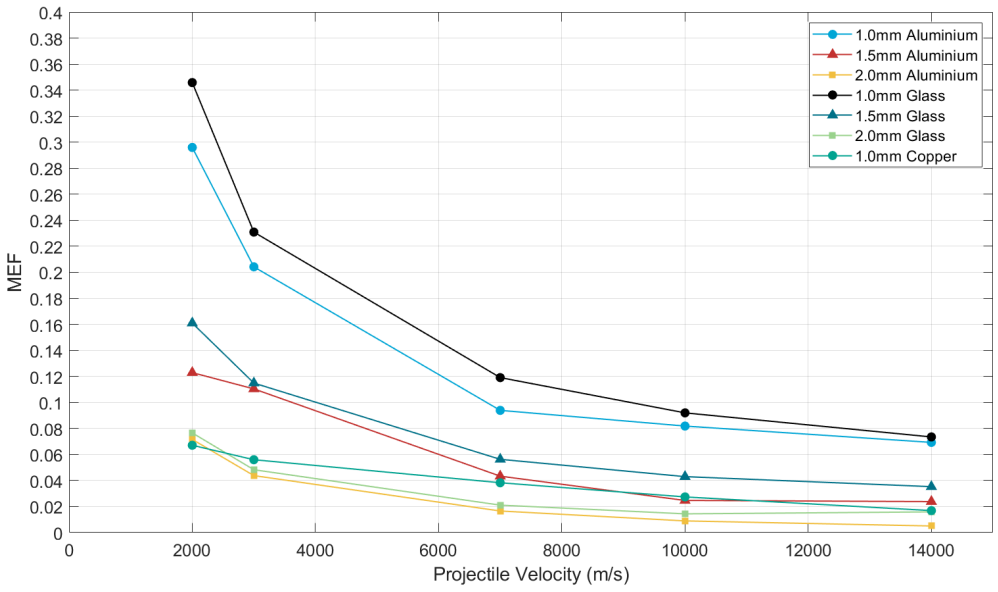

Figure 7.1: Simulated results of Projectile Velocity vs. Momentum Enhancement Factor (MEF) for aluminium and glass spheres of 1.0, 1.5 & 2.0 mm diameter striking 0.7 mm thick glass-glass-aluminium targets.

The amount of ejecta mass generated by both the aluminium and glass projectiles is illustrated in Figure 7.2. The 1.0 mm glass projectile yields higher ejecta mass generation for every impact velocity except 2000 m/s where the aluminium projectile actually produces more. This same behaviour is observed for the 1.5 mm projectiles. The 2.0 mm projectiles display some slightly different behaviour however, with the glass producing more ejecta than the aluminium apart from the 3000 m/s impact case. Although the 1.0 & 1.5 mm aluminium projectiles generate greater quantities of ejecta than the glass for 2000 m/s, it does not correspond to larger MEF values.

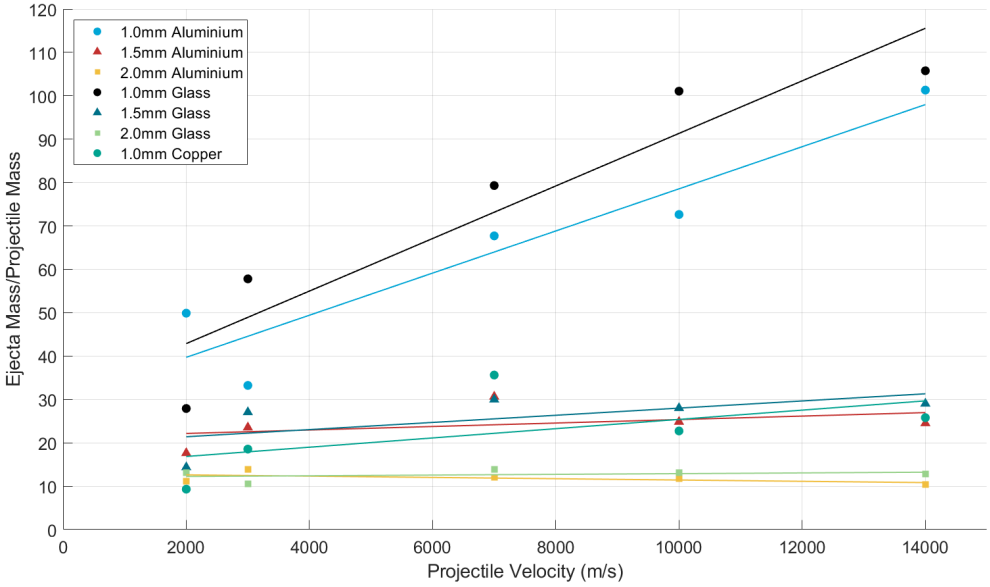

Figure 7.2: Simulated results of Projectile Velocity vs. Normalised Ejecta Mass for aluminium and glass spheres of 1.0, 1.5 & 2.0 mm diameter striking 0.7 mm thick glass-glass-aluminium targets.

Comparing the impact sites of the 1.0 mm projectiles at 2000 m/s, we see in Figure 7.3a that the glass projectile hasn't caused as much spallation as the aluminum projectile has in Figure 7.3b. It is reasonably assumed that these glass chippings are the cause of the ejecta mass difference. While these are significantly large fragments, they have only broken off the target just before the simulation cut-off time of 1.5 ms and therefore do not make any considerable contribution to the MEF due to their low velocity. These slow moving spalls explain why the ejecta mass is larger and the MEF is not.

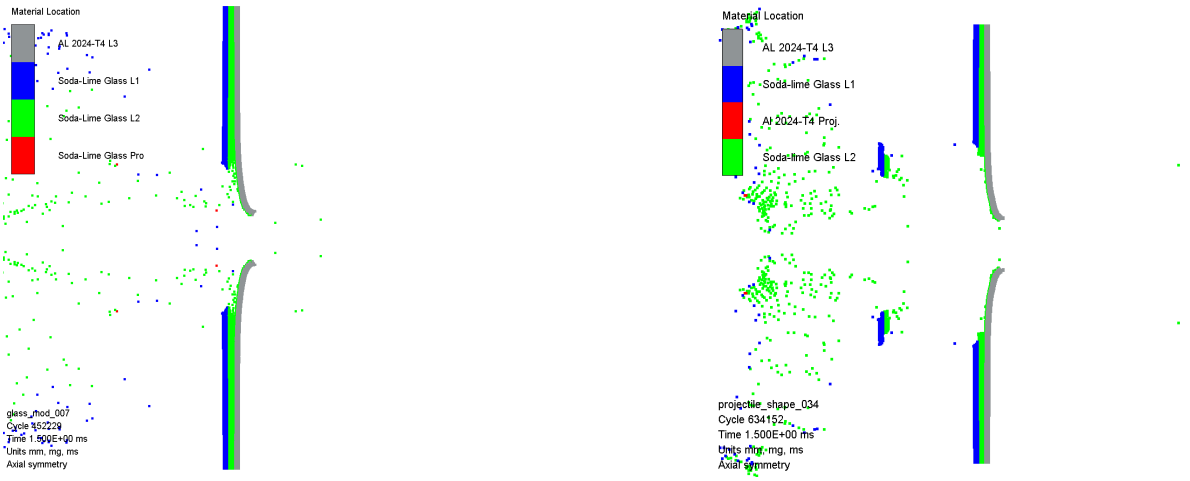

(a) 1.0 mm glass projectile

(b) 1.0 mm aluminium projectile

Figure 7.3: Impact sites of glass-glass-aluminium target using 1.0 mm glass and aluminium projectiles at 2000 m/s.

Of course the 1.5 mm projectiles also displays this behaviour at 2000 m/s. Analysing the impact sites of the aluminium and glass projectiles, there is more intact material present on the target in Figure 7.4a, albeit not a lot. Again, this does not lead to any significant change in the MEF as there is some substantial material to the left of the target in Figure 7.4b which has just broken off with an average x-direction velocity of ∼-5 m/s.

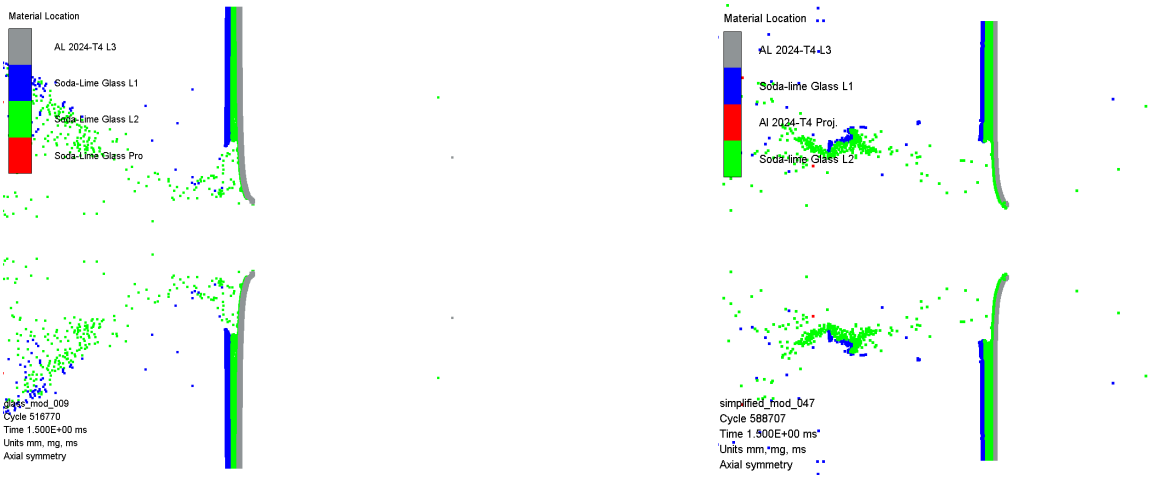

(a) 1.5 mm glass projectiles

(b) 1.5 mm aluminium projectiles

Figure 7.4: Impact sites of glass-glass-aluminium target using 1.5 mm glass and aluminium projectiles at 2000 m/s.

This behaviour is prevalent across the graph in Figure 7.2 and demonstrates that although normalised ejecta mass production might vary up and down between different projectile materials, the MEF follows a more distinct trend. This means that assessing target damage as a parameter to make inferences about MEF values of unknown projectile variables like size and velocity is not a reasonable practise.

7.3. Summary

The results of this chapter have shown that density plays a critical role in effecting MEF values. Low-density materials like glass and aluminium have less initial momentum which result in larger MEF values. Copper on the other hand is a lot denser, resulting in much lower MEF values. It has also been shown that for material with similar densities like glass and aluminium, MEF doesn't change much between them, though the target damage may be a little different. This is a result of glass chippings breaking off of the target late into the simulation. Although these have large masses, their velocities are extremely low and therefore are negligible when considering back-scattered ejecta momentum.

8

Projectile Shape Study

Although spherical projectiles have been the most studied throughout literature, they do not constitute common debris shapes. More realistic debris fragments might be better represented by more irregular shapes. This chapter explores the influence that projectile shape has on MEF by simulating a cone, cylinder and punch to compare against the results obtained for the spherical projectile. This is done by analysing the projectile shape effects for ejecta mass and MEF in Sections 8.2.1 and 8.2.2 respectively, and also ejecta angle effects for MEF in Section 8.2.3.

8.1. Model Setup

Six different projectile shapes were simulated at 2000, 3000, 7000, 10000 and 14000 m/s. Similarly to Section 6.1, the glass-glass-aluminium target configuration was used with an SPH packing size of 0.05 mm. The projectile material employed throughout the entirety of this projectile shape study was Al 2024-T4. The shapes that were chosen were a sphere, cone, cylinder, cup and punch. In order to size the different projectile shapes correctly, the volume of the 1 mm spherical projectile was recorded and used as a baseline for the other projectiles. Keeping this constant, the various parameters like inner & outer radius, length and cone length could be adjusted accordingly in order to achieve the target volume of 0.52 mm^3. Table 8.1 provides an overview of these shape parameters and values.

Projectile Shape	Outer Radius (mm)	Inner Radius (mm)	Length (mm)	Cone Length (mm)	Volume (mm^3)
Sphere	0.50	-	-	-	0.52
Cone	0.50	-	0.57	0.29	0.52
Cylinder	0.50	-	0.67	-	0.52
Cup	0.50	0.30	1.04	-	0.52
Punch	0.50	-	0.80	0.40	0.52

Table 8.1: Various parameters used in the sizing of the projectile shape study.

CAD renderings of the different projectiles were made in SolidWorks and are presented in Table 8.2. This shows both 2D and 3D visualisations of the projectile shapes. The projectile profiles aim to represent the basic shapes of various debris fragments. The objective was to select shapes that will maximise the amount of ejecta generated in order to examine the worst possible outcome for structures. The sphere is the standard shape tested throughout literature and therefore was selected to facilitate future studies. The cylinder was selected for its blunt profile and therefore its potential to excavate large amounts of ejecta. The cone and punch shapes were chosen to examine the effects of projectiles with pointed tips and edges and finally the cup was decided upon in order to determine if projectile porosity influenced the MEF.

	Sphere	Cone	Cylinder	Cup	Punch
3D				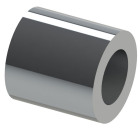	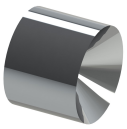
2D	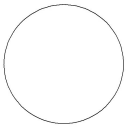	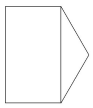	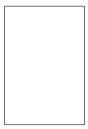	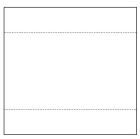	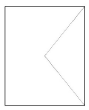

Table 8.2: Projectile shape CAD representations.

8.2. Results and Discussion

While running the cup shape simulations, certain issues arose which drastically increased simulation time and also reduced the accuracy of the simulations. Due to the narrow 0.2 mm profile of the cup shape in 2D, the amount of SPH particles was reduced significantly and didn't allow the simulations to run correctly. Of course, the SPH packing size could have been decreased to compensate for this, but this would have resulted in much longer simulation times. A decision was made not to proceed any further with the cup shape and just focus on the sphere, cone, cylinder and punch shapes. As illustrated in Figure 8.1, the projectiles are

relatively straight forward to model in Autodyn. The only constraint is that they must be symmetrical about the x-axis or axis of symmetry.

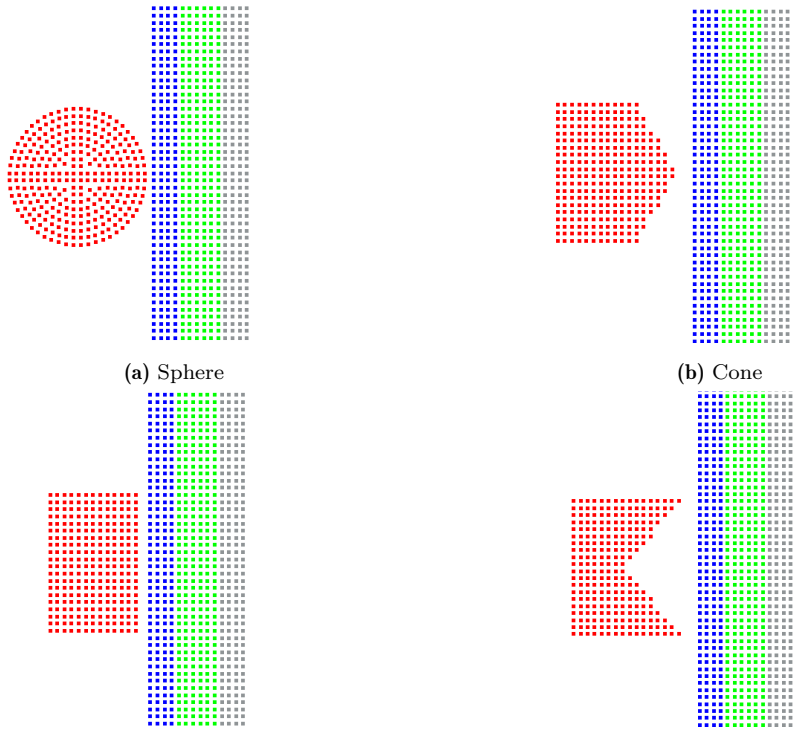

(a) Sphere **(b)** Cone

(c) Cylinder **(d)** Punch

Figure 8.1: Various enlarged images of projectile shapes modelled in Autodyn.

Simulation times varied across the different projectile shapes ranging from 72-96 hours depending on impact velocity and shape. The results are presented in Table 8.3. At first glance, its clear that the mass of the projectiles varies slightly across the different shapes. This in turn has a direct influence on the momentum and kinetic energy of the projectile. This slight variation can be attributed to the SPH particle packing of the objects. It was found that the jagged lines created when the perimeter of the shape was neither circular nor parallel/perpendicular to the axis of symmetry resulted in very minor packing inconsistencies. Of course this only resulted in a mass difference of $\pm$ 0.09 mg, but still lead to moderately larger differences in projectile momentum and kinetic energy. In order to overcome this variation, the ejecta mass was normalised by projectile mass. This meant that for the same impact velocity, material and other controlled parameters, geometrical shape of the projectiles could be compared.

Shape	v_p (m/s)	m_p (mg)	p_p (mgm/s)	Ejecta Mass/ Projectile Mass	E_k $(Joules)$	MEF
Sphere	2000	1.38	2761.32	49.89	2.76	0.2958
Sphere	3000	1.38	4141.98	33.24	6.21	0.2041
Sphere	7000	1.38	9664.62	67.71	33.81	0.0938
Sphere	10000	1.38	13806.60	72.64	69.00	0.0817
Sphere	14000	1.38	19329.20	101.31	135.24	0.0691
Cone	2000	1.46	2920.09	33.58	2.92	0.3620
Cone	3000	1.46	4380.14	32.45	6.57	0.1589
Cone	7000	1.46	10220.30	68.71	35.77	0.1165
Cone	10000	1.46	14600.50	86.86	73.00	0.0897
Cone	14000	1.46	20440.60	75.63	143.08	0.0488
Cylinder	2000	1.42	2843.53	46.12	2.84	0.3731
Cylinder	3000	1.42	4265.30	66.10	6.40	0.2385
Cylinder	7000	1.42	9952.37	87.75	34.83	0.1296
Cylinder	10000	1.42	14217.70	109.35	71.09	0.0929
Cylinder	14000	1.42	19904.70	95.10	139.34	0.0744
Punch	2000	1.47	2931.03	24.16	2.93	0.1084
Punch	3000	1.47	4396.54	29.28	6.59	0.0838
Punch	7000	1.47	10258.60	63.91	35.90	0.0828
Punch	10000	1.47	14655.10	69.49	73.28	0.0792
Punch	14000	1.47	20517.20	92.06	143.62	0.0674

Table 8.3: Overview of results for a variety of aluminium shapes striking 0.7 mm thick glass-glass-aluminium targets.

Figure 8.2 presents the relation between impact velocity and MEF for each projectile shape. From initial examination it can be seen that the MEF values for the sphere, cone and cylinder shapes follow the same trend as previously discussed in Section 6.1.4 and become smaller as impact velocity increases. They begin quite high for the 2000 m/s impact case and then proceed to fall quite rapidly until they reach around 7000 m/s where they start to even out. The MEF values for the punch shape also decrease as velocity grows, but displays more neutral behaviour and does not appear to have as much of an effect on MEF as opposed to the other shapes. Overall, the MEF values range from 0.0264-0.3731, and display substantial variations particularly when compared to the punch shape. To understand the reasoning behind these differences three main mechanisms are considered, namely, projectile shape effects for ejecta mass and MEF and ejecta angle effects for MEF which are discussed in the following sections.

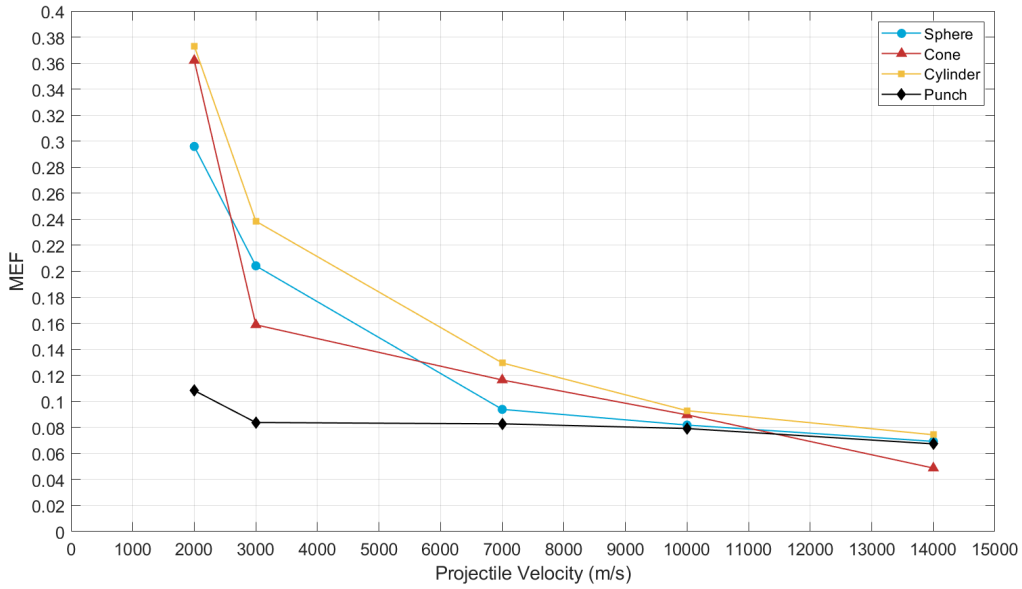

Figure 8.2: Simulated results of Projectile Velocity vs. Momentum Enhancement Factor (MEF) for a variety of aluminium shapes striking 0.7 *mm* thick glass-glass-aluminium targets.

8.2.1. Projectile Shape Effects for Ejecta Mass

The quantity of ejecta generated upon impact is one of the most important factors when calculating the MEF. In order to show these effects, impact velocity was plotted against normalised ejecta mass for each projectile shape. The ejecta mass was normalised in order to negate any slight variation in mass difference across projectile shapes and yields a dimensionless number which is representative of the amount of ejecta produced by that specific impact. MATLAB's *polyfit* function was used in order to compute a least-squares fit and follow a linear regression approach. Looking at Figure 8.3 it can be seen that the slopes of each ejecta mass function are quite comparable. The blunt shape of the sphere and cylinder projectiles enable them to have more surface area contact upon impact and therefore produce slightly more debris than the cone and punch shapes. The sharper tips on these projectiles make them easier to deform and result in smaller crater sizes. Since crater size is proportional to the amount of ejecta produced, the more blunt projectiles will yield higher amounts of ejecta.

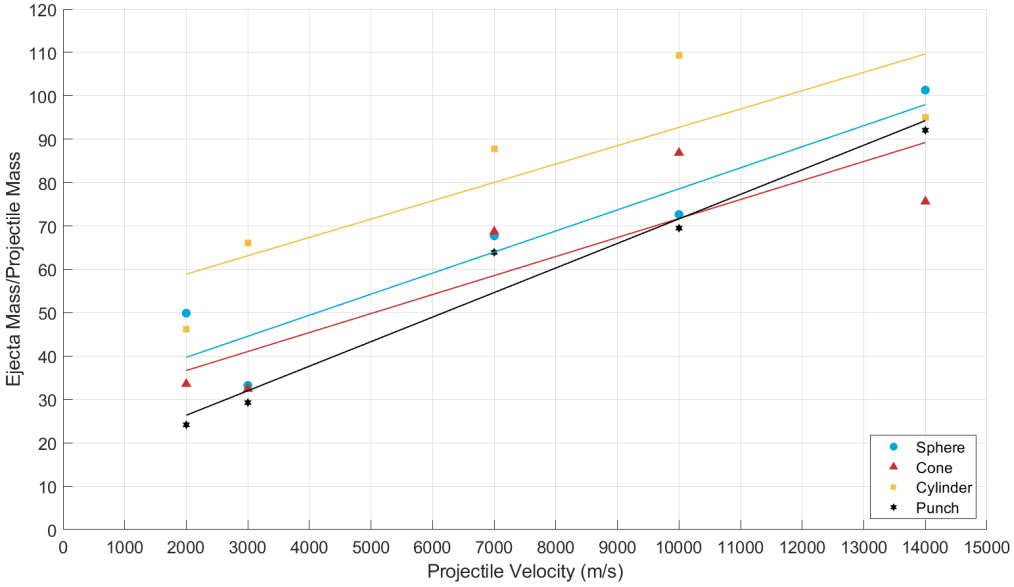

Figure 8.3: Simulated results of Projectile Velocity vs. Normalised Ejecta Mass for a variety of aluminium shapes striking 0.7 *mm* thick glass-glass-aluminium targets.

8.2.2. Projectile Shape Effects for MEF

Although the quantity of generated ejecta is important in MEF calculation, the projectile size effect is compared by considering the efficiency of this ejecta. To illustrate this, simulation results are presented in Figure 8.4a which plots projectile momentum against MEF and Figure 8.4b which plots projectile momentum against normalised ejecta mass. For the sake of comparison, projectile momentum is used on the horizontal axis in both cases. This enables an assessment of the tendency of the MEF and normalised ejecta mass in the context of momentum enhancement.

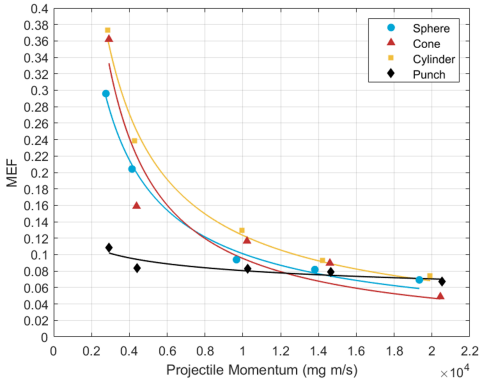

(a) Projectile Momentum vs. Momentum Enhancement Factor (MEF)

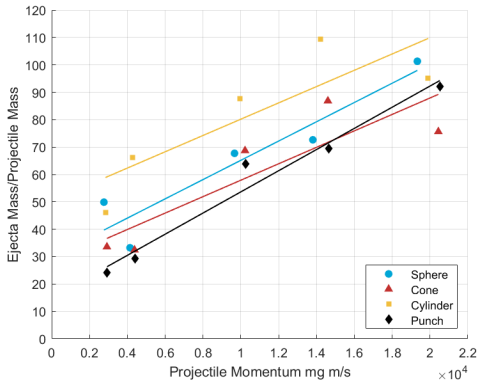

(b) Projectile Momentum vs. Normalised Ejecta Mass

Figure 8.4: Simulated results for a variety of aluminium shapes striking 0.7 *mm* thick glass-glass-aluminium targets.

Looking at Figure 8.4a, MEF tends to decrease as projectile momentum increases across all shapes. For the same initial projectile momentum, the MEF of the cylinder shape was maximal, followed by the cone, sphere, and finally punch. As the velocity and hence momentum of the projectile increases, we notice how the projectile shape seems to play less of a role in influencing the MEF. Interestingly, it is around the 10000 mgm/s point where the spread of MEF data for the different shapes begins to reduce and cluster. This corresponds to around 7000 m/s, which is significant as it approximates the transition from the shatter range to the melt/vaporisation range as highlighted back in Figure 6.2. As the projectiles enter this regime, they become completely fragmented and vaporise to the extent that shape plays much less of a role in MEF calculation.

As previously outlined in Section 8.2, the punch shape has a much less negative slope than the other projectile shapes. This result was not expected as it was anticipated that the target was too thin for the projectile shape to make any meaningful difference. A possible explanation for this result may be due to the fact that the punch shape has a higher porosity than other shapes. The front face is predominantly hollow which reduces density and hence MEF. This highlights that even when the target is extremely thin and complete perforation occurs, the MEF can be very sensitive to projectile shape, particularly at lower impact velocities.

It was expected that as the quantity of ejecta mass increased, so too would the ejecta momentum which would in turn result in a drop in MEF. Looking at Figure 8.4b however, this did not turn out to be the general case. The cylinder recorded the highest figures for ejecta mass, while also having the highest MEF values. This means that more of the projectiles initial momentum was transferred to the target rather than to the ejecta, resulting in more efficient momentum transfer. By this reasoning, the projectile shape which produced the lowest amount of ejecta mass should then yield the lowest MEF values, which is observed with the punch shape. However, the cone and sphere shapes do not uphold this logic. The sphere generates more ejecta mass than the cone, but yet has lower MEF values. This demonstrates that the influence of ejecta mass on momentum transfer varies from shape to shape and that there is some other mechanism influencing momentum transfer.

8.2.3. Ejecta Angle Effects for MEF

To explore this further, consideration needs to be given to what happens when the projectile perforates the target. From Figure 6.4a, it can be seen that for the 2000 m/s impact, the projectile remains more or less in tact as opposed to the higher impact velocities. Furthermore, the spread angle of ejecta is far smaller. It stands to reason that for larger angles of ejecta emission, the resulting ejecta velocity in the x-direction will be smaller, leading to a increase in MEF. Conversely, smaller ejecta angles result in an increase in x-momentum and hence reduce the efficiency of momentum transfer. In order to conceptualise this, imagine a projectile completely perforating a target as shown in Figure 8.5. The higher the magnitude of downrange x-momentum, the less momentum in the target and the lower the MEF will be. As the ejecta

angle becomes larger, so too does the magnitude of the y-momentum, resulting in higher momentum enhancement factors.

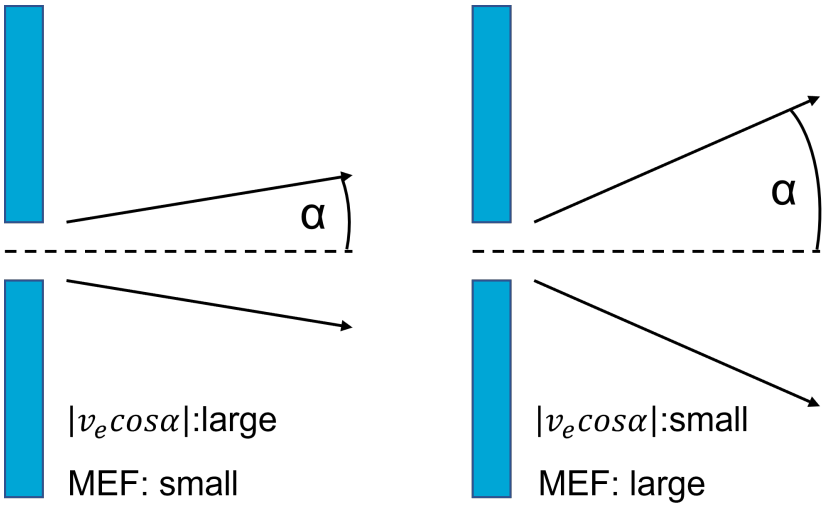

Figure 8.5: Ejecta spread angle and impact on MEF.

This theory is tested by turning now to Figure 8.6 which shows the relationship between normalised ejecta mass and MEF. The steeper the inclination of the line (i.e. the more negative the slope becomes), the more efficient the process of momentum transfer is in terms of ejecta mass. The cylinder shape has the steepest slope, followed by the cone, sphere and punch. This indicates that although the sphere produced more ejecta than the cone, it was slightly less efficient at momentum transfer.

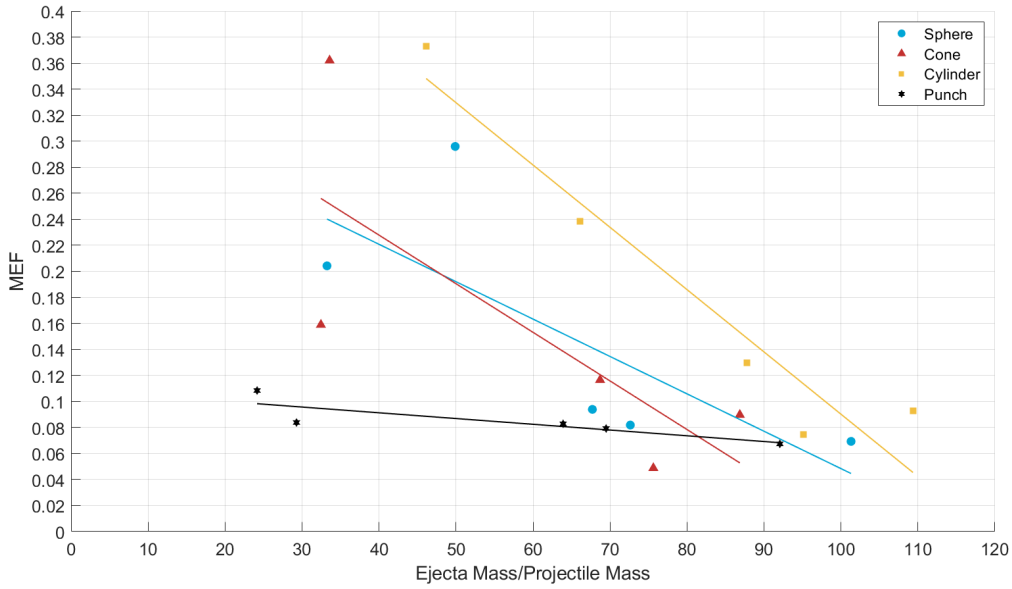

Figure 8.6: Simulated results of Normalised Ejecta Mass vs. Momentum Enhancement Factor (MEF) for a variety of aluminium shapes striking 0.7 *mm* thick glass-glass-aluminium targets.

It can be reasonably assumed that these differences are a consequence of the angle at which ejecta was expelled. Larger angles mean that ejecta will spread more widely and less of the ejectas x-momentum will be considered in the calculation of the MEF.

Figure 8.7 shows the differences in the debris clouds and particularly the ejecta angles for the various projectile shapes. By taking the direction of the average downrange ejecta particle, the sphere shape results in the largest angle, followed by the cylinder, cone and punch shapes as outlined in Table 8.4.

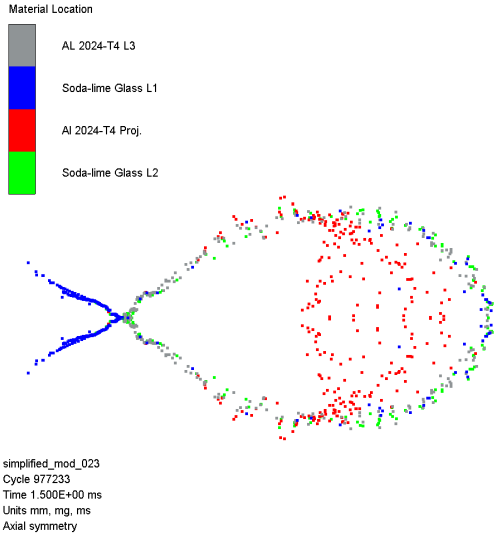

(a) Sphere ejecta angle, Normalised ejecta mass = 101.31, MEF = 0.0691, Angle = 59.11°

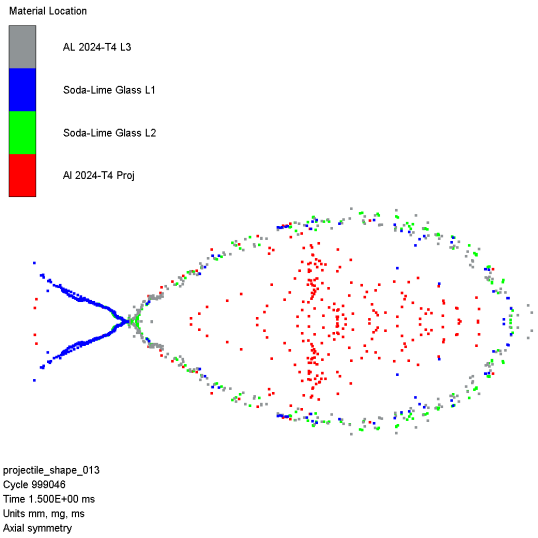

(b) Cone ejecta angle, Normalised ejecta mass = 75.63, MEF = 0.0488, Angle = 58.06°

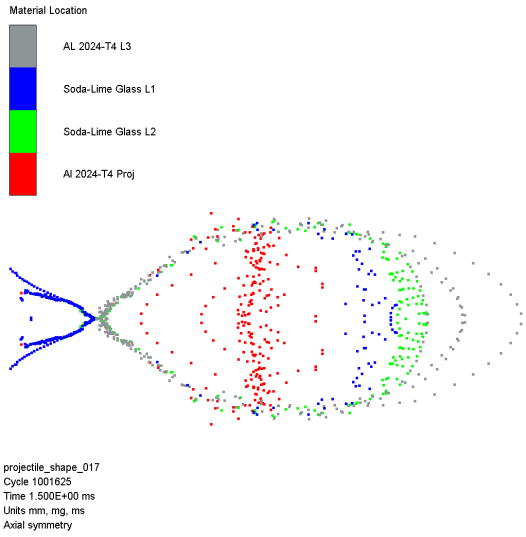

(c) Cylinder ejecta angle, Normalised ejecta mass = 95.10, MEF = 0.0744, Angle = 58.33°

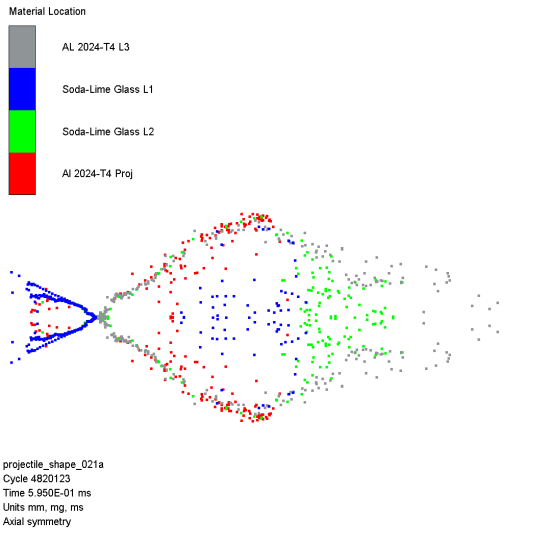

(d) Punch ejecta angle, Normalised ejecta mass = 92.06, MEF = 0.0674, Angle = 57.73°

Figure 8.7: Comparison of ejecta angles for various projectile shapes at $v_p = 14000\ m/s$, $t = 1.5\ ms$.

It stands to reason that for larger angles of ejecta emission, the resulting ejecta velocity in the x-direction will be smaller, leading to a decrease in MEF. The downrange velocity of the various

materials shows some pretty different patterns with projectile shape. The sphere appears to finish with a lot more forward momentum on its fragments, followed by the cone with a little less, then the cylinder. The punch displays a different pattern altogether where it disperses outward at the edges of the debris cone instead of being in the centre of the cloud.

Shape	Ejecta Mass/Projectile Mass	Magnitude (mgm/s)	Angle (°)	MEF
Sphere	101.31	19.83	59.11	0.0691
Cone	75.63	21.13	58.06	0.0488
Cylinder	95.10	20.75	58.33	0.0744
Punch	92.06	23.86	57.73	0.0674

Table 8.4: Comparison of ejecta angles for projectile shapes travelling at 14000 m/s.

8.3. Summary

As we have seen in this chapter, the glass-glass-aluminum target has been subjected to hypervelocity impacts of various projectile shapes. It has been shown that projectiles with more flat or blunt faces like the cylinder and sphere shapes tend to produce larger amounts of ejecta when compared to projectiles with sharper tips and edges like the cone and punch shapes. However, this increase in ejecta mass does not necessarily correspond to larger ejecta momentum. It has been found that certain projectile shapes are more efficient at momentum transfer in terms of ejecta mass. This is due to the angles at which ejecta is expelled from the target. Larger angles of ejecta emission tend to lead to larger MEF values while smaller angles result in smaller MEF values. Overall, the cylinder shape produced the greatest MEF values, followed by the cone, sphere and punch. In terms of debris impacts into satellite solar arrays, these results show that the projectile shape which will induce the least amount of momentum transfer and therefore the preferred shape to minimise changes in satellite direction is the punch. Although not examined in great detail in this thesis, it is the blunt projectiles like cylinders and spheres which generate higher quantities of ejecta and therefore are more detrimental to contributing to the debris environment.

9

Application to Debris Environment Validation

In this chapter, the MEF results are applied to various impacts to determine the resulting transferred momentum. This is applied to a method of predicting changes in a satellites altitude in order to make inferences about the impacting projectile. The goal of this step is to aid in the understanding of how much various impacts can effect a satellites orbit, but to also shed light on how this information can be used in the future to validate the debris environment.

9.1. Predicting Changes in Satellite Altitude

Due to the variance in MEF values for different configurations and initial conditions, it is difficult to understand the impact that this has on real world spacecraft operations. In order to put this all in to context, a system of measuring the change in spacecraft momentum is needed. Williamsen et al. [3] implemented a method whereby they computed the difference in semi major axis (dSMA) in order to make inferences about space debris impact characteristics. The work assumes that the satellite is initially in a circular Keplerian orbit with $r = a$. Following the debris impact, the satellite transitions to an elliptical orbit with a new semi-major axis which is calculated using the the vis-visa equation. This enables the change in satellite orbital velocity to be related to its altitude and is given by Equation 9.1.

$$\Delta v = \sqrt{\frac{\mu}{r}} - \sqrt{\frac{2\mu}{r} - \frac{\mu}{a}} \tag{9.1}$$

Where:

- Δv = the change in orbital velocity of the satellite (km/s)

- μ = Earth's gravitation constant (398600 $km^3 \cdot s^{-2}$)
- r = the original orbital radius in the circular orbit (km)
- a = the new semi-major axis of the orbit following the collision (km)

Knowing the change in orbital velocity, the mass of the projectile can be calculated by using the conservation of momentum given by 9.2.

$$m_p \times v_p \times MEF = M \times \Delta v \tag{9.2}$$

Where:

- m_p = projectile mass (kg)
- v_p = projectile velocity (km/s)
- MEF = momentum enhancement factor
- M = satellite mass (kg)

9.1.1. Unknown MEF Values

Williamsen et al. assume near-normal incidence and illustrate how changes in SMA following a collision with debris may be correlated for each satellite class to the size of the projectiles. In the example they use with the near-polar orbital inclination at 800 km altitude, the relative velocity distribution of debris ranges from 1000-15000 m/s. They use an example with a near-polar inclination and 800 km altitude. Using the same orbital conditions, the predicted changes in SMA or altitude from aluminium sphere debris strikes are presented in Figure 9.5. Figure 9.1a deals with a 1 kg class satellite while Figure 9.1b plots for a 10 kg satellite, both at 14000 m/s and for a range of MEF values.

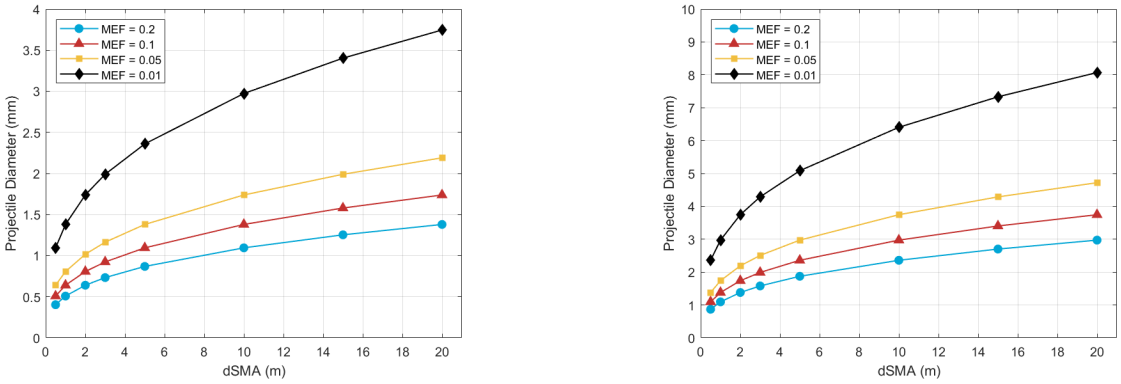

(a) $V = 14000m/s$, $M = 1kg$

(b) $V = 14000m/s$, $M = 10kg$

Figure 9.1: Inferred Aluminium Sphere Projectile Diameter vs. Observed dSMA for 14000 m/s impact.

Using the same MEF values, Figure 9.5a presents the data for a 2000 m/s impact. The plots show that at lower impact velocities, larger projectiles are required at in order to achieve the same dSMA values as higher velocities.

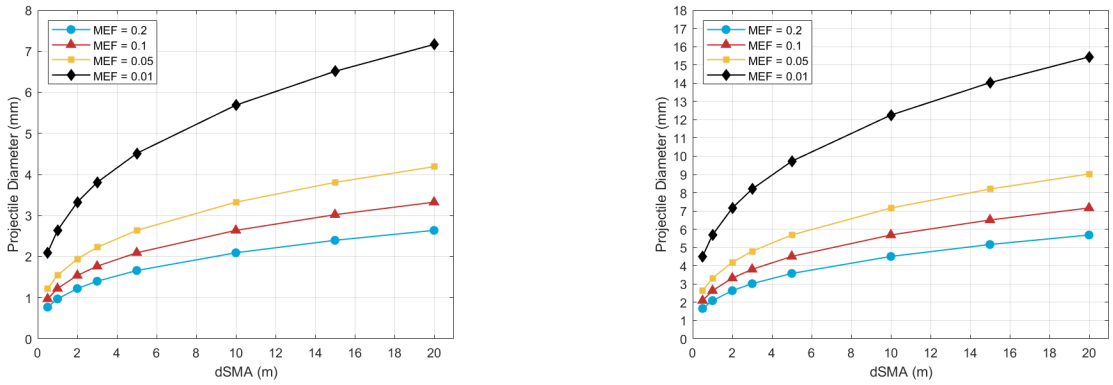

(a) $V = 2000m/s$, $M = 1kg$ **(b)** $V = 2000m/s$, $M = 10kg$

Figure 9.2: Inferred Aluminium Sphere Projectile Diameter vs. Observed dSMA for 2000 m/s impact.

Clearly the mass of the satellite, MEF value, and the change in semi-major axis all play an important role in determining the size of the detected projectile. The lower the MEF becomes, the less momentum that is transferred to the target and hence the more difficult it is for the satellites orbit to be changed. This is a noteworthy point to consider in terms of solar array construction seeing as it is might be preferred to keep the MEF as low as possible. If future solar arrays can be designed in such a way as to minimise the MEF resulting from impacts while maintaining the structural integrity of the array, it would mean less orbital adjustments over the satellites lifetime. From a debris environment validation standpoint however, it might be more advantageous to have slightly larger MEF values so that more momentum transfer occurs, making it easier to detect dSMA. Smaller orbital changes might be a lot more difficult to detect as opposed to changes in the tens of metres depending on the accuracy of the detection equipment. Larger satellites have the capability of carrying more mass and better GPS systems as opposed to smaller ones. Due to their increased mass however, larger satellites wont experience as much of a change in SMA when compared to a smaller satellite for a given impact, making the smaller sized projectiles even more difficult to detect. Its worth bearing in mind that a 1 kg satellite wont know its orbit well enough to do this kind of detection (or be capable of doing missions where this kind of orbit accuracy matters). A larger dSMA is easier to detect to get measurements of the in situ debris population. Large satellites with very thin Hubble-style arrays might be less useful for detecting orbit perturbations due to the low MEF values, but satellites with slightly thicker arrays might be more useful.

9.1.2. Known MEF Values

The previous section dealt with predicting changes in a satellites altitude from debris strikes into defined satellite classes for a range of MEF values. The advantage of undertaking HVI simulations is that the MEF values for a range of different projectile and target conditions are now roughly known. This enables us to multiply the projectile momentum by the MEF value and determine the actual momentum transferred for that given impact scenario. By doing so, the change in orbital velocity can be computed and substituted into Equation 9.1, leaving the expected change in SMA. As spacecraft operators can detect changes in SMA, it means that the change in momentum can be correlated to a narrowed set of potential impacts and cross-referenced with debris models.

Rearranging Equation 9.2 to solve for Δv yields the following:

$$\Delta v = \frac{m_p \times v_p \times MEF}{M} \tag{9.3}$$

From reviewing Equation 9.3, its clear that for constant satellite mass the projectiles momentum multiplied by the MEF is the driving factor behind the change in orbital velocity. This term is known as the transferred momentum and unfortunately the individual components of $m_p \times v_p \times MEF$ cannot currently be individually determined when debris strikes a satellite. This term is plotted on the y-axis in Figure 9.3.

In the example Williamsen et al. use with the near-polar orbital inclination at 800 km altitude, the relative velocity distribution of debris ranges from 1000-15000 m/s. Using the data obtained from this study, which used velocities of 2000-14000 m/s, a scatter plot can be created plotting the relationship between projectile momentum and transferred momentum. Regions can be created which show the minimum and maximum expected projectile momentum values that result from the transferred momentum. Using the transferred momentum value, it could be determined from the graph with a degree of estimation, what the projectile momentum was and possibly the projectile size regime.

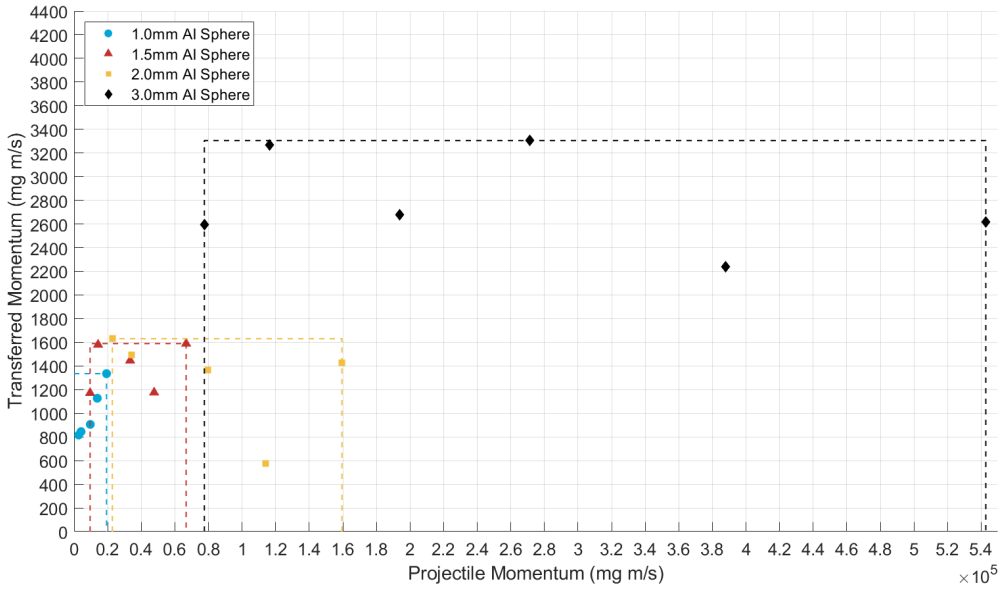

Figure 9.3: Simulated results of Projectile Momentum vs. Transferred Momentum for aluminium spheres of 1.0, 1.5 & 2.0 mm diameter striking 0.7 mm thick glass-glass-aluminium targets.

In certain areas of Figure 9.3, the data points representing the different projectile diameters overlap or come very close to each other. These areas indicate that certain impact scenarios are indistinguishable from one another in terms of absolute momentum transferred. This means that for example if the change in orbital velocity relates to a transfer momentum value of $\sim$ 1150 mgm/s, it is very difficult from this method alone to determine whether the impact came from a 1 mm or 1.5 mm projectile diameter travelling at 10000 m/s. Similarly, depending on how accurate measurements are, it would be very difficult to distinguish between a 1.5 mm travelling at 7000 m/s and 2.0 mm projectile diameter travelling at 3000 m/s as both yield very similar transfer momentum values of around 1500 mgm/s. That being said, some velocities are much more likely to occur in LEO, with the average collision velocity being around 10000 m/s [106]. Looking at the specific example of the near-polar orbital inclination at 800 km altitude in Figure 9.4, its clear that a debris impact with a velocity of 14000 m/s is much more likely to occur. By looking at a larger data set of impacts across a constellation and taking what is known about the velocity distribution, it might be possible to do some statistical analysis involving maximum likelihood estimation to draw conclusions about the mass distribution of the debris. The uncertainty in that parameter is likely a significant issue with current risk modelling.

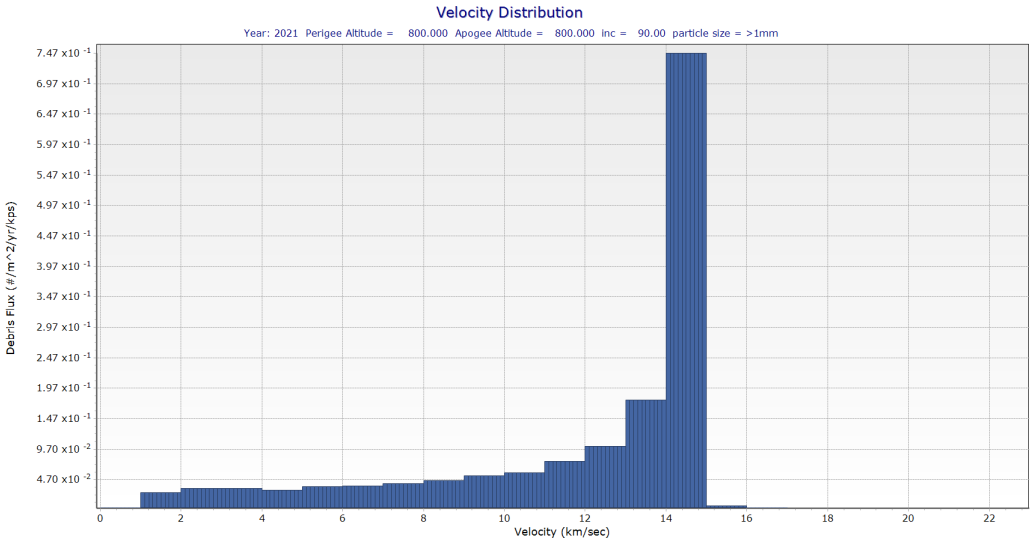

Figure 9.4: Velocity vs. Debris Flux for Low Earth Orbit (altitude = 800 km, inclination = 90°) in 2021.

Using the MEF values obtained for different projectiles, the associated change in SMA can be calculated for various impacts. Figure 9.5a highlights that the expected dSMA for a 3.0 mm projectile impacting satellites of different mass at 2000 m/s is going to be the highest followed by the 2.0, 1.5 and 1.0 mm projectiles. Figure 9.5b then shows how for a 14000 m/s impact, the 1.5 mm will actually induce a higher change in SMA than the 2.0 mm projectile, meaning that it will transfer more momentum at this particular velocity.

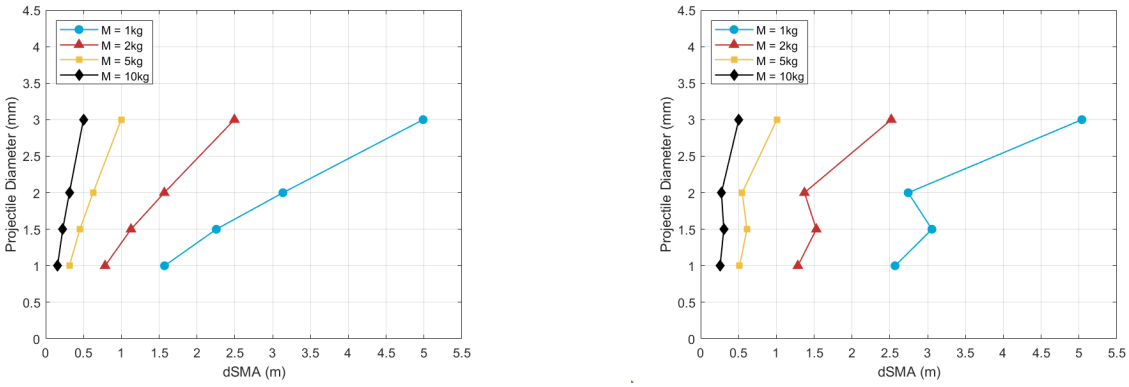

(a) $V = 2000m/s$ **(b)** $V = 14000m/s$

Figure 9.5: Simulated results for Change in Semi-Major Axis vs. Projectile Diameter for a range of different satellite masses.

These results can be explored by looking at Figure 9.6 and seeing that at 2000 m/s, the 3.0 mm projectile does indeed transfer more momentum than the 1.0, 1.5 & 2.0 mm projectiles. As velocity increases however, some incredibly intriguing behaviour of particular interest unfolds. There does not seem to be any clear, discernible tendency among the data points except for

the fact that the 3.0 *mm* projectile seems to be the most efficient at transferring its initial momentum to the target. This almost seems counter intuitive as it was concluded previously that the lower momentum projectiles result in higher MEF values. However, it is the product of projectile momentum and MEF that results in the transferred momentum and from these graphs, its clear that the 3.0 *mm* projectile yields the most optimum momentum transfer. This implies that of the four diameters simulated in this study, the 3.0 *mm* poses the biggest threat to this specific satellite solar array configuration in terms of momentum transfer. It is worth mentioning that solar arrays with different structural and material composition, like those used for EURECA, might see a different size that maximises momentum transfer in accordance with its different ballistic limit.

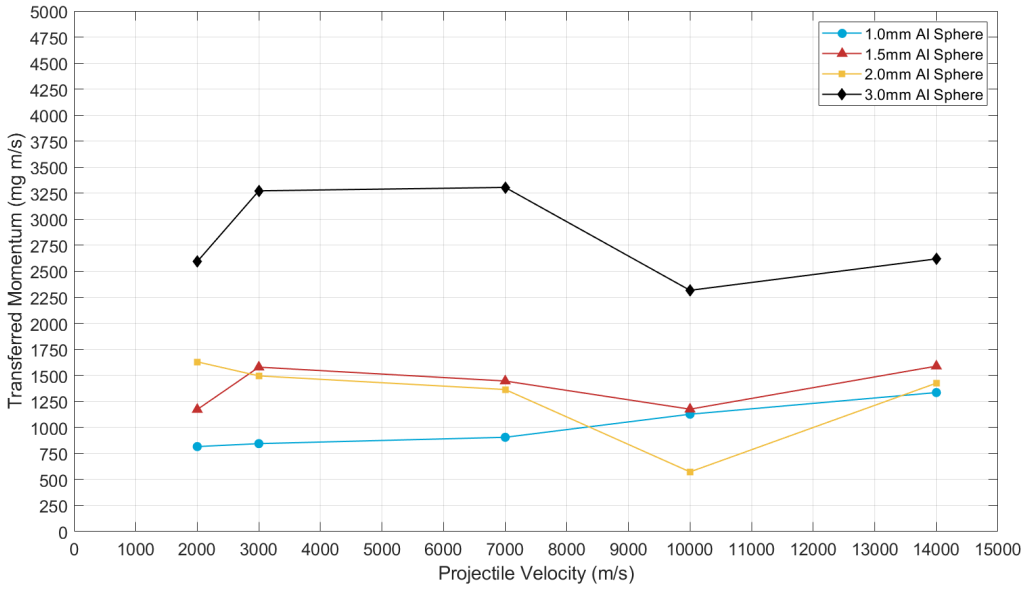

Figure 9.6: Simulated results of Projectile Velocity vs. Transferred Momentum for aluminium spheres of 1.0, 1.5, 2.0 & 3.0 *mm* diameter striking 0.7 *mm* thick glass-glass-aluminium targets.

Although the above plot provides some initial food for thought, it suffers from the assumption that all debris objects are going to be aluminium spheres. In the real world, debris objects are more likely going to be irregular in shape from the fragmentation events they have encountered. They are also going to be made up from a whole host of different materials which will influence the MEF in various ways. Figure 9.7 presents an amalgamation of various HVI simulations which have been conducted throughout this work. The blue markers represent the 1.0 *mm* sized projectiles or the shapes which were formed from the equivalent volume of a 1.0 *mm* sphere, the red markers represent the 1.5 *mm*, followed by yellow for 2.0 *mm* and black for 3.0 *mm* diameter spheres. A lot of the markers are clustered together, particularly the blue, red and yellow ones. This highlights that for particular impact velocities, the transferred momentum value of different projectile types will be very close due to the variability in MEF. For example, at 10000 m/s the 2.0 *mm* aluminium sphere will impart less momentum than the 1.5 *mm* glass

sphere. By the same token, at 14000 m/s the 2.0 mm aluminum sphere punch transfers less momentum than the punch. These findings conclude that MEF is extremely important in the process of momentum transfer and that different combinations of projectile size/material/shape influence momentum transfer differently.

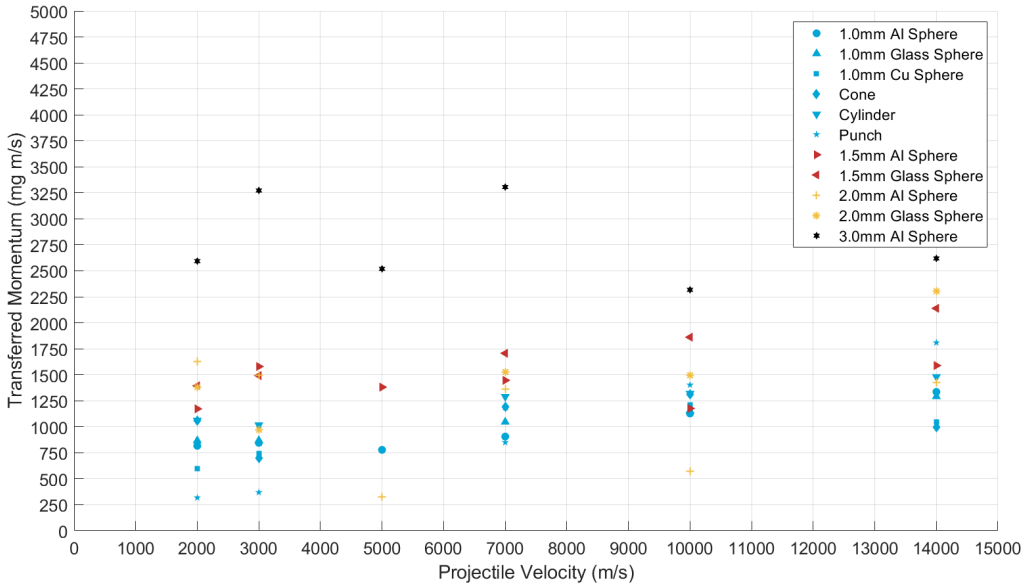

Figure 9.7: Simulated results of Projectile Velocity vs. Transferred Momentum for a range of projectile sizes, materials and shapes striking 0.7 mm thick glass-glass-aluminium targets.

From the findings of this study, it is now possible to understand the variance in MEF values that result from specific impacts into satellite solar arrays. This, along with data obtained from orbital debris models, allows for better estimations of the size and velocity of the projectiles that impact solar arrays. An important consideration, albeit unsatisfying, is that the transferred momentum is not necessarily a good indicator of projectile momentum due to variabilities in MEF under different impact scenarios.

10

Conclusions and Recommendations

The following chapter contains the main conclusions which can be drawn from this thesis work as well as recommendations for future work. Section 10.1 answers the original research questions from Chapter 1 and highlights the most relevant results. Section 10.2 outlines some proposals for subsequent work which can build on the achievements of this thesis.

10.1. Conclusions

In this thesis, an investigation was undertaken to determine the MEF values associated with hypervelocity impacts into spacecraft solar arrays. The following section outlines the conclusions that were made based on the initial research questions.

1. **To what extent can a typical spacecraft solar panel be modelled using hydrocode?**
   Due to the variety of solar panel configurations available, both the composition and thickness of the different layers play an important role in modelling a typical solar panel. The more numerous and thin the layers are, the more computational power is required due to the significantly smaller SPH particle packing size needed to fill these thin spaces and obtain accurate results. In addition to this, a whole range of material models is needed in order to successfully replicate the behaviour of real-life materials. Due to these constraints, this thesis focussed on creating a simplified model which used commonly validated materials such as glass and aluminium. To this extent, a solar panel can be successfully modelled using hydrocode.

(a) **Is a simplified model a sufficient replacement for a more complex multi-material composition design?**
Comparing simulated to real-life tests in Figures 3.3 and 3.4, the conchoidal fracturing is very similar in both. However, comparing Figures 5.8 and 5.9, it can be seen that the simplification of modelling the solar panel multi-layer substrate as a single aluminium layer means that delamination behaviour is not observed. Although the aluminium layer did not delaminate, it displayed the same lipped shape feature as the real-life impact and is a good indication that the simplified model performs well in replicating experimental behaviour. The objective of simplifying the solar panel was to create a model which drastically cut down on computation time and also use the materials which could be validated. This enabled useful trends and general conclusions to be drawn for a thin solar panel-like structure where complete perforation occurs.

2. **How effectively can the momentum transfer from a hypervelocity impact to a solar panel be modelled?**
Overall very well. At the heart of momentum transfer is the MEF and modelling techniques like SPH make it possible to obtain these values. In addition to this, being able to use numerical analysis tools like ANSYS Autodyn enables velocities in the hypervelocity regime to be simulated which otherwise would not be possible by conventional experimental means. The ability to extract ejecta momentum data is the most important factor to consider when selecting a software tool. In this case a user subroutine was designed to cater for this. This enabled the MEF values to be calculated for a whole host of different impact scenarios and subsequently the magnitude of transferred momentum.

   (a) **What is the typical range of MEF values that result from a 1-3 mm size spherical projectile impacting a simplified solar panel target at hypervelocities?**
   The results obtained in Chapter 6 revealed that within the 2000 - 14000 m/s range, the MEF varies from between 0.0048 to 0.2958 for 1-3 mm spherical aluminium projectiles. Inside these size and velocity ranges, the smaller and slower the projectile, the larger the MEF. There is a bigger difference between smaller and larger projectiles at lower velocities, however, once the projectiles breach around the 7000 m/s point, they enter into the melt/vaporisation range and this is where the projectiles become substantially melted and where we see the MEF tending the plateau.

   (b) **How does the projectile size and material effect the MEF?**
   When complete perforation occurs at a given velocity, smaller projectiles will have larger MEFs due to the higher percentage of momentum transferred to the target. This is due to the characteristics of the ejecta - the more back-scattered ejecta momentum there is and the slower the downrange ejecta becomes means that even though you start with less momentum, a much larger percentage of that momentum gets transferred to the target. When momentum is held constant, projectile size has little effect on MEF. This means that a 1.0 mm diameter projectile travelling at 21,728 m/s will transfer roughly the same percentage of its initial momentum as

a 2.0 mm projectile travelling at 2,634 m/s. Chapter 7 has shown that material is another factor which can heavily influence MEF. For this particular study, low-density materials like glass and aluminium lead to much larger MEF values than higher-density materials such as copper. This is a result of an increase in initial projectile momentum which has been shown to reduce MEF where complete perforation occurs.

(c) **What influence does the target composition have on MEF?**
By changing the second glass layer to the proposed silicon model, it was found that the target produces less ejecta mass than the previously simulated glass-glass-aluminium target. This implies that the silicon material used has a higher resistance under hypervelocity impact than the glass. Interestingly, the lower quantity of ejecta mass doesnt correspond to an increase in MEF. On account of the fact that MEF tends to decrease as ejecta mass generation increases, it was expected that the MEF values for the glass-silicon-aluminium target would be higher. This is not the case however. The general tendency of MEF values for the glass-silicon-aluminium target are below those of the glass-glass-aluminium target. This underlines that although more ejecta mass may be produced, it does not necessarily mean that less momentum will be transferred to the target. Due to the fact that more of the silicon is intact, less material was ejected and hence a higher proportion of the projectile momentum had to be transferred to less material.

(d) **What are the effects of using various projectile shapes on both ejecta mass and MEF?**
Chapter 8 revealed that for the same initial projectile momentum value, the MEF of the cylinder shape was maximal, followed by the cone, sphere, and finally punch. Interestingly however, even though the cone shape has higher MEF values than the sphere, it is the latter which generates more ejecta. The blunt shape of the sphere and cylinder projectiles enable them to have more surface area contact upon impact and therefore produce slightly more debris than the cone and punch shapes. The sharper tips on these projectiles make them easier to deform and result in smaller crater sizes. In addition to this, the punch shape shows very similar results in terms of generated ejecta compared to the other shapes, but much lower MEF values. This demonstrates that the influence of ejecta mass on momentum transfer varies from shape to shape. Because each shape has the same projectile momentum, it can be reasonably assumed that these differences are a consequence of the angle at which ejecta was expelled. Larger angles mean that ejecta will spread more widely and less of the ejectas x-momentum will be considered in the calculation of the MEF.

(e) **How does a normal vs. oblique incidence impact effect the ejecta and therefore momentum transfer?**
Unfortunately this sub-question cannot be answered because Autodyn 2D was used used which doesn't allow impact angle to be changed. This decision was made in order to increase computational efficiency so that a broader range of studies and analysis could be done.

3. **Can MEF results be applied to space debris environment validation?**
The findings of this work imply that there will be difficulties here because imparted momentum can map to a whole range of different projectile scenarios thanks to MEF variations. With a large enough data set and well-characterised MEF relationships it could be done.

(a) **Is it possible to determine the size of an impacting projectile due to changes in a spacecrafts semi-major axis?**
It is possible to make inferences about the size of a projectile due to change in SMA for a given MEF but no concrete conclusion. A lot depends on the MEF values selected, the mass of the satellite and the amount of change in semi-major axis detected. MEF variation with shape and momentum means that this mapping will need a substantial bit of data before useful conclusions can be drawn.

(b) **Can simulated MEF values, aided by satellite perturbation data, be used in order to characterize debris strikes?**
Referring back to Figure 9.6, its clear that a given transferred momentum can map to a whole range of mass/velocity/shape combinations. The consequences of this are that it becomes extremely difficult to distinguish between impact types. Analysing the debris velocity distributions can help to narrow in on potential suspecting collision parameters but a larger data set of multiple impacts would be required in order to start drawing useful conclusions about debris characteristics. Since prior work has completely disregarded solar arrays, this work's contribution is to show that solar array impacts can impart detectable momentum even if they break through and thus need to be taken into account, not ignored. There are multiple factors (size, shape, material) that can influence MEF and transferred momentum. Although measuring the transferred momentum doesn't map to a specific deterministic projectile parameters, with good MEF modeling you can figure out what family of projectiles/velocities could have produced that effect, and use other data (DebriSat, etc) to start using in situ data to draw conclusions about mass distributions for debris, and from that learn more about satellite risks. There's some tendency in academia to blow off debris risks because the models are clearly over-conservative, and we need to do better in order to motivate actions to protect the space environment. This research is a step in the right direction by reducing the very coarse MEF assumptions used in prior work to start refining those and reduce the uncertainties in using in situ perturbation data to validate debris environment models.

In conclusion, this work aims to act as a stepping stone in reducing the assumptions required for assessing perturbations in the context of debris environment modeling. The 1-3 mm debris range remains as an interpolated region in many statistical debris models used today. Understanding how solar panels react to impact in the context of momentum transfer is mostly driven by the MEF which until now has been unknown.

10.2. Recommendations

As with any research undertaken, there will always be areas for improvement and further exploration. This final chapter outlines some potential future work that would significantly improve the knowledge surrounding momentum transfer.

First of all, as was pointed out in Section 2.5, the non-existence of MEF data for solar panels available in literature means that all of this work is based on proposed and simplified models. Of course, the constitutive materials used in these models have been validated, but unless experimental studies are carried out the exact MEF values will remain unknown. Great work is currently been done by PhD researcher Anne Bennett of the Autonomous Vehicles Systems Laboratory at the University of Colorado Boulder to identify debris strikes in spacecraft telemetry. There is interest in conducting a series of hypervelocity impact tests using solar array samples which would serve to compliment studies like Anne's and validate the work of this thesis.

One area where a lot of work was done around was implementing CFRP Aluminium Honeycomb sandwich panels into Autodyn. This modern, state-of-the-art aerospace structure is very common nowadays and used in the construction of many different solar panel configurations. A lot of time was spent gathering the material models and running simulations only to find that the complex behaviour of orthotropic materials like CFRP required substantial amounts of computational effort. Figure 10.1 presents an example with CFRP sandwich panels connected by Al 5056 honeycomb struts, which was the closest structure to honeycomb that could be simulated using Autodyn 2D. This simulation took roughly 140 hours to complete and did not even contain any additional layers like the coverglass or solar cell which would have only further increased simulation time. Determining the MEF values associated with CFRP AL HC sandwich panels, either experimentally or numerically, has not yet been done before and would certainly be very beneficial.

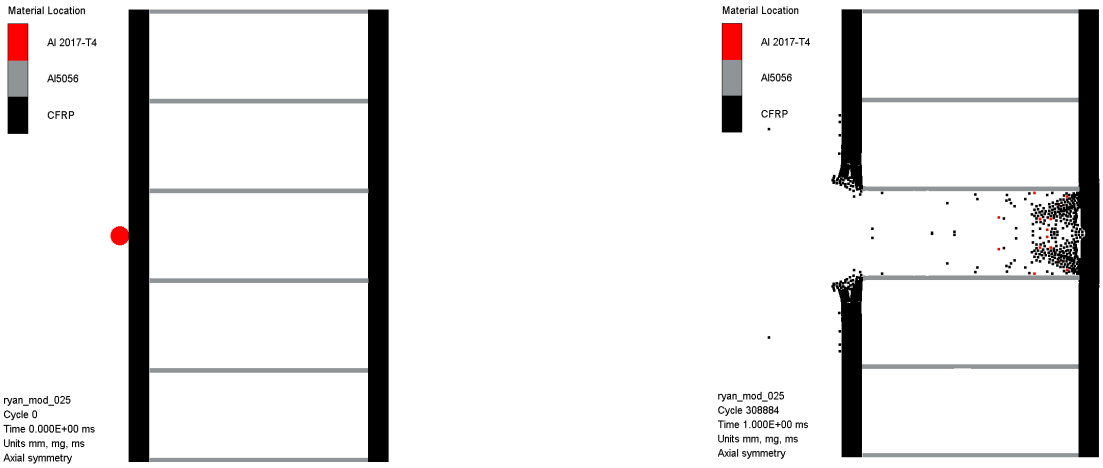

(a) Pre-impact **(b)** Post-impact

Figure 10.1: CFRP Aluminium Honeycomb Sandwich Panels modelled in Autodyn.

Figure 10.2 presents a simplified EURECA solar panel which was impacted by a 1 mm aluminium spherical projectile travelling at 10000 m/s. This was done in order to try and determine an approximate value for MEF for this particular system. Interestingly, the MEF value obtained was 0.45. Compare this to the simplified HST solar panel for the same impact conditions where the MEF was 0.08, its clear that the thicker panel with CFRP Al HC drastically increases MEF. Lower velocities will only increase the MEF further and this observation is of significant importance so far as detecting strikes go. A panel which results in higher transferred momentum will induce a much larger perturbation and will be easier to detect. This has the potential to make it easier to determine the parameters of the colliding projectile and draw clearer conclusions. This initial result warrants further investigation into modelling more resistive solar panel configurations which will help to better validate the debris environment.

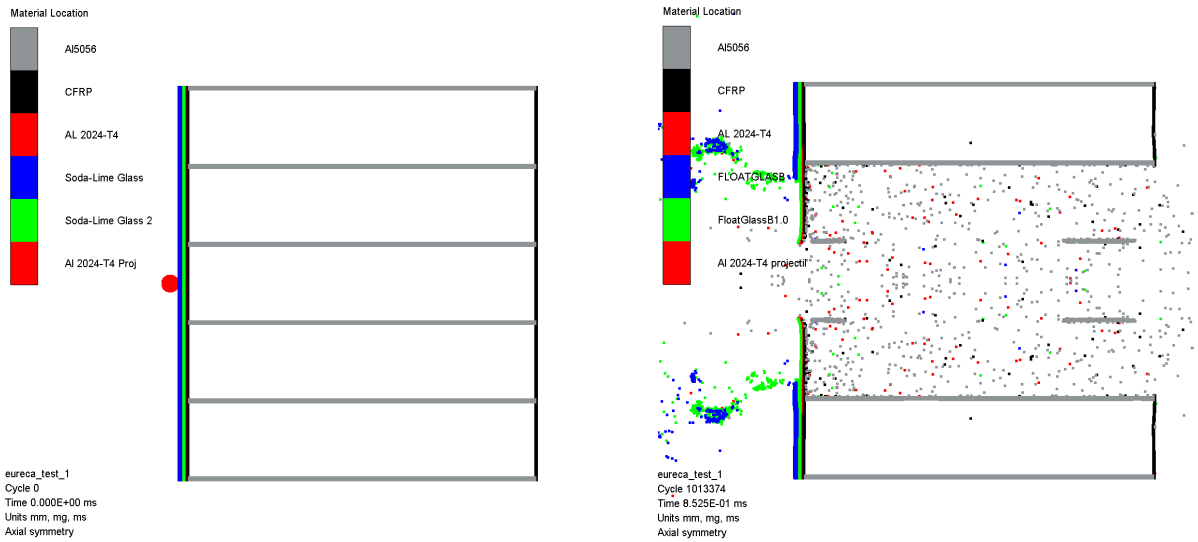

(a) Pre-impact **(b)** Post-impact

Figure 10.2: Simplified EURECA solar panel impacted by an aluminium spherical projectile at 10000 m/s, MEF = 0.45.

Another interesting study would be to develop a material model for silicon and incorporate it into the solar panel model. The assumptions made around simplifying the solar panel model mean that it would be worthwhile investigating further or even validate using a a real HST solar array. If any HVI testing is conducted for validation purposes in the future, I would recommend the following tests:

1. MEF measurement for 1-3 mm Al 2024-T4 spherical projectiles impacting HST solar cell samples at velocities up to the maximum capability of the test equipment.
2. Select a variety of other projectile materials which are representative of debris materials, like copper, CFRP and glass and record MEF values.
3. Investigate how MEF changes when solar panels with CFRP Al HC are used.

Additionally, if any further simulations are being conducted in the future (depending on whether the computer has the capabilities of handling them) I would recommend the following simulations:

1. Modelling EURECA solar panels (which contain CFRP Al HC sandwich panels) with the same impact conditions used in this thesis.
2. Use 3D models to simulate more irregular projectile shapes which are more akin to real debris objects.

References

[1] "Space environment statistics - space debris user portal." (Accessed on 03/10/2021). ().

[2] B. Bastida Virgili, J. C. Dolado, H. G. Lewis, *et al.*, "Risk to space sustainability from large constellations of satellites," *Acta Astronautica*, vol. 126, pp. 154–162, Sep. 2016, ISSN: 0094-5765. DOI: 10.1016/J.ACTAASTRO.2016.03.034.

[3] J. Williamsen, D. Pechkis, A. Balakrishnan, and S. Ouellette, "Improving Orbital Debris Environment Predictions Through Examining Satellite Movement Data," 2020. DOI: 10.2514/1.A34765.

[4] V. V. Adushkin, O. Y. Aksenov, S. S. Veniaminov, S. I. Kozlov, and V. V. Tyurenkova, "The small orbital debris population and its impact on space activities and ecological safety," *Acta Astronautica*, vol. 176, no. January, pp. 591–597, 2020, ISSN: 00945765. DOI: 10.1016/j.actaastro.2020.01.015.

[5] A. Aryadne, B. A, H. Schaub, and R. Carpenter, "Assessing Debris Strikes in Spacecraft Telemetry: Development and Comparison of Various Techniques," Tech. Rep., 2019, pp. 21–25.

[6] W. Ley, K. Wittmann, and W. Hallmann, *Handbook of Space Technology*. 2009, pp. 1–883, ISBN: 9780470697399. DOI: 10.1002/9780470742433.

[7] "Space debris - evolution in pictures." (), [Online]. Available: https://www.esa.int/About_Us/ESOC/Space_debris_-_evolution_in_pictures (visited on 08/11/2021).

[8] R. D. Culp, *Orbital debris*. 1991, vol. 74, pp. 629–647, ISBN: 087703334X. DOI: 10.17226/4765.

[9] P. H. Krisko, "The predicted growth of the low-Earth orbit space debris environment - An assessment of future risk for spacecraft," *Proceedings of the Institution of Mechanical Engineers, Part G: Journal of Aerospace Engineering*, vol. 221, no. 6, pp. 975–985, 2007, ISSN: 09544100. DOI: 10.1243/09544100JAERO192.

[10] A. Murtaza, S. J. H. Pirzada, T. Xu, and L. Jianwei, "Orbital Debris Threat for Space Sustainability and Way Forward (Review Article)," *IEEE Access*, vol. 8, pp. 61 000–61 019, 2020, ISSN: 21693536. DOI: 10.1109/ACCESS.2020.2979505.

[11] A. A. Bennett and H. Schaub, "Identifying and Assessing Debris Strikes in NASA Spacecraft Telemetry," Tech. Rep.

[12] J. R. Shell, "Optimizing orbital debris monitoring with optical telescopes," Tech. Rep.

[13] J. Koning, G. va Uffelen, A. Zemanek, and B. Zemanek, *Technical description*, 0. 2017, vol. 49, pp. 22–27, ISBN: 2002210780. DOI: 10.1163/9789004278004{_}005.

[14] N. L. Johnson, P. H. Krisko, J. C. Liou, and P. D. Anz-Meador, "NASA's new breakup model of EVOLVE 4.0," *Advances in Space Research*, vol. 28, no. 9, pp. 1377–1384, 2001, ISSN: 02731177. DOI: 10.1016/S0273-1177(01)00423-9.

[15] J. C. Liou, N. L. Johnson, P. H. Krisko, and P. D. Anz-Meador, "The new NASA orbital debris breakup model," *COSPAR Colloquia Series*, vol. 15, no. C, pp. 363–367, 2002, ISSN: 09642749. DOI: 10.1016/S0964-2749(02)80367-5.

[16] D. J. Kessler, N. L. Johnson, and M. Matney, "The Kessler Syndrome: Implicatinos to Future Space Operation," *33rd Annual AAS Guidance and Control Conference*, pp. 10–016, 2010.

[17] G. Drolshagen, "Impact effects from small size meteoroids and space debris," *Advances in Space Research*, vol. 41, no. 7, pp. 1123–1131, 2008, ISSN: 02731177. DOI: 10.1016/j.asr.2007.09.007.

[18] L. B. Sagnières and I. Sharf, "Stochastic modeling of hypervelocity impacts in attitude propagation of space debris," *Advances in Space Research*, vol. 59, no. 4, pp. 1128–1143, 2017, ISSN: 18791948. DOI: 10.1016/j.asr.2016.11.030.

[19] J. B. WHITE, "Meteoric Effects on Attitude Control of Space Vehicles," *ARS Journal*, vol. 32, no. 1, pp. 75–78, 1962. DOI: 10.2514/8.5951.

[20] G. P. Anshakov, A. I. Belousov, A. V. Sedelnikov, and A. S. Gorozhankina, "The micrometheroid influence estimate on the microaccelerations level onboard small spacecraft," *Journal of Physics: Conference Series*, vol. 1210, no. 1, 2019, ISSN: 17426596. DOI: 10.1088/1742-6596/1210/1/012002.

[21] A. Francesconi, "Characterization of Ejecta From Hvi on Spacecraft Outer Surfaces," *Iadc-11-05*, no. April, pp. 1–77, 2013.

[22] M. Rival and J. Mandeville, "Modeling of Ejecta Produced upon Hypervelocity Impacts," *Space Debris*, vol. 1, no. 1, pp. 45–57, 1999, ISSN: 1388-3828. DOI: 10.1023/A:1010021403591.

[23] E. Schneider and A. Stilp, *Meteroid/debris simulation at Ernst-Mach-Institut (EMI) - Experimental Methods and Recent Results* -, 1993.

[24] A. M. Vickery, *The Theory of Jetting: Application to the Origin of Tektites*, 1993. DOI: 10.1006/icar.1993.1140.

[25] M. Rival, J. C. Mandeville, and C. Durin, "Impact phenomena on brittle materials: Analysis of 1 μM to 1 MM impact features on solar arrays," *Advances in Space Research*, vol. 20, no. 8, pp. 1451–1456, 1997, ISSN: 02731177. DOI: 10.1016/S0273-1177(97)00415-8.

[26] A. F. Cheng, A. M. Stickle, E. G. Fahnestock, *et al.*, "DART mission determination of momentum transfer: Model of ejecta plume observations," *Icarus*, vol. 352, no. November 2019, p. 113 989, 2020, ISSN: 10902643. DOI: 10.1016/j.icarus.2020.113989.

[27] D. Risquez, F. van Leeuwen, and A. G. Brown, "Dynamical attitude model for Gaia," *Experimental Astronomy*, vol. 34, no. 3, pp. 669–703, 2012, ISSN: 09226435. DOI: 10.1007/s10686-012-9310-5.

[28] W. M. Alexander and J. A. McDonnell, "Hypervelocity impact on the GIOTTO Halley Mission dust shield: Momentum exchange and measurement," *Advances in Space Research*, vol. 2, no. 12, pp. 185–187, 1982, ISSN: 02731177. DOI: 10.1016/0273-1177(82)90305-2.

[29] M. Ikeda, M. Tanaka, D. Yokoo, T. Koura, and Y. Akahoshi, "Study of the Effects of Projectile Shape in the Asteroid Orbit Change by Spacecraft Impact," *Procedia Engineering*, vol. 204, pp. 138–145, 2017, ISSN: 18777058. DOI: 10.1016/j.proeng.2017.09.766.

[30] T. Hoerth, F. Schäfer, J. Hupfer, O. Millon, and M. Wickert, "Momentum transfer in hypervelocity impact experiments on rock targets," *Procedia Engineering*, vol. 103, pp. 197–204, 2015, ISSN: 18777058. DOI: 10.1016/j.proeng.2015.04.027.

[31] J. D. Walker and S. Chocron, "Momentum enhancement in hypervelocity impact," *International Journal of Impact Engineering*, vol. 38, no. 6, A1–A7, 2011, ISSN: 0734743X. DOI: 10.1016/j.ijimpeng.2010.10.026.

[32] G. J. Flynn, D. D. Durda, M. J. Molesky, *et al.*, "Momentum transfer in hypervelocity cratering of meteorites and meteorite analogs: Implications for orbital evolution and kinetic impact deflection of asteroids," *International Journal of Impact Engineering*, vol. 136, no. June 2019, p. 103 437, 2020, ISSN: 0734743X. DOI: 10.1016/j.ijimpeng.2019.103437.

[33] K. A. Holsapple and K. R. Housen, "Momentum transfer in asteroid impacts. I. Theory and scaling," *Icarus*, vol. 221, no. 2, pp. 875–887, 2012, ISSN: 00191035. DOI: 10.1016/j.icarus.2012.09.022.

[34] J. D. Walker, S. Chocron, D. J. Grosch, D. D. Durda, and K. R. Housen, "Momentum enhancement due to hypervelocity impacts into pumice," *Procedia Engineering*, vol. 204, pp. 130–137, 2017, ISSN: 18777058. DOI: 10.1016/j.proeng.2017.09.765.

[35] /. Mcdonnell, "Investigation of Energy Partitioning in Hypervelocity Impacts Final Report,"

[36] J. Williamsen and S. Evans, "ScienceDirect ScienceDirect Orbital debris momentum transfer in satellite shields following hypervelocity impact , and its application to environment validation," *Procedia Engineering*, vol. 204, pp. 500–507, 2017, ISSN: 1877-7058. DOI: 10.1016/j.proeng.2017.09.747.

[37] R. H. C. Moir, "Introduction and Overview of Hydrocodes for Impact Cratering Modeling,"

[38] M. Schimmerohn, P. Matura, E. Watson, *et al.*, "Numerical investigation on the standard catastrophic breakup criteria," *Acta Astronautica*, vol. 178, no. September 2020, pp. 265–271, 2021, ISSN: 00945765. DOI: 10.1016/j.actaastro.2020.09.014.

[39] J. a. Zukas, *Introduction to Hydrocodes*. 2004, vol. 49, pp. 279–310, ISBN: 9780080443485.

[40] H.Klinkrad, *Space Debris - Models and Risk Analysis*. 2006, ISBN: 354025448X.

[41] S. Hiermaier, *Structures Under Crash and Impact*. 2008, ISBN: 9780387738628. DOI: 10.1007/978-0-387-73863-5.

[42] M. B. Liu and G. R. Liu, *Smoothed particle hydrodynamics (SPH): An overview and recent developments*, 1. 2010, vol. 17, pp. 25–76, ISBN: 1183101090. DOI: 10.1007/s11831-010-9040-7.

[43] S. Zhang, "Detonation and its applications," 1976.

[44] J. Zukas, *High Velocity Impact Dynamics*, 1990.

[45] S. Ma, X. Zhang, and X. M. Qiu, "Comparison study of MPM and SPH in modeling hypervelocity impact problems," *International Journal of Impact Engineering*, vol. 36, no. 2, pp. 272–282, 2009, ISSN: 0734743X. DOI: 10.1016/j.ijimpeng.2008.07.001.

[46] K. Wen, X. w. Chen, and Y. g. Lu, "Research and development on hypervelocity impact protection using Whipple shield: An overview," *Defence Technology*, no. xxxx, 2020, ISSN: 22149147. DOI: 10.1016/j.dt.2020.11.005.

[47] L. Lucy, "A numerical approach to the testing of the fission hypothesis," *The Astronomical Journal*, vol. 82, no. 12, pp. 1013–1024, 1977, ISSN: 0949-1775.

[48] R. A. Gingold and J. J. Monaghan, "Smoothed particle hydrodynamics: theory and application to non-spherical stars," *Monthly Notices of the Royal Astronomical Society*, vol. 181, no. 3, pp. 375–389, Dec. 1977, ISSN: 0035-8711. DOI: 10.1093/mnras/181.3.375.

[49] ——, "Kernel estimates as a basis for general particle methods in hydrodynamics," *Journal of Computational Physics*, vol. 46, no. 3, pp. 429–453, 1982, ISSN: 10902716. DOI: 10.1016/0021-9991(82)90025-0.

[50] J. J. Monaghan and R. A. Gingold, "Shock simulation by the particle method SPH," *Journal of Computational Physics*, vol. 52, no. 2, pp. 374–389, 1983, ISSN: 10902716. DOI: 10.1016/0021-9991(83)90036-0.

[51] J. J. Monaghan, "Why Particle Methods Work," *SIAM Journal on Scientific and Statistical Computing*, vol. 3, no. 4, pp. 422–433, Dec. 1982, ISSN: 0196-5204. DOI: 10.1137/0903027.

[52] ——, "An introduction to SPH," *Computer Physics Communications*, vol. 48, no. 1, pp. 89–96, 1988, ISSN: 00104655. DOI: 10.1016/0010-4655(88)90026-4.

[53] ——, "Smoothed particle hydrodynamics," *Annual Review of Astronomy and Astrophysics*, vol. 30, no. 1, pp. 543–574, 1992, ISSN: 00664146. DOI: 10.1146/annurev.aa.30.090192.002551.

[54] W. Benz, *The Numerical Modelling of Nonlinear Stellar Pulsations*, J. R. Buchler, Ed. Dordrecht: Springer Netherlands, 1990, pp. 269–289, ISBN: 978-94-010-6720-1. DOI: 10.1007/978-94-009-0519-1.

[55] P. Liu, Y. Liu, and X. Zhang, "Simulation of hyper-velocity impact on double honeycomb sandwich panel and its staggered improvement with internal-structure model," *International Journal of Mechanics and Materials in Design*, vol. 12, no. 2, pp. 241–254, 2016, ISSN: 15738841. DOI: 10.1007/s10999-015-9300-7.

[56] Z. Ye, X. Zhang, G. Zheng, and G. Jia, "A material point method model and ballistic limit equation for hyper velocity impact of multi-layer fabric coated aluminum plate," *International Journal of Mechanics and Materials in Design*, vol. 14, no. 4, pp. 511–526, 2018, ISSN: 15738841. DOI: 10.1007/s10999-017-9387-0.

[57] Y. P. Lian, X. Zhang, and Y. Liu, "An adaptive finite element material point method and its application in extreme deformation problems," *Computer Methods in Applied Mechanics and Engineering*, vol. 241-244, pp. 275–285, 2012, ISSN: 00457825. DOI: 10.1016/j.cma.2012.06.015.

[58] P. W. Randles and L. D. Libersky, "Normalized SPH with stress points," *International Journal for Numerical Methods in Engineering*, vol. 48, no. 10, pp. 1445–1462, Aug. 2000, ISSN: 0029-5981. DOI: 10.1002/1097-0207(20000810)48:10<1445::AID-NME831>3.0.CO;2-9.

[59] C. T. Dyka, P. W. Randles, and R. P. Ingel, "Stress Points for Tension Instability in SPH," *International Journal for Numerical Methods in Engineering*, vol. 40, no. 13, pp. 2325–2341, Jul. 1997, ISSN: 0029-5981. DOI: 10.1002/(SICI)1097-0207(19970715)40:13<2325::AID-NME161>3.0.CO;2-8.

[60] G. Oger, M. Doring, B. Alessandrini, and P. Ferrant, "An improved SPH method: Towards higher order convergence," *Journal of Computational Physics*, vol. 225, no. 2, pp. 1472–1492, Aug. 2007, ISSN: 10902716. DOI: 10.1016/j.jcp.2007.01.039.

[61] A. Shaw and S. R. Reid, "Heuristic acceleration correction algorithm for use in SPH computations in impact mechanics," *Computer Methods in Applied Mechanics and Engineering*, vol. 198, no. 49-52, pp. 3962–3974, Nov. 2009, ISSN: 00457825. DOI: 10.1016/j.cma.2009.09.006.

[62] E. P. Fahrenthold and B. A. Horban, "A hybrid particle-finite element method for hypervelocity impact simulation," *International Journal of Impact Engineering*, vol. 23, no. 1 PART I, pp. 237–248, 1999, ISSN: 0734743X. DOI: 10.1016/s0734-743x(99)00076-7.

[63] ——, "An improved hybrid particle-element method for hypervelocity impact simulation," *International Journal of Impact Engineering*, vol. 26, no. 1-10, pp. 169–178, 2001, ISSN: 0734743X. DOI: 10.1016/s0734-743x(01)00079-3.

[64] C. Alves and C. Armando Duarte, *Advances in Meshfree Techniques*, V. M. A. Leitão, C. J. S. Alves, and C. Armando Duarte, Eds., 9. Dordrecht: Springer Netherlands, 2007, vol. 53, ISBN: 978-1-4020-6094-6. DOI: 10.1007/978-1-4020-6095-3.

[65] G. R. Johnson, S. R. Beissel, and C. A. Gerlach, "A combined particle-element method for high-velocity impact computations," in *Procedia Engineering*, vol. 58, Elsevier Ltd, Jan. 2013, pp. 269–278. DOI: 10.1016/j.proeng.2013.05.031.

[66] G. R. Johnson, "Linking of Lagrangian particle methods to standard finite element methods for high velocity impact computations," *Nuclear Engineering and Design*, vol. 150, no. 2-3, pp. 265–274, Sep. 1994, ISSN: 00295493. DOI: 10.1016/0029-5493(94)90143-0.

[67] G. R. Johnson, S. R. Beissel, and C. A. Gerlach, "Another approach to a hybrid particle-finite element algorithm for high-velocity impact," *International Journal of Impact Engineering*, vol. 38, no. 5, pp. 397–405, May 2011, ISSN: 0734743X. DOI: 10.1016/j.ijimpeng.2011.01.002.

[68] G. R. Johnson and R. A. Stryk, "Conversion of 3D distorted elements into meshless particles during dynamic deformation," *International Journal of Impact Engineering*, vol. 28, no. 9, pp. 947–966, Oct. 2003, ISSN: 0734743X. DOI: 10.1016/S0734-743X(03)00012-5.

[69] G. R. Johnson, S. R. Beissel, and R. A. Stryk, "Generalized particle algorithm for high velocity impact computations," *Computational Mechanics*, vol. 25, no. 2, pp. 245–256, 2000, ISSN: 01787675. DOI: 10.1007/s004660050473.

[70] Q. G. He, X. Chen, and J. F. Chen, "Finite element-smoothed particle hydrodynamics adaptive method in simulating debris cloud," *Acta Astronautica*, vol. 175, pp. 99–117, Oct. 2020, ISSN: 00945765. DOI: 10.1016/j.actaastro.2020.05.056.

[71] M. Faraud, "Numerical simulation of orbital debris impact on spacecraft G," Tech. Rep., Jan. 1996. DOI: 10.2495/SUSI960251.

[72] ANSYS, "ANSYS Autodyn User's Manual," no. January 2018, 2018.

[73] M. Wicklein, S. Ryan, D. M. White, and R. A. Clegg, "Hypervelocity impact on CFRP: Testing, material modelling, and numerical simulation," *International Journal of Impact Engineering*, vol. 35, no. 12, pp. 1861–1869, 2008, ISSN: 0734743X. DOI: 10.1016/j.ijimpeng.2008.07.015.

[74] W. Riedel, H. Nahme, D. M. White, and R. A. Clegg, "Hypervelocity impact damage prediction in composites: Part II-experimental investigations and simulations," *International Journal of Impact Engineering*, vol. 33, no. 1-12, pp. 670–680, 2006, ISSN: 0734743X. DOI: 10.1016/j.ijimpeng.2006.09.052.

[75] T. Lässig, L. Nguyen, M. May, *et al.*, "A non-linear orthotropic hydrocode model for ultra-high molecular weight polyethylene in impact simulations," *International Journal of Impact Engineering*, vol. 75, pp. 110–122, 2015, ISSN: 0734743X. DOI: 10.1016/j.ijimpeng.2014.07.004.

[76] L. H. Nguyen, T. R. Lässig, S. Ryan, W. Riedel, A. P. Mouritz, and A. C. Orifici, "A methodology for hydrocode analysis of ultra-high molecular weight polyethylene com-

posite under ballistic impact," *Composites Part A: Applied Science and Manufacturing*, vol. 84, pp. 224–235, 2016, ISSN: 1359835X. DOI: 10.1016/j.compositesa.2016.01.014.

[77] "Hypervelocity impact sample." (), [Online]. Available: https://www.esa.int/ESA_Multimedia/Images/2009/02/Hypervelocity_impact_sample (visited on 11/09/2021).

[78] Y. Michel, J. M. Chevalier, C. Durin, C. Espinosa, F. Malaise, and J. J. Barrau, "Hypervelocity impacts on thin brittle targets: Experimental data and SPH simulations," *International Journal of Impact Engineering*, vol. 33, no. 1-12, pp. 441–451, 2006, ISSN: 0734743X. DOI: 10.1016/j.ijimpeng.2006.09.081.

[79] Y. Michel, N. Le Roux, C. Durin, *et al.*, "Damages and matter ejection during HVI on brittle structures: Implications for space environment," *European Space Agency, (Special Publication) ESA SP*, no. 616, pp. 1–16, 2006, ISSN: 03796566.

[80] A. Moussi, G. Drolshagen, J. A. McDonnell, J. C. Mandeville, A. T. Kearsley, and H. Ludwig, "Hypervelocity impacts on HST solar arrays and the debris and meteoroids population," *Advances in Space Research*, vol. 35, no. 7, pp. 1243–1253, 2005, ISSN: 02731177. DOI: 10.1016/j.asr.2005.03.060.

[81] Y. Michel, "Phenomene dimpact a Haute Vitesse Sur Cibles Minces Fragiles - Application au Projet de Laser Megajoule et a la Problematique des Debris Spatiaux," Ph.D. dissertation, Université Toulouse III Paul Sabatier, 2007.

[82] M. Liu, Q. Wang, Q. Zhang, R. Long, and Z. Su, "Characterizing hypervelocity (>2.5km/s)-impact-engendered damage in shielding structures using in-situ acoustic emission: Simulation and experiment," *International Journal of Impact Engineering*, vol. 111, no. October, pp. 273–284, 2018, ISSN: 0734743X. DOI: 10.1016/j.ijimpeng.2017.10.004.

[83] D. J. Steinberg, S. G. Cochran, and M. W. Guinan, "A constitutive model for metals applicable at high-strain rate," *Journal of Applied Physics*, vol. 51, p. 1498, 1980. DOI: 10.1063/1.327799.

[84] B. Verheijen, D. I. Gransden, O. K. Bergsma, U. Heisserer, and H. V. D. Werff, "Feasibility study of the modelling of hypervelocity impacts in ultra high molecular weight polyethylene composites using an SPH discretisation method," no. 3, pp. 18–20, 2017.

[85] E. A. Taylor, C. J. Hayhurst, and K. Tsembelis, "Hydrocode modelling of space debris hypervelocity impact on soda-lime glass using the Johnson-Holmquist brittle material model," *European Space Agency, (Special Publication) ESA SP*, no. 393, pp. 449–453, 1997, ISSN: 03796566.

[86] V. Leus, Y. Neumann, E. Racah, *et al.*, "Experimental and Numerical Study of Aluminum 6061-T6 Fragmentation Process at Very High Strain Rates," Tech. Rep., 2011.

[87] ANSYS, *AUTODYN User Subroutines Tutorial*, November. 2013.

[88] B. Denardo and C. Nysmith, "Momentum Transfer And Cratering Phenomena Associated with the Impact of Alumnium Spheres into Thick Aluminium Targets at Velocities to 24,000 Feet per Second," pp. 389–402, 1964.

[89] L. E. Murr, S. A. Quinones, E. Ferreyra T, *et al.*, "The low-velocity-to-hypervelocity penetration transition for impact craters in metal targets," *Materials Science and Engineering A*, vol. 256, no. 1-2, pp. 166–182, Nov. 1998, ISSN: 09215093. DOI: 10.1016/s0921-5093(98)00796-5.

[90] E. A. Taylor, "Experimental Hypervelocity and Computational Impact on Brittle Study of and Materials Composites," no. April, 1998.

[91] E. A. Taylor and J. A. McDonnell, "Hypervelocity impact on soda lime glass: Damage equations for impactors in the 400-2000 M range," *Advances in Space Research*, vol. 20, no. 8, pp. 1457–1460, 1997, ISSN: 02731177. DOI: 10.1016/S0273-1177(97)00416-X.

[92] E. A. Taylor, K. Tsembelis, C. J. Hayhurst, L. Kay, and M. J. Burchell, "Hydrocode modelling of hypervelocity impact on brittle materials: Depth of penetration and conchoidal diameter," *International Journal of Impact Engineering*, vol. 23, no. 1 Part II, pp. 895–904, 1999, ISSN: 0734743X. DOI: 10.1016/s0734-743x(99)00133-5.

[93] T. J. Holmquist and G. R. Johnson, "A computational constitutive model for glass subjected to large strains, high strain rates and high pressures," *Journal of Applied Mechanics, Transactions ASME*, vol. 78, no. 5, pp. 1–9, 2011, ISSN: 00218936. DOI: 10.1115/1.4004326.

[94] Z. Wei, H. Yue, G. Gongshun, and P. Baojun, "Experimental and numerical studies of laminated glass subject to hypervelocity impact," *European Space Agency, (Special Publication) ESA SP*, vol. 2005, no. 587, pp. 431–436, 2005, ISSN: 03796566.

[95] D. M. White, E. A. Taylor, and R. A. Clegg, *Numerical simulation and experimental characterisation of direct hypervelocity impact on a spacecraft hybrid carbon fibre/Kevlar composite structure*, 2003. DOI: 10.1016/j.ijimpeng.2003.10.024.

[96] S. Ryan, F. Schaefer, R. Destefanis, and M. Lambert, "A ballistic limit equation for hypervelocity impacts on composite honeycomb sandwich panel satellite structures," *Advances in Space Research*, vol. 41, no. 7, pp. 1152–1166, 2008, ISSN: 02731177. DOI: 10.1016/j.asr.2007.02.032.

[97] F. Schäfer, E. Schneider, and M. Lambert, "Review of ballistic limit equations for CFRP structure walls of satellites," *European Space Agency, (Special Publication) ESA SP*, no. 558, pp. 431–443, 2004, ISSN: 03796566.

[98] S. Ryan, "Hypervelocity Impact Induced Disturbances on Composite Sandwich," Ph.D. dissertation, RMIT University, 2007, p. 228, ISBN: 9783816775225.

[99] "Hst, hubble space telescope." (), [Online]. Available: https://esahubble.org/images/hubble_earth_sp01/ (visited on 11/10/2021).

[100] W. P. Schonberg, "Using Modified Ballistic Limit Equations in Spacecraft Risk Assessments," *Acta Astronautica*, vol. 126, p. 199, Sep. 2016, ISSN: 00945765. DOI: 10.1016/j.actaastro.2016.03.038.

[101] A. R. Coronado, M. N. Gibbins, M. A. Wright, and P. H. Stern, "Space station integrated wall design and penetration damage control," *undefined*, 1987.

[102] D. L. Oltrogge, S. Alfano, C. Law, A. Cacioni, and T. S. Kelso, "A comprehensive assessment of collision likelihood in Geosynchronous Earth Orbit," *Acta Astronautica*, vol. 147, pp. 316–345, Jun. 2018, ISSN: 0094-5765. DOI: 10.1016/J.ACTAASTRO.2018.03.017.

[103] J. M. Siguier and J. C. Mandeville, "Test procedures to evaluate spacecraft materials ejecta upon hypervelocity impact," *Proceedings of the Institution of Mechanical Engineers, Part G: Journal of Aerospace Engineering*, vol. 221, no. 6, pp. 969–974, 2007, ISSN: 09544100. DOI: 10.1243/09544100JAERO236.

[104] E. A. Taylor, H. J. Scott, M. Abraham, and A. T. Kearsley, "Hypervelocity Impact on Silicon Wafers with Metallic and Polymeric Coatings,"

[105] M. C. Price, A. T. Kearsley, and M. J. Burchell, "Validation of the Preston-Tonks-Wallace strength model at strain rates approaching 1011 s-1 for Al-1100, tantalum and copper using hypervelocity impact crater morphologies," *International Journal of Impact Engineering*, vol. 52, pp. 1–10, 2013, ISSN: 0734743X. DOI: 10.1016/j.ijimpeng.2012.09.001.

[106] S. Ren, X. Yang, R. Wang, S. Liu, and X. Sun, "The interaction between the LEO satellite constellation and the space debris environment," *Applied Sciences (Switzerland)*, vol. 11, no. 20, 2021, ISSN: 20763417. DOI: 10.3390/app11209490.

A

Material Models

A.1. Al 2024-T4 Parameters

Parameter	Value	Unit
Equation of State: Shock		
Reference Density	2.785	g/cm^3
Gruneisen Coefficient	2.0	-
Parameter C1	5.328E+3	-
Parameter S1	1.338	-
Reference Temperature	300	K
Specific Heat	863	J/kgK
Strength: Steinberg Guinan		
Shear Modulus	2.86E+7	kPa
Yield Stress	2.6E+5	kPa
Maximum Yield Stress	7.6E+5	kPa
Hardening Constant	310	-
Hardening Exponent	0.185	-
Derivative dG/dP	1.8647	-
Derivative dG/dT	-1.762E+4	kPa/K
Melting Temperature	1.22E+3	K
Failure: Hydro (Pmin)		
Hydro Tensile Limit	-4.27E+5	kPa
Reheal	No	-
Crack Softening	No	-
Stochastic Failure	No	-

Table A.1: Al 2024-T4 material model parameters.

A.2. Soda-Lime Glass Parameters

Parameter	Value	Unit
Equation of State: Polynomial		
Reference Density	2.53	g/cm^3
Bulk Modulus A1	4.54E+7	kPa
Parameter A2	-1.38E+8	kPa
Parameter A3	2.9 E+8	kPa
Parameter B0	0	-
Parameter B1	0	-
Reference Temperature	0	K
Specific Heat	0	J/kgK
Thermal Conductivity	0	J/mKs
Strength: Johnson-Holmquist		
Shear Modulus	3.04E+7	kPa
Model Type	Continuous	-
Hugoniot Elastic Limit	5.95E+6	kPa
Intact Strength Constant A	0.93	-
Intact Strength Exponent N	0.77	-
Strain Rate Constant C	0.003	-
Fractured Strength Constant	0.035	-
Fractured Strength Exponent	0.4	-
Max. Fractured Strength Ratio	0.5	-
Failure: Johnson-Holmquist		
Hydro Tensile Limit	-3.50E+4	kPa
Model Type	Continuous	-
Damage Constant D1	0.053	-
Damage Constant D2	0.85	-
Damage Type	Gradual (JH2)	-
Tensile Failure	Hydro (Pmin)	-

Table A.2: Soda-Lime Glass material model parameters.

A.3. Silicon Parameters

Parameter	Value	Unit
Equation of State: Polynomial		
Reference Density	2.34	g/cm^3
Bulk Modulus A1	1.02E+8	kPa
Parameter A2	1.55E+8	kPa
Parameter A3	7.37E+7	kPa
Parameter B0	0	-
Parameter B1	0	-
Parameter T1	1.02E+8	kPa
Parameter T2	0	kPa
Reference Temperature	293.00	K
Specific Heat	0	J/kgK
Thermal Conductivity	0	J/mKs
Strength: Johnson-Holmquist		
Shear Modulus	7.17E+7	kPa
Model Type	Continuous	-
Hugoniot Elastic Limit	1.00E+07	kPa
Intact Strength Constant A	0.93	-
Intact Strength Exponent N	0.77	-
Strain Rate Constant C	0.003	-
Fractured Strength Constant	0.035	-
Fractured Strength Exponent	0.4	-
Max. Fractured Strength Ratio	0.5	-
Failure: Johnson-Holmquist		
Hydro Tensile Limit	-1.50E+5	kPa
Model Type	Continuous	-
Damage Constant D1	0.05	-
Damage Constant D2	0.85	-
Bulking Constant, Beta	1.00	-
Damage Type	Gradual (JH2)	-
Tensile Failure	Hydro (Pmin)	-

Table A.3: Silicon material model parameters.

A.4. Copper Parameters

Parameter	Value	Unit
Equation of State: Shock		
Reference Density	8.93	g/cm^3
Gruneisen Coefficient	2.02	-
Parameter C1	3.94E+3	-
Parameter S1	1.489	-
Reference Temperature	300	K
Specific Heat	383	J/kgK
Strength: Steinberg Guinan		
Shear Modulus	4.77E+7	kPa
Yield Stress	1.2E+5	kPa
Maximum Yield Stress	6.4E+5	kPa
Hardening Constant	36	-
Hardening Exponent	0.45	-
Derivative dG/dP	1.35	-
Derivative dG/dT	-1.798E+4	kPa/K
Melting Temperature	1.79E+3	K
Failure: Hydro (Pmin)		
Hydro Tensile Limit	-2.00E+5	kPa
Reheal	No	-
Crack Softening	No	-
Stochastic Failure	No	-

Table A.4: Copper material model parameters.

B

User Subroutine

```
1
2       SUBROUTINE EXEDIT
3
4       USE kindef
5       USE wrapup
6       USE mdgrid
7       USE ranges
8       USE kindef
9       USE cycvar    !STORES THE CYCLE VARIABLES (E.G. TIME)
10      USE subdef
11      USE fildef
12    USE matdef    !STORES ALL RELEVANT MATERIAL ASSIGNMENTS AND DETAILS
13    USE material
14
15
16      IMPLICIT NONE
17
18    ! Define user variables
19    INTEGER (INT4)  ::  NS,I,J,IJK,counter
20    REAL (REAL8)  ::  X_LIMIT,X_LIMIT_POS,POS_X,POS_Y,SIM_TIME,VEL_X,VEL_Y
21
22
23      !
    **************************************************************************
24
25      ! THIS IS A USER SUPPLIED SUBROUTINE WHICH CAN BE USED TO PROVIDE
26      ! SPECIAL CUSTOM EDITING. THE FREQUENCY AT WHICH THIS SUBROUTINE
27      ! IS CALLED IS DEFINED THROUGH INPUT (GLOBAL-EDIT-USER). WHEN
28      ! REQUESTED, IT IS CALLED BY THE EDIT PROCESSOR AT THE END OF A
29      ! COMPUTATIONAL CYCLE. THE ROUTINE IS CALLED BEFORE ANY OTHER
30      ! TYPES OF STANDARD EDITS ARE CALLED FOR THAT CYCLE (EG. PRINT,
31      ! SAVE, HISTORY, DISPLAY, ETC), SO IT MAY ALSO BE USED TO SET UP
32      ! DATA TO BE PROCESSED BY OTHER EDIT TYPES.
```

```
33
34        !
      **********************************************************************
35
36        ! Specify the output files
37      ! Desired output is a text file which lists the relevant variables for each
       fragment, i.e.
38      ! Fragment  Mat-ID  Part  Index X_POS Y_POS Z_POS Time  X_VEL Y_VEL Z_VEL
      Mass
39
40      open(99,FILE=trim(FNID)//'.dat')
41      write (99, '(A15)',advance='no')'Cycle no: '
42      write (99, '(I10)',advance='yes')NCYCLE
43      write (99, '(A15)',advance='yes')' '
44      write (99, '(A15)',advance='no')'Fragment'
45      write (99, '(A15)',advance='no')'Index'
46      write (99, '(A15)',advance='no')'X-POS'
47      write (99, '(A15)',advance='no')'Y_POS'
48      write (99, '(A15)',advance='no')'Time'
49      write (99, '(A15)',advance='no')'X_VEL'
50      write (99, '(A15)',advance='no')'Y_VEL'
51      write (99, '(A15)',advance='no')'Mass'
52      write (99, '(A15)',advance='yes')' '
53
54
55      !The variable count is initialized to 0
56          counter = 0
57      ! Defining the x-boundaries
58      X_LIMIT = 0
59          X_LIMIT_POS = 0.75
60
61      ! Initialization of arrays
62      ! This set of loops generates a variable array IJK which defines each IJK
      index in each part
63      DO NS=1,NUMSUB
64      NSUB=NS
65      CALL GETSUB
66        DO I=1,IMAX
67          DO J=1,JMAX
68              IJK=IJSET(I,J)
69          END DO
70        END DO
71      END DO
72
73      ! Determining the fragment variables
74        DO NS = 1, NUMSUB ! From NS = 1 to the Number of Parts in problem
75      NSUB = NS
76      CALL GETSUB
77      CALL GETMAT
78        DO I = 1,IMAX
79          DO J = 1,JMAX
```

```
80            IJK=IJSET(I,J)
81            SIM_TIME=0    ! Resets the counter
82            IF ((XN(IJK).LE.X_LIMIT).OR.(XN(IJK).GE.X_LIMIT_POS).AND.(SIM_TIME
    ==0)) THEN !If (X space coordinate is less than X_limit or greater than
    X_limit_pos)
83                                !and (simulation time is equal to 0).
84                counter=counter+1 !The variable count is incremented each time
    the loop body is executed. When the loop exits, count contains the result
85                                !the total number of times the loop body was
    executed, which is the same as the number of digits.
86                SIM_TIME=TIME !TIME is an already defined variable - CURRENT
    TIME
87                write(99,'(I15)',advance='no')counter
88                !write(99,'(A15)',advance='no')ADJUSTR(NODE_MAT)
89                !write(99,'(A15)',advance='no')ADJUSTR(NAMSUB(NSUB))
90                write(99,'(I15)',advance='no')IJK
91                write(99,'(F15.5)',advance='no')XN(IJK)
92                write(99,'(F15.5)',advance='no')YN(IJK)
93                write(99,'(F15.5)',advance='no')TIME
94                write(99,'(F15.5)',advance='no')UXN(IJK)
95                write(99,'(F15.5)',advance='no')UYN(IJK)
96                write(99,'(F15.5)',advance='yes')CMASS(IJK)
97            END IF
98          END DO
99        END DO
100     END DO
101   CLOSE(99)
102   RETURN
103     END SUBROUTINE EXEDIT
```